



저작자표시-비영리-변경금지 2.0 대한민국

이용자는 아래의 조건을 따르는 경우에 한하여 자유롭게

- 이 저작물을 복제, 배포, 전송, 전시, 공연 및 방송할 수 있습니다.

다음과 같은 조건을 따라야 합니다:



저작자표시. 귀하는 원저작자를 표시하여야 합니다.



비영리. 귀하는 이 저작물을 영리 목적으로 이용할 수 없습니다.



변경금지. 귀하는 이 저작물을 개작, 변형 또는 가공할 수 없습니다.

- 귀하는, 이 저작물의 재이용이나 배포의 경우, 이 저작물에 적용된 이용허락조건을 명확하게 나타내어야 합니다.
- 저작권자로부터 별도의 허가를 받으면 이러한 조건들은 적용되지 않습니다.

저작권법에 따른 이용자의 권리는 위의 내용에 의하여 영향을 받지 않습니다.

이것은 [이용허락규약\(Legal Code\)](#)을 이해하기 쉽게 요약한 것입니다.

[Disclaimer](#)

A THESIS  
FOR THE DEGREE OF DOCTOR OF PHILOSOPHY

**Evaluation of Flexible Resistive Random Access Memory  
Devices Fabricated with Nanocomposites of 2D Materials**

By  
**Muhammad Muqet Rehman**

Department of Mechatronics Engineering  
GRADUATE SCHOOL  
JEJU NATIONAL UNIVERSITY  
2018. 02

# Evaluation of Flexible Resistive Random Access Memory Devices Fabricated with Nanocomposites of 2D Materials

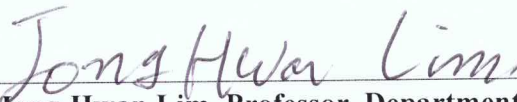

Muhammad Muqet Rehman

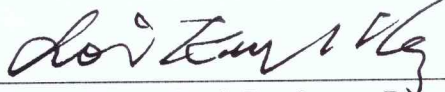

(Supervised by Professor Kyung Hyun Choi)


A thesis submitted in partial fulfillment of the requirement for the degree of Doctor of Philosophy

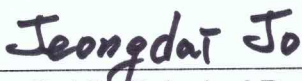

2018. 02


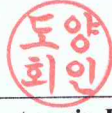
The thesis has been examined and approved.

  
Thesis Director, Jong-Hwan Lim, Professor, Department of Mechatronics Engineering 

  
Thesis Supervisor Kyung Hyun Choi, Professor, Department of Mechatronics Engineering 

  
Chang-Nam Kang, Professor, Department of Mechanical Engineering

  
Jeong-Dai Jo, Principal Researcher, Korea Institute of Machinery & Materials 

  
Yang-Hoi Doh, Professor, Department of Electronic Engineering 

-----  
Date

Department of Mechatronics Engineering

GRADUATE SCHOOL

JEJU NATIONAL UNIVERSITY

REPUBLIC OF KOREA



*This Thesis is Dedicated to my Parents,  
Fiancé, Siblings, Teachers, Friends, and  
Entire Nation of Pakistan*

## ACKNOWLEDGEMENTS

I would like to extend my modest gratitude to Allah Almighty, the most Gracious and Merciful. He provided me the strength and hope during extremely tough phase of my doctoral studies. I seek his guidance and refuge from upcoming difficulties of life as well. I am highly thankful to the last Prophet Hazrat Muhammad (PBUH) for all the difficulties that he faced in delivering the message of Allah Almighty with honesty and diligence only for the sake of humanity.

This dissertation would not have been possible without the continuous support, guidance and encouragement of Prof Kyung Hyun Choi (PhD supervisor) who always kept challenging and pushing me throughout my doctoral studies to do better. It is due to his continuous motivation that I have managed to achieve so much during my PhD studies. Under the guidance and management of Prof. Choi, I was not only able to become an expert of my own research field but also developed the basic knowledge of several modern day sciences and technologies owing to the brainstorming sessions, stimulating seminars, international workshops, and endless appetite for perfection. His working stamina will certainly be a source of inspiration for the rest of my life.

I am extremely grateful to Dr. Khalid Rehman (Alumni of AMM Lab) who introduced me to my supervisor for postgraduate studies. I have been fortunate enough to work among the highly competent and multidisciplinary group of enthusiastic researchers in these three years of my PhD studies. My PhD would not have been possible without the everlasting support, guidance and counselling of Dr. Ghayas Uddin Siddiqui and Dr. Kamran Ali. Jahan Zeb Gul was more than a colleague as he always helped me with his technical expertise when I needed them the most. The support and emotional attachment of my younger brother and colleague, Hafiz Mohammad Mutee ur Rehman is worth mentioning, especially during the five months of my fractured foot when he took care of all domestic matters and bare all the burden on his shoulders alone so that I can focus on my work. I would also like to thank my Korean colleagues specially Sowon Kim, Gobum and Khyung Huwan who helped me a lot during my research work and managerial issues regarding office work. I would like to thank Dr. Junaid Ali, Dr. Shahid Aziz, Dr. Srikanth Karthik, Imran Shah, Mohsin Abbas, Shital Kumar, and Asad Ullah for making my journey memorable at AMM lab.

I would specially like to thank three of my finest friends with whom I shared a special bond of friendship during PhD including Dr. Afaq Muhammad, Zubair Amjad and Fasih Ullah for giving me countless cherishable moments to remember. I am also thankful to the wonderful friends with whom I enjoyed every bit of my stay at Jeju by playing competitive cricket matches including Dr. Rashid Ahmed, Dr. Farrukh Israr, Dr. Safdar Ali, Dr Anil Kumar, Dr. Waqar Abbasi, Dr. Arshad Hassan, Dr. Irshad Ali, Tahir Abbas, Asif Mahmood, Talha Jadoon, Mudassar Liaq, Waseem Abbas, Gul Hassan, Adeel Farooq, and Waqar Kayani.

I am indebted to my great teachers due to whom I have managed to come this far by taking small steps. I owe every bit of my developed knowledge to my school teachers. My school (Sadiq Public School, Bahawalpur) teachers including Sir Muhammad Usman Malik (Physics), Sir Faiz Kareem Malik (Chemistry), Sir Nazeer Ahmad (Additional Mathematics), and Sir Muhammad Mansoor Abdullah (Mathematics) provided me with a strong knowledge base and due to their joint efforts

I had my first major success in the shape of my O-Levels result. My college (Moon System of Education, Bahawalpur) teachers including Dr. Mehmood Aslam (Chemistry) and Mr. Raja Amjad (Physics) inspired me with the most important jewel of hard work to achieve my goals. My university (Ghulam Ishaq Khan Institute-GIKI) teachers including Prof. Junaid Mughal, Prof. Nisar Ahmed and Prof. Khasan S. Karimov refined my abilities to broaden my analytical views and enhanced my problem solving aptitude.

I would also like to praise and acknowledge the scenic beauty of Jeju National University (JNU). The clean air and hygienic lifestyle helped me a lot to do my hard work without getting sick. The dormitory life and Cricket ground at JNU made my life extremely comfortable and colourful. I enjoyed every bit of my weekends here by taking an active part in the cricket of JNU and travelling to most amazing places of this beautiful island.

I am forever thankful to my father (Mr. Muhammad Mujeeb ur Rehman) and my mother (Mrs. Farkhanda Mahmood) who sacrificed their youth and happiness for my prosperous future. They worked day and night to provide me with a dream life by protecting me from the hardships of life. I would like to thank my fiancé, Ms. Maryam Khan who was a great support in these three tough years of my life. Her optimistic and encouraging nature always helped me to fight through the difficult times. I am thankful to my elder sister (Mrs. Sana Rehman), elder brother (Mr. Muhammad Junaid ur Rehman), brother in law (Mr. Nadir Hayat), nephew (Muhammad Faiz Hayat) and niece (Haniya Hayat) for their priceless prayers, love and support.

Lastly I would like to thank the Korean Nation to whom I found very accommodating, open minded and welcoming. It was a great experience to live in such a clean, safe, developed and modern country.

## List of Figures

|   |    |
|---|----|
| Figure 1. 3D and 2D view of Reverse Off-Set schematic diagram illustrating the patterning of bottom Ag electrodes on flexible PET substrate a) Glass slide b) Ag nanoparticles ink spin coated on glass slide c) Ag ink being attached with the PDMS blanket by rolling the blanket roll over Ag coated glass slide d) Cliché showing the engraved patterns on its surface e) OFF Process taking place in which engraved patterns of cliché are being transferred onto PDMS blanket f) SET Process in which Ag electrodes are transferred from blanket roll onto the desired PET substrate .....  | 7  |
| Figure 2. Schematic diagram of reciprocating (RPC) inkjet printing system and illustration of each fabrication step with optical images of three different size circular top electrodes .....   | 10 |
| Figure 3. a) Schematic diagram of EHDA process with labelling of each part b) Operating envelope of EHDA process for the deposition of functional thin film. ....   | 11 |
| Figure 4. Chemical structure and as synthesized ink of a few layered WS <sub>2</sub> material .....   | 12 |
| Figure 5. Chemical structures of dielectric PVA polymer and semi-conductive pristine MoS <sub>2</sub> displaying their interatomic bonding along with the as synthesized exfoliated few layered MoS <sub>2</sub> flakes ink with PVA dissolved in NMP solvent .....   | 14 |
| Figure 6. Chemical structures of as synthesized 2D materials including hBN flakes, QDs and their nanocomposite. The prepared inks of each material in their respective solvents is shown at the bottom of each chemical structure.....  | 15 |
| Figure 7. Complete process of synthesizing an all 2D QDs-hBN nanocomposite ink with proper color scheme. The synthesis of hBN flakes are illustrated in the upper part while QDs synthesis is shown in the lower part of diagram. ....  | 16 |
| Figure 8. Schematic representation of the advanced 2D nanocomposite synthesis. The upper row illustrates the preparation of MoS <sub>2</sub> QDs while the bottom layer is showing the preparation of hBN flakes by using chemical liquid exfoliation in DMF, NMP, and DMEU respectively with appropriate color scheme and labelling of each step.....  | 18 |
| Figure 9. (a) FESEM image of as exfoliated WS <sub>2</sub> solution via liquid exfoliation with co-solvent (b) morphology of as deposited thin films of exfoliated WS <sub>2</sub> flakes through EHDA showing large lateral size up to few microns making it uniform and continuous. (c) HR-TEM image of exfoliated mono or few layer graphene nanosheets (d) Exfoliated hBN nanoflakes illustrating their platelike shape and size of the individual flake in the range of 100 nm-several nanometers (e) HR-TEM image displaying the uniform size and high concentration of QDs, inset histogram exhibits the average size of as synthesized QDs (2-4 nm) (f) HR-TEM image of as synthesized MoS <sub>2</sub> QDs (g) FESEM image illustrating the high density of as synthesized MoS <sub>2</sub> flakes (h) Typical bright field TEM image of MoS <sub>2</sub> flakes showing layer edges (i) Phase contrast High Resolution (HR) TEM image of thin MoS <sub>2</sub> flakes clearly displaying layer edges. Inset in (i) shows the selective area electron diffraction (SAED) pattern (j) AFM image illustrating a single flake of hBN surrounded by MoS <sub>2</sub> QDs. The thickness of a single hBN flake as displayed in this image is 4 nm verifying that it is a few layer flake (k) AFM image of formed 2D nanocomposite demonstrating the thickness of an individual hBN flake and interspersions of QDs onto and around it. (l) AFM image of single exfoliated MoS <sub>2</sub> flake illustrating its few layered nature with average thickness of 4 nm ..... | 20 |
| Figure 10. 2D nanomap image displaying the surface morphology of as deposited active thin film of MoS <sub>2</sub> -PVA nanocomposite by using EHD Atomization. The average roughness value is equal to 41.19 nm .....  | 22 |
| Figure 11. (a) Raman spectra of as deposited thin film of WS <sub>2</sub> flakes (b) XRD results of pristine and exfoliated WS <sub>2</sub> flakes (c) Raman spectra of pristine and exfoliated hBN flakes illustrating a clear shift in the peak (d) Raman spectra of exfoliated hBN nanoflakes (e) Typical Raman spectra of a few layered   |    |

|  |    |
|--|----|
| MoS <sub>2</sub> semiconductor (f) XPS data of as deposited Al <sub>2</sub> O <sub>3</sub> thin film for encapsulation of our memory device .....  | 25 |
| Figure 12. (a) Optical absorption and transmittance of as deposited thin film of WS <sub>2</sub> flakes (b) Illustration of optical transmittance and absorbance of 2D nanocomposite thin film. (c) Transmittance and absorbance spectra of as deposited thin film of GQDs/hBN nanocomposite (d) UV-vis optical transmittance spectra of the as synthesized few layered MoS <sub>2</sub> flakes .....  | 27 |
| Figure 13. Schematic diagram of entire device fabrication through all printed technology followed by encapsulation of atomically thin film of Al <sub>2</sub> O <sub>3</sub> to enhance its lifetime.....  | 29 |
| Figure 14. Optical microscope images of as patterned Ag electrodes on flexible PET substrate illustrating their high uniformity and smooth surface .....   | 32 |
| Figure 15. a) Schematic diagram of Electrohydrodynamic (EHD) Atomization system for spraying GQDs-hBN thin film over the patterned silver (Ag) electrodes with labeling of each part b) Operating envelope of GQDs-hBN spray through EHDA illustrating the voltage range for each mode of deposition .....   | 34 |
| Figure 16. Flow diagram of flexible NVM device fabrication illustrating each step sequentially such as bare PET substrate, patterning of Ag electrodes with high resolution through reverse offset printing system, spraying functional thin film of GQDs-hBN nanocomposite through EHDA and finally encapsulating the whole device by atomically thin layer of Al <sub>2</sub> O <sub>3</sub> deposited through spatial ALD system. Optical image of the final device is shown in the center of the diagram. ....   | 36 |
| Figure 17. Operating envelope for the deposition of all 2D functional layer of the fabricated device based on the hBN/MoS <sub>2</sub> QDs nanocomposite. This plot illustrates different ranges of applied voltage and their respective flow rates .....  | 37 |
| Figure 18. (a) 3D schematic diagram of as fabricated nonvolatile memory device on a flexible PET substrate with three different top electrode sizes (b) Chemical structures of the 2D materials used as the functional layer of fabricated device.....   | 39 |
| Figure 19. Schematic diagram illustrating the whole manufacturing process of as fabricated memory device on a flexible PET substrate. The images enclosed in the red dotted block exhibit each step of the fabrication process while the images outside the block correspond to the resulting device after each step. The bottom left corner exhibit layer by layer sandwiched structure of a single memory cell in bend state with PET/Ag/MoS <sub>2</sub> -PVA/Ag configuration .....  | 42 |
| Figure 20. Optical images of bottom and top Ag electrodes displaying their high quality patterned by using reverse offset and EHD patterning systems respectively a) gap between side by side patterned bottom electrodes b) Magnified image of a single bottom electrode c) Two consecutive bottom electrodes with a thin film of MoS <sub>2</sub> -PVA nanocomposite coated on them by EHDA d) Magnified image of a single bottom electrode with a thin film of MoS <sub>2</sub> -PVA nanocomposite coated on it by EHDA e) Image of top electrode bisecting the bottom Ag electrode f) Magnified image of top electrode displaying its remarkably uniform surface ..... | 43 |
| Figure 21. Electrical characterization results of WS <sub>2</sub> based memory device (a) Characteristic bipolar I-V curve (b) retention I-V curves for a 10 <sup>5</sup> s (c) high endurance I-V curves for 1500 voltage sweeps (d) inverse relation of switching ratio with increasing applied voltage (e) High repeatability of as fabricated memory device as illustrated by the overlapping I-V curves of each of the nine memory cells chosen randomly .....  | 44 |
| Figure 22. Characteristic I-V curves of developed memory device with a sandwiched layer of WS <sub>2</sub> layered material in harsh environments. (a) with humidity ranging from 40% RH- 60% RH (b) with temperature varying from 30 °C – 50 °C.....  | 46 |



|   |    |
|---|----|
| Figure 23. Conduction mechanism as explained by the double logarithmic graph of the I-V curve. (a) This graph suggest that TCSCCLC is followed in the HRS while (b) Ohmic current model satisfies the conduction of LRS .....   | 47 |
| Figure 24. Mechanical characterization results of as fabricated memory device on a flexible substrate (a) Mechanical robustness against 1500 bending cycles (b) Mechanical robustness against various bending diameters from 50 mm to 5 mm. (c) Optical image of as fabricated WS <sub>2</sub> based memory device in bend state. ....  | 49 |
| Figure 25. Electrical characterization results of as fabricated NVM device (a) Electroforming curve before applying double voltage sweep (b) Characteristic bipolar I-V curve showing memory effect (c) Illustration of switching ratio with increasing voltage. The switching ratio is maximum at a read voltage in the range of 0.6 V - 0.9 V (d) I-V curves of whole memory cell array illustrating highly repeatable memory behavior in each cell .....   | 51 |
| Figure 26. (a) Electrical endurance curves for 1000 voltage sweeps with high stability (b) Illustration of high retentivity owing to the protection by the encapsulation coating of Al <sub>2</sub> O <sub>3</sub> through ALD (c) Cumulative probability plot of threshold voltages (both SET and RESET) showing high stability in the obtained results (d) Cumulative probability plot of bistable resistive states (both HRS and LRS) showing high stability in the obtained results with negligible deviation.....  | 52 |
| Figure 27. Illustration of working mechanism a) This part shows four different stages of filament formation and rupture such as initial condition (when Ag <sup>+</sup> cations are depleted in the functional layer), filament formation (where reduction of Ag <sup>+</sup> cations takes place), set process (A point where the formed filament connects anode with cathode to complete the pathway of charge carriers to flow) and finally the reset process (when voltage of opposite polarity is applied) b) Dependence of bistable resistive states (HRS and LRS) on temperature verifying the formation of metallic filament through the functional layer ..... | 54 |
| Figure 28. Mechanical characterization results of as fabricated flexible memory device a) Illustration of mechanical endurance for several bending cycles at a fixed diametre of 15 mm b) Display of mechanical robustness and stability over a range of bending diametres from 200 mm to 2 mm. c) Schematic diagram of as fabricated flexible memory device in bend state with labeling of each part d) Optical image of the developed memory device in bend state .....   | 56 |
| Figure 29. Optical images of as fabricated memory device obtained at various bending angles without any degradation of either electrodes or functional thin film.....   | 56 |
| Figure 30. Electroforming Process of the fabricated device for the creation of conductive channel between top and bottom electrodes before observing repeatable bipolar resistive switching effect in them.....   | 57 |
| Figure 31. Characteristic bipolar resistive switching curves of as prepared non-volatile flexible memory device based on hybrid hBN-MoS <sub>2</sub> QDs nanocomposite (a) I-V characteristic curve of 42 μm device (b) I-V characteristic curve of 70 μm device (c) I-V characteristic curve of 100 μm device (d) Switching ratio vs applied biased voltage showing their inverse relation (e) Optical images of the prepared devices with three different sizes of 100 μm, 70 μm and 42 μm from left to right respectively with a scale bar of 50 μm .....  | 58 |
| Figure 32. Durability of memory device based on all 2D functional layer against multiple voltage sweeps and for several hours along with cumulative probability plots of resistance and threshold voltages a) Electrical endurance for 1000 voltage sweeps without any considerable deviation b) High retentivity with high stability in both resistive states of all the three devices c) Cumulative probability plot of LRS and HRS d) Cumulative Probability curve of threshold voltages showing minor deviation.....  | 59 |
| Figure 33. Typical bipolar I-V curves of all the three memory devices with different sizes of 42 μm, 70 μm, and 100 respectively plotted against each other to clearly observe the difference between their   |    |

|  |    |
|--|----|
| switching ratios. LRS of all the devices is same however HRS tend to decrease with increasing device size hence resulting in smaller switching ratio .....   | 60 |
| Figure 34. Schematic diagram of various stages of filament formation and rupture and its verification by temperature and device dependence of bistable resistive states. a) (i) Electrons are depleted from the top electrode followed by the injection of $\text{Ag}^+$ cations into the active layer (ii) Injected $\text{Ag}^+$ cations travel slowly within the active layer and thus they are reduced by the nearby trapped electrons. This causes the growth of Ag filament as an extension of top electrode (iii) The filament growth continues until it connects top electrode with bottom electrode hence switching the device into ON state (writing process) (iv) A bias of opposite polarity is applied to rupture the filament from its thinnest part near the bottom electrode to turn the device back to its OFF state (erasing process) b) Illustration of temperature dependence on the resistive states of the fabricated device c) Illustration of device size dependence on the resistive states of the fabricated device..... | 62 |
| Figure 35. Mechanical characterization of as fabricated flexible memory device a) Mechanical bending test for various bending diameters b) Endurance test for 1500 bending cycles at a fixed bending diameter of 10 mm without any major difference in the bistable resistance values c) Schematic diagram of flexible memory device in bend state with labelling of each part.....  | 65 |
| Figure 36. Electrical characterization of memory device a) Typical log I-V characteristic curve of a memristor showing bipolar resistive switching <b>b)</b> Endurance measurement showing excellent repeatability of 1 <sup>st</sup> , 500 <sup>th</sup> , and 1000 <sup>th</sup> cycle <b>c)</b> Typical I-V curves showing the bipolar resistive switching effect in all the 9 memory cells of a $9 \times 1$ array labeled as M1-M9 respectively <b>d)</b> Endurance of HRS and LRS at a reading voltage of 0.7 volt showing remarkable stability <b>e)</b> Retention of HRS and LRS measured over a longer period of time without any noticeable deviation at 0.7 volts <b>f)</b> Optical Image of as fabricated memory device on a flexible PET substrate in bend condition.....   | 67 |
| Figure 37. Cumulative Probability plot displaying highly stable and repeatable experimental values of both resistive states and threshold voltages for storing and removing data a) LRS and HRS b) Set and RESET voltage for writing and erasing data .....  | 68 |
| Figure 38. Double Logarithmic I-V curve showing the slopes for HRS and LRS with different values of slope. This plot can be divided into three distinguish regions as separated by the three different colors. In the red line region, ohmic conduction takes place as slope $\approx 1$ . The green line is the Child's law region as the slope value $\approx 3$ . The blue line shows the region of sharp current increase as slope $\approx 23$ where the device switches from HRS to LRS. ....  | 71 |
| Figure 39. Bendability measurements by using the in-house prepared bending machine showing the remarkable flexible properties of as prepared resistive switching device a) Endurance curve showing HRS and LRS values for 1500 bending cycles at a fixed diameter value of 10 mm b) Endurance plot clearly showing very less deviation in HRS and LRS with changing values of bending diameters in the range of 30 mm to 2 mm. The device behaved like an open circuit at a bending diameter of 2 mm. Optical images of as top and bottom electrodes at different values of bending diameters c) Before bending d) Appearance of micro-cracks in bottom electrode e) Development of a major crack in the bottom electrode and completely broken top electrode at a bending diameter of 2 mm resulting in the open circuit of memory device.....  | 73 |

## List of Tables

|  |    |
|--|----|
| Table 1. Optimized values spraying parameters to precisely control the film uniformity and thickness through EHD Atomization of WS <sub>2</sub> solution.....  | 29 |
| Table 2. Different spraying modes and their respective voltage range in which they appeared during EHD atomization of WS <sub>2</sub> solution .....   | 30 |
| Table 3. Optimized parameters and their fixed values used for patterning the top Ag electrode through EHD patterning .....   | 30 |
| Table 4. Optimized parameters for depositing atomically thin film of Al <sub>2</sub> O <sub>3</sub> through ALD along with complete details of used precursors such as TMA and H <sub>2</sub> O .....  | 31 |
| Table 5. Various modes of deposition along with the range of applied voltage difference from high-voltage power supply during EHDA of hBN/GQDs nanocomposite .....   | 33 |
| Table 6. Optimized values of various parameters for spraying functional thin film of GQDs-hBN 2D nanocomposite to control the film thickness and uniformity during EHDA .....  | 34 |
| Table 7. Optimized parameters for depositing atomically thin film of Al <sub>2</sub> O <sub>3</sub> through ALD along with complete details of used precursors such as TMA and H <sub>2</sub> O .....  | 35 |
| Table 8. Optimized values of various parameters to control the film thickness and uniformity during EHD Atomization of hBN/MoS <sub>2</sub> QDs nanocomposite .....  | 37 |
| Table 9. Various modes of deposition along with the range of applied voltage difference from high-voltage power supply during EHDA of hBN/MoS <sub>2</sub> QDs nanocomposite .....   | 38 |
| Table 10. Optimized condition and their set values during the deposition of top Ag electrode through RPC inkjet printing system patterning process of top Ag Electrode .....   | 39 |
| Table 11. Optimized values of various parameters to control the film thickness and uniformity during EHD Atomization of MoS <sub>2</sub> -PVA nanocomposite.....   | 41 |
| Table 12. Various Modes of Deposition along with the Range of Applied Voltage Difference from High-Voltage Power Supply during EHD Atomization of MoS <sub>2</sub> -PVA nanocomposite .....  | 41 |
| Table 13. Optimized condition and their set values during the deposition of top Ag electrode through EHD Patterning Process of Top Ag Electrode.....   | 43 |
| Table 14. Comparison of various resistive switching device parameters of as fabricated memory device with other hybrid and non-hybrid nanocomposite active layer materials .....   | 66 |
| Table 15. Comparison of MoS <sub>2</sub> -PVA nanocomposite based memristive device with already reported memory devices based on PVA nanocomposites. It is evident from the illustrated results that MoS <sub>2</sub> flakes play a vital role in improving the electrical properties of PVA based memory devices.....  | 74 |
| Table 16. Comparison of MoS <sub>2</sub> -PVA nanocomposite based memristive device with already reported memory devices based on nanocomposites of MoS <sub>2</sub> semiconductor with other materials. It is evident from the illustrated results that PVA has enhanced the retention time and mechanical strength MoS <sub>2</sub> based memory device..... | 74 |

# Contents

|  |      |
|--|------|
| <b>Abstract</b> .....  | xiii |
| <b>1. Introduction</b> .....   | 1    |
| 1.1 Two Dimensional Materials.....   | 1    |
| 1.2 Role of 2D Materials in RRAM Devices.....  | 3    |
| 1.2.1 Graphene and its Nanocomposites.....   | 3    |
| 1.2.2 MoS <sub>2</sub> and its Nanocomposites.....   | 4    |
| 1.2.3 Other 2D Materials and their Nanocomposites.....                                     | 4    |
| 1.3 Printing Technologies.....   | 5    |
| 1.3.1 Reverse Offset Electrode Patterning.....   | 5    |
| 1.3.2 Electrohydrodynamic Patterning and Atomization.....                                  | 7    |
| 1.3.3 Reciprocating Inkjet Head for Electrode Patterning.....                              | 8    |
| 1.3.4 Electrohydrodynamic Atomization for Thin Film Deposition.....                        | 10   |
| <b>2 Experimental</b> .....  | 11   |
| 2.1 Synthesis of functional materials.....   | 11   |
| 2.1.1 Synthesis of WS <sub>2</sub> flakes.....   | 11   |
| 2.1.2 Synthesis of MoS <sub>2</sub> flakes blended with PVA.....                           | 13   |
| 2.1.3 Synthesis of hBN flakes blended with GQDs.....                                       | 14   |
| 2.1.4 Synthesis of hBN flakes blended with MoS <sub>2</sub> QDs.....                       | 17   |
| 2.2 Surface Characterizations.....   | 18   |
| 2.2.1 Surface Morphology.....  | 18   |
| 2.2.2 Compositional Characterization.....  | 22   |
| 2.2.3 Optical Characterization.....  | 25   |
| 2.2 Fabrication of flexible RRAM devices.....  | 27   |
| 2.2.1 Fabrication of Ag/WS <sub>2</sub> /Ag RRAM.....                                      | 27   |
| 2.2.2 Fabrication of Ag/hBN-GQDs/Ag RRAM.....  | 31   |
| 2.2.3 Fabrication of ITO/hBN-MoS <sub>2</sub> QDs/Ag RRAM.....                             | 36   |
| 2.2.4 Fabrication of Ag/MoS <sub>2</sub> -PVA/Ag RRAM.....                                 | 39   |
| <b>3 Resistive switching in as synthesized 2D materials and their nanocomposites</b> ..... | 43   |
| 3.1 Flexible Ag/WS <sub>2</sub> /Ag RRAM.....  | 43   |
| 3.1.1 Electrical Characterization.....   | 43   |
| 3.1.2 Conduction Mechanism.....  | 46   |
| 3.1.3 Mechanical Characterization.....   | 48   |

|  |    |
|--|----|
| 3.2 Flexible Ag/hBN-GQDs/Ag RRAM.....                  | 49 |
| 3.2.1 Electrical Characterization.....                 | 49 |
| 3.2.2 Conduction Mechanism .....                       | 52 |
| 3.2.3 Mechanical Characterization.....                 | 55 |
| 3.3 Flexible ITO/hBN-MoS <sub>2</sub> QDs/Ag RRAM..... | 57 |
| 3.3.1 Electrical Characterization.....                 | 57 |
| 3.3.2 Conduction Mechanism .....                       | 60 |
| 3.3.3 Mechanical Characterization.....                 | 63 |
| 3.4 Flexible Ag/MoS <sub>2</sub> -PVA/Ag RRAM .....    | 66 |
| 3.4.1 Electrical Characterization.....                 | 66 |
| 3.4.2 Conduction Mechanism .....                       | 68 |
| 3.4.3 Mechanical Characterization.....                 | 72 |
| 4. Conclusions and Future work .....                   | 75 |
| 4.1 Conclusions.....                                   | 75 |
| 4.2 Future work.....                                   | 75 |
| References.....  | 77 |

## Abstract

In this study, 2D materials and their nanocomposites have been explored as the functional layer of resistive random access memory (RRAM) devices. 2D materials and their nanocomposites such as molybdenum disulfide-polyvinyl alcohol (MoS<sub>2</sub>-PVA), hexagonal boron nitride flakes-MoS<sub>2</sub> quantum dots (hBN-MoS<sub>2</sub>QDs), flakes of tungsten disulfide (WS<sub>2</sub>) and hBN flakes-graphene quantum dots (hBN-GQDs) have been sandwiched between two metallic electrodes to complete the simple structure of RRAM devices. All-Printed technology was used to fabricate each RRAM device on a flexible and transparent substrate. All the devices displayed highly stable, repeatable and bipolar resistive switching characteristics. The least switching ratio was shown by the active layer of MoS<sub>2</sub>-PVA ( $1.28 \times 10^2$ ) while hBN-MoS<sub>2</sub>QDs, WS<sub>2</sub> and hBN-GQDs exhibited a superior value of  $10^3$  each. Lowest retention time of  $10^4$  s was exhibited by the WS<sub>2</sub> flakes while MoS<sub>2</sub>-PVA, hBN-MoS<sub>2</sub>QDs, and hBN-GQDs showed a higher value of  $10^5$  s each. All 2D materials based flexible RRAM devices were tested for their bendability in the bending diameter range of 500 mm to 2 mm. Functional layer of MoS<sub>2</sub>-PVA showed maximum number of bending cycles (2000 cycles) without any prominent decay in the device performance while hBN-MoS<sub>2</sub>QDs, WS<sub>2</sub> flakes and hBN-GQDs exhibited mechanical robustness upto 1500 cycles each respectively. Conduction mechanism shown by active layers of MoS<sub>2</sub>-PVA and WS<sub>2</sub> flakes was space charge limited current (SCLC) while conductive filaments were formed in the active layer of hBN-GQDs and hBN-MoS<sub>2</sub>QDs. Furthermore, functional thin films of hBN-GQDs and WS<sub>2</sub> flakes were also encapsulated with atomically thin film of aluminum oxide (Al<sub>2</sub>O<sub>3</sub>) through spatial atmospheric atomic layer deposition (SAALD) system to enhance their lifetime. These obtained results clearly illustrate that functional layers based on 2D materials have a huge potential to replace the existing nanomaterials used as active layers of RRAM devices.

# 1. Introduction

## 1.1 Two Dimensional Materials

2D materials such as graphene, transition metal dichalcogenides (TMDs) and diatomic hexagonal boron nitride (hBN) with zero, intermediate and large bandgaps respectively are under extensive research now a days because of their promising properties [1]. These layered materials are attractive for researchers due to their unique electrical, mechanical, chemical, optical and thermal properties. 2D materials offer utmost mechanical strength with high flexibility yet extremely light weight [1–3]. Graphene was the pioneer 2D material that revolutionized the world of electronics ever since its advent owing to its unique mechanical [4], thermal [5], magnetic [6], semiconducting [7], optoelectronic [4,8], and superconducting [9] properties. Graphene sheets have extremely high metal like conductivity owing to their vast Bohr radius with zero band-gap [10] however, an intermediate band-gap in pristine graphene sheets can be introduced by synthesizing GQDs and nanoribbons through exfoliation. GQDs have already shown encouraging results in various applications such as light emitting diodes [11], photodetectors [12], supercapacitors [13], and photovoltaic solar cells [14] owing to their edge states and variable quantum confinement effect. Moreover, surface/volume ratio of GQDs is higher than carbon nanodots.

TMDs are another class of 2D materials that have already been successfully employed in various electronic device applications such as field effect transistors (FETs) [15], lasers [16], photovoltaic solar cells (PVSC) [17], photo diodes [18], etc. Unlike, highly conductive graphene, TMDs are semiconducting layered materials whose conductivity varies with the number of exfoliated layers. These semiconducting materials have an added advantage of easy synthesis through several methods such as liquid phase exfoliation and mechanical cleavage owing to weak van der Waals bonding between their atoms [19]. Furthermore, these materials are physically and chemically

stable. Among these 2D materials, MoS<sub>2</sub> is a very attractive candidate with an immense potential to be used in electronic device applications because of its suitable quantum confinement, high mobility owing to direct band gap of 1.85 eV in monolayer, and indirect bandgap of 1.29 eV in multilayer<sup>7</sup>. MoS<sub>2</sub> has 1T (metallic phase), 2H (hexagonal symmetry), 3R (rhombohedral) and other phases due to single, double, triple and multilayers stacked over each other respectively. Sulfur-molybdenum-sulfur having hexagonal structure are sandwiched over one another. TMDs are promising 2D materials that can be divided into several categories based on the combination of transition metal (Mo, Nb, Re, Ni, W or V) and chalcogen (Se, S, or Te) [20]. Properties of TMDs heavily depend on the number of layers in a nanosheet such as pristine or a few layer MoS<sub>2</sub> has an indirect bandgap of ~1.3 eV while monolayer MoS<sub>2</sub> has a direct bandgap of 1.9 eV [21]. Mobility of MoS<sub>2</sub> is as high as that of a single crystal of silicon with this bandgap [2]. Owing to the quick progress of TMDs to be used in the future electronic device applications, various techniques to synthesize monolayer and a few layer MoS<sub>2</sub> flakes have been explored. These methods include micromechanical exfoliation, hydrothermal process, solution-based chemical exfoliation, chemical vaporization, ion intercalation exfoliation, and sulfurization of molybdenum (Mo) [22–26]. Exfoliated MoS<sub>2</sub> semiconductor has already shown remarkable electrical properties and mechanical strength in various micro electronic device applications such as lasers [27], supercapacitors [28], thin film transistors (TFTs) [29], phototransistors [30], bio sensors [31], solar cells [32], and batteries [33].

Among other promising 2D materials, hBN and tungsten disulfide (WS<sub>2</sub>) are most famous for their known properties. hBN has a substantially high elastic constant (503 N m<sup>-1</sup>) and breaking strength (15.7 N m<sup>-1</sup>) to show excellent applications in flexible electronic devices [34]. Furthermore, hBN is a hydrophobic material implying that electronic devices fabricated by using this 2D material



will remain protected in humid conditions. Other distinct characteristics of hBN include high temperature stability, large surface area, high mechanical strength, hydrophobicity (water repellent) and large thermal conductivity. As per  $WS_2$  is concerned, its atomic structure is similar to  $MoS_2$  with the exception of Molybdenum (Mo) atom being replaced with tungsten (W) atom but  $WS_2$  has relatively lighter effective mass, high thermal and chemical stability, making it superior to other available TMDs. Furthermore,  $WS_2$  has distinct pressure-tunable properties with the ability to bear extreme load that makes it a promising candidate for flexible electronic device applications as high mechanical strength is an inherent property of all 2D materials.

## 1.2 Role of 2D Materials in RRAM Devices

### 1.2.1 Graphene and its Nanocomposites

Due to its zero bandgap, graphene can not be used as the active layer of RRAM devices. However, graphene has been used as the transparent and highly conductive electrode in various RRAM devices. Moreover, synthesis of GQDs through exfoliated graphene sheets can play a vital role in the resistive switching characteristics of RRAM devices. Recently, effect of embedding various conductive nanoparticles (NPs) such as Au NPs [35], CdSe NPs [36], and CdSe/ZnS NPs [37] on the characteristics of memory devices with typical sandwich structure have shown promising results. GQDs are considered as a superior choice to be used as the functional material for flexible nonvolatile memory (NVM) applications as compared to other nanoparticles owing to their remarkable characteristics of chemical inertness, high conductivity, excellent solubility, huge flexibility, and enhanced surface grafting [38,39]. Moreover, the edge and quantum confinement effect of the GQDs induces several physical and chemical properties that are highly suitable for a charge-trapping medium [40].

### 1.2.2 MoS<sub>2</sub> and its Nanocomposites

These theoretical predictions provide strong motivation for further experimental research on the applications of layered materials in flexible electronic memory devices. Atomic level thickness of TMDs make them an attractive class of materials for electronic device applications such as flexible memory devices owing to their exotic optical, thermal, mechanical, chemical and electrical properties [41]. The properties that make TMDs a preferred choice as the functional material of a memory device includes their tunable band gap that transforms from indirect to direct band gap with varying crystal thickness. This band gap (1.1 eV-2 eV) is ideal for memory applications with clearly defined ON/OFF states and reliable data storage. Although various contributions have already been reported to use MoS<sub>2</sub> in various electronic device applications as mentioned above, but the resistive switching characteristics of this 2D material in the form of a RRAM device in particular has yet to be completely explored. A lot of research is ongoing to explore the unique nanocomposite materials with memory effect owing to its potential of replacing transistor from memory devices [42–46]. Nanospheres, monolayer, and multilayer flakes of MoS<sub>2</sub> have recently been reported to exhibit remarkable resistive switching properties with a very high off/on ratio of up to 10<sup>6</sup> and reproducibility of 10<sup>4</sup> voltage sweeps [47–51]. Juqing Liu et al. [51] and Sachin M. Shinde et al. [48] have recently reported appreciable results of resistive switching by using a combination of exfoliated MoS<sub>2</sub> flakes with a polymer.

### 1.2.3 Other 2D Materials and their Nanocomposites

Graphene was the first 2D nano-material with promising applications but it has a limitation of zero bandgap that does not allow it to be used as a memory device. Emergence of a sister 2D material, hBN saved the overwhelming reputation of layered materials by offering extremely high bandgap

of  $\approx 5.9$  eV thus, making it an ideal functional material for memory applications [52]. Chemical structures of graphene and hBN are similar except that carbon atoms in the honeycomb of graphene are replaced with nitrogen atoms [51]. In spite of such attractive qualities, hBN based memory device can result in high power consumption, low current density and high threshold voltage ( $V_{th}$ ) owing to its large bandgap and lower conductivity. To overcome the deficiency of low conductivity in hBN due to its large bandgap, MoS<sub>2</sub> can be used to form a blend. WS<sub>2</sub> is another 2D material with potential application of resistive switching memory. Electron affinity values for WS<sub>2</sub> lies between 4 eV to 4.4 eV and it has an indirect band gap ( $E_g = 1.3$  eV) [53]. WS<sub>2</sub> is most probably a suitable choice to be used as the functional layer of a memory device due to the absence of states for charge leakage through quantum mechanical tunneling resulting in large retention of stored digital data [54]. Additionally, 2D electron-electron links among W atoms of WS<sub>2</sub> layers would assist in improving planar electronic transportation characteristics of charge carriers. WS<sub>2</sub> is preferred over other TMDs owing to its relatively larger band gap in both monolayer ( $\sim 1.3$  eV) and bulk ( $\sim 2.1$  eV) form as compared to MoS<sub>2</sub>, MoSe<sub>2</sub>, and WSe<sub>2</sub> which is a vital entity for any nonvolatile memory device [19]. WS<sub>2</sub> has the ability to act as a highly efficient and ultrafast interlayer for electron transfer.

## 1.3 Printing Technologies

### 1.3.1 Reverse Offset Electrode Patterning

In order to achieve fine patterns with high resolution, more accurate micro-fabrication technology is required. Moon et al. reported a novel direct contact method known as reverse offset printing for patterning high quality metal electrodes. This patterning technique has the ability to print extremely tiny and complicated structures with uniform thickness [55]. Electrodes printed through reverse offset roll-to-plate printing technique have the promising characteristics of high resolution,

low resistivity, high quality surface, simplicity, and ease of fabrication to realize an accurate and precise pattern [56]. It is a direct printing method that can print electrodes with pattern size  $< 1 \mu\text{m}$  unlike its other competitive direct printing techniques such as screen printing, flexographic printing, gravure printing and inkjet printing.

Complete schematic diagram of reverse offset patterning system is illustrated in Fig.1. Accessories of reverse offset printing system include a glass slide to deposit ink, a roller enfolded with a blanket of highly hydrophobic poly-dimethylsiloxane (PDMS) material, a cliché designed with the negative of electrode patterns engraved on its surface and finally the desired substrate on which the device has to be fabricated. In order to achieve high resolution micro patterns, large pressure and low speed are the desired parameters. The area of blanket roll known as nip which remains in continuous contact with the plate, cliché or desired substrate is extremely important as transfer of ink from or to the blanket roll occurs in this area<sup>1</sup>. Adhesion and cohesion of each surface is also an important parameter which should be optimized by controlling the pressure and speed of the blanket roll. Ink adheres to the roll and separated from the surface at the end of contact.

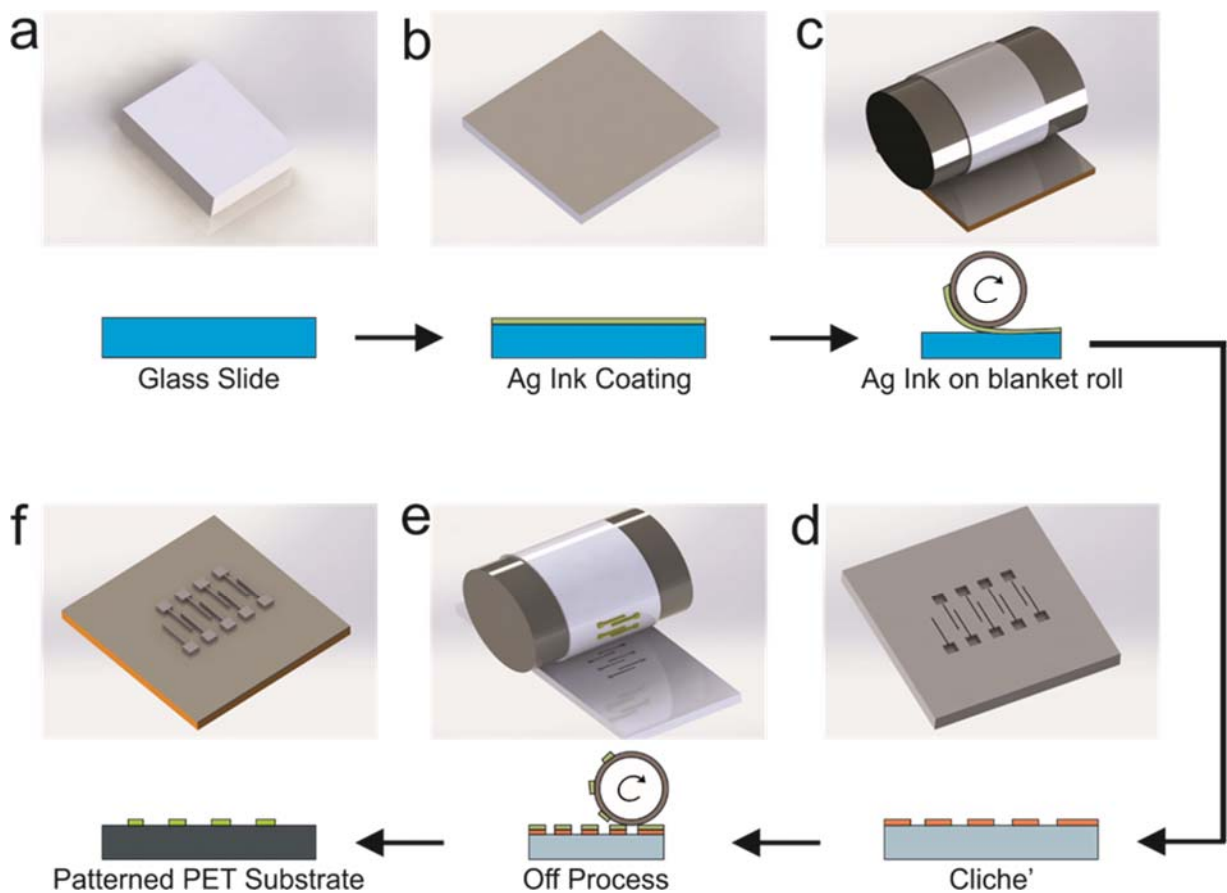


Figure 1. 3D and 2D view of Reverse Off-Set schematic diagram illustrating the patterning of bottom Ag electrodes on flexible PET substrate a) Glass slide b) Ag nanoparticles ink spin coated on glass slide c) Ag ink being attached with the PDMS blanket by rolling the blanket roll over Ag coated glass slide d) Cliché showing the engraved patterns on its surface e) OFF Process taking place in which engraved patterns of cliché are being transferred onto PDMS blanket f) SET Process in which Ag electrodes are transferred from blanket roll onto the desired PET substrate

### 1.3.2 Electrohydrodynamic Patterning and Atomization

Electrohydrodynamic (EHD) patterning is a non-contact printing technique used for patterning high resolution metallic electrodes with uniformity. EHD patterning is preferred over other contact based patterning techniques such as screen printing, reverse offset and gravure offset because they could damage the functional thin film resulting in a short circuit between top and bottom electrodes. However, on the other hand EHD patterning is a non-contact method for patterning electrodes that does not make any contact with the functional thin film while depositing top electrodes on its surface. EHD patterning is accomplished by applying a high electric field at the tip of the nozzle.

This applied electric field directly effects the flow of liquid being deposited through the nozzle to form the desired jet. Before the application of electric field, a hemispherical drop of the liquid is formed on the meniscus which adopts the form of a cone when potential difference is applied between the nozzle and substrate. Ions with the same polarity are mobilized and gather at the meniscus surface. This cone formation can be depicted by the stability between the surface tension and applied electrostatic forces. Single jet with extremely thin diameter is ejected from the tip of the cone to print on the targeted substrate when the electrostatic forces surpass the specific limit of surface tension. These deposition conditions can be used to pattern various type of electrodes based on different materials on flexible and rigid substrates. The desired dimensions of the patterned electrodes can be controlled by varying a few parameters such as flow rate, applied voltage, nozzle diameter and standoff distance. Properties of the ink like conductivity, viscosity, density and surface tension also play a vital role. The mode of deposition can be either drop on demand or continuous depending on the value of applied voltage.

### 1.3.3 Reciprocating Inkjet Head for Electrode Patterning

Reciprocating (RPC) inkjet head is another non-contact based patterning technique for depositing metallic electrodes in circular and straight line form with desirable dimensions. The whole schematic diagram of RPC inkjet printing system during each patterning step is presented in Fig. 2. RPC inkjet printing system is preferred over other patterning techniques owing to its high controllability, compatibility with flexible substrates and high precision without damaging the functional layer. Unlike continuous drop on demand (DOD) method,  $\mu$ -droplets from RPC inkjet printing system are only generated when they are required. The capillary force keeps the high viscosity metallic nanoparticle ink inside the chamber while a pneumatic actuator is used to dispense the droplets.

Reciprocating inkjet has the ability to deposit inks with various drop sizes ranging from 10  $\mu\text{m}$  to 1mm. This wide range of deposited drop size is ascribed to the mechanical extrusion mechanism followed by this electrode patterning technology whereas the controllability over the electrode size is mainly dependent upon the needle diameter. A disadvantage of this electrode patterning technique is that its printing frequency is characteristically limited to 1-20 Hz due to the mechanical reciprocating manner movement of the micro needle. Frequency of reciprocating head is significantly lower than that of inkjet printing, which normally operates at 1-10 kHz. Optimized values of various parameters such as ink viscosity, standoff distance, nozzle diameter, and deposition frequency need to be considered for highly controllable, precise and repeatable patterning of  $\mu$ -droplets. These  $\mu$ -droplets are sintered by UV laser in real time followed by thermal sintering to enhance conductivity.

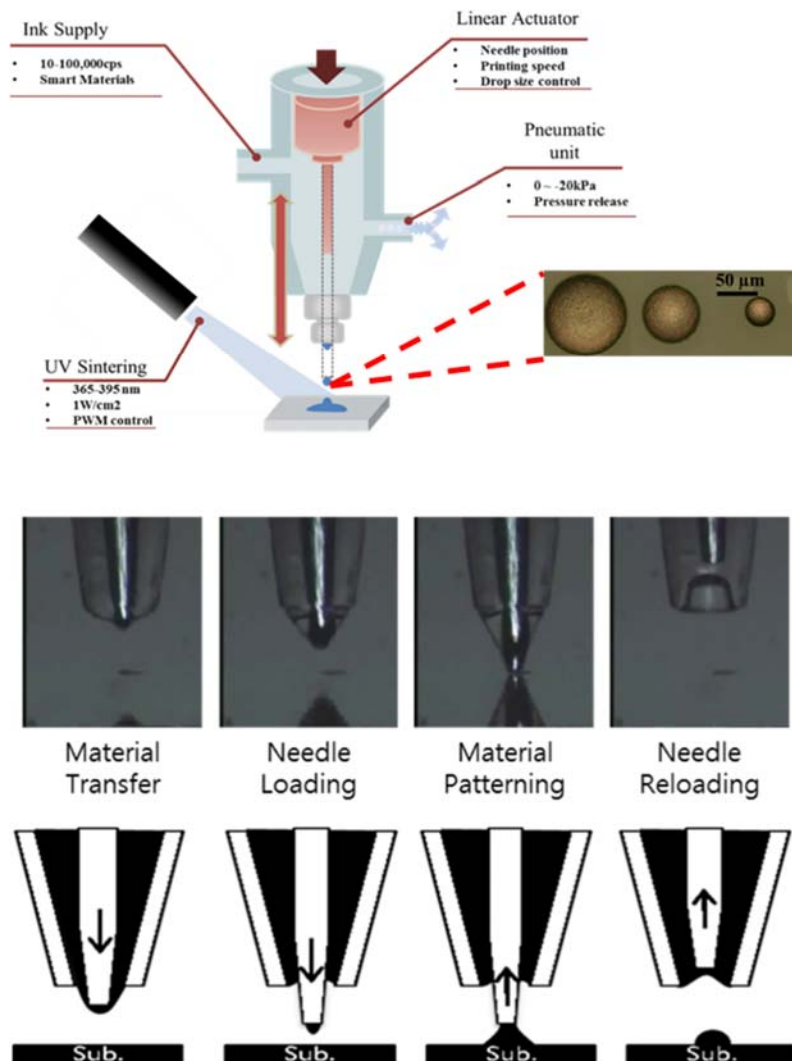


Figure 2. Schematic diagram of reciprocating (RPC) inkjet printing system and illustration of each fabrication step with optical images of three different size circular top electrodes

### 1.3.4 Electrohydrodynamic Atomization for Thin Film Deposition

EHDA is preferred over other active layer deposition techniques due to its high control, simplicity, large area coverage and ability to produce very thin films with high uniformity in quick time [57,58]. Complete schematic diagram of EHDA system with labelling of each part and an example of its operating envelop are shown in Fig. 3. The functional thin film solution is allowed to flow through the meniscus of the nozzle by applying the electric field. The flow rate can be varied to



achieve the stable cone jet for deposition of uniform thin film in the desired area over the surface of target substrate. Active material ink being sprayed begins to split into small droplets with increasing voltage. Spraying modes varies from dripping to multi-stable jet after passing through micro-dripping, unstable jet and stable jet. The spraying mode can be controlled by several parameters such as applied voltage, distance of nozzle from the substrate, nozzle diameter and set value of flow rate. The operating envelope of depositing the functional thin film can also be drawn by recording the data of respective deposition condition. Film thickness can be controlled by optimizing the number of spraying passes, spraying time, speed of stage and standoff distance between the nozzle and desired substrate.

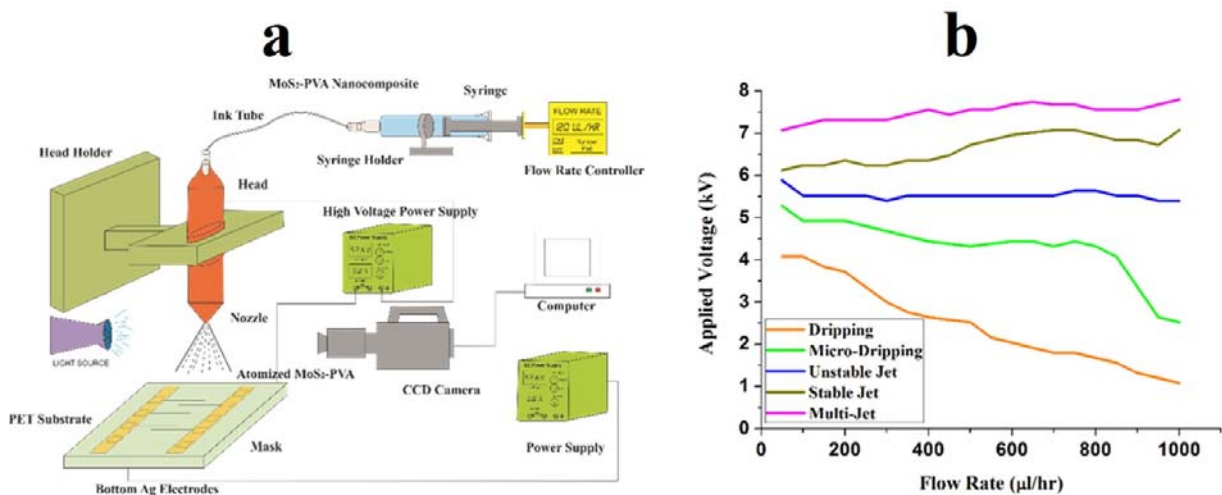


Figure 3. a) Schematic diagram of EHDA process with labelling of each part b) Operating envelope of EHDA process for the deposition of functional thin film.

## 2 Experimental

### 2.1 Synthesis of functional materials

#### 2.1.1 Synthesis of WS<sub>2</sub> flakes

Pristine WS<sub>2</sub> (99.0%) ultrafine powder was purchased from Graphene Supermarket. Solvents NMP and acetone for exfoliation of WS<sub>2</sub> flakes were purchased from Sigma Aldrich. Exfoliation of

pristine WS<sub>2</sub> flakes was carried out by liquid exfoliation method using co-solvent approach as compared to mechanical method of scotch tape micro cleavage to achieve high throughput. First of all, the pristine WS<sub>2</sub> was ground in a mortar for 2 h by adding a few drops of NMP solvent. The gel like mixture was then dried and dispersed in equal volume ratio of NMP and acetone. This solution was sonicated through ultrasonic probe sonication with pulse on 3 s and pulse off 1 s with a frequency of 20 kHz. The resultant solution was kept unstirred for overnight and  $\frac{3}{4}$ <sup>th</sup> portion of the suspension was centrifuged at 3000 rpm for 1 h. After centrifugation, the supernatant was taken out and stirred for 24 h. Before the deposition of thin film, the stability of the solution was evaluated by sedimentation test by allowing the solution stand undisturbed for 72 h; slower the particles settle, the better the solution stability is. Furthermore, the resultant exfoliated solution of WS<sub>2</sub> flakes found to be stable even after 8 weeks. The as prepared solution was used for thin film fabrication and further characterizations. The molecular structure of a few layer WS<sub>2</sub> flakes along with its as synthesized exfoliated solution ink bottle are shown in Fig. 4.

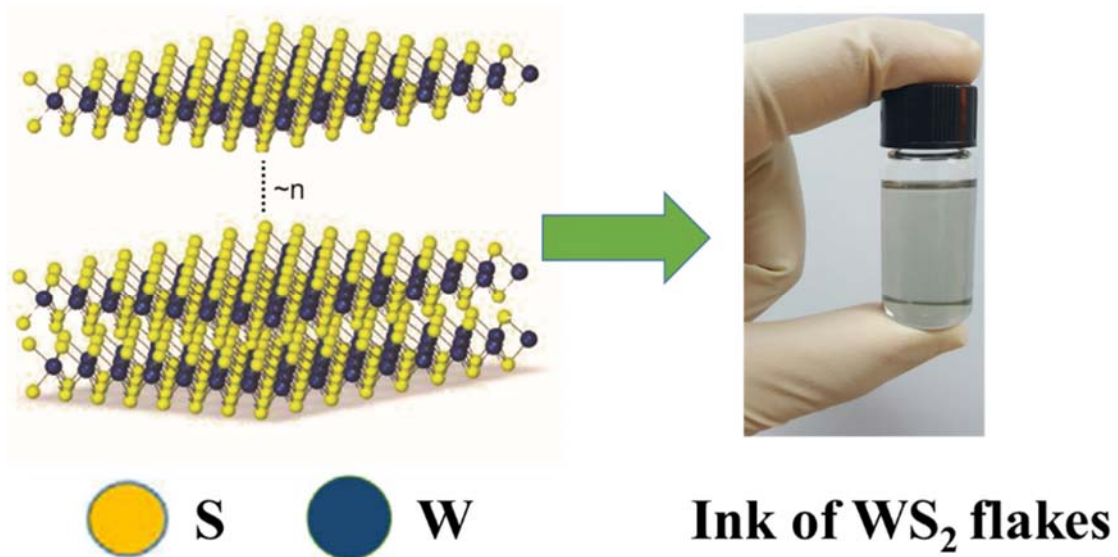


Figure 4. Chemical structure and as synthesized ink of a few layered WS<sub>2</sub> material

### 2.1.2 Synthesis of MoS<sub>2</sub> flakes blended with PVA

Pristine MoS<sub>2</sub> (99.0%) ultrafine powder was purchased from Graphene Supermarket. PVA (MW 9000–10000, 80% hydrolyzed) and NMP (anhydrous, 99.5%) were purchased from Sigma Aldrich. Liquid exfoliation method was used for the synthesis of MoS<sub>2</sub> flakes compared to mechanical method of scotch tape micro cleavage to achieve high throughput. Lateral flake size and thickness of raw flakes are affected by the selected exfoliation process. NMP was selected as the solvent for dispersing MoS<sub>2</sub> in PVA. NMP is a suitable choice for exfoliating MoS<sub>2</sub> powder due to its surface energy that matches well with the nanosheets of MoS<sub>2</sub>. The surface tension helps in overcoming the van der Waals forces resulting in ease of exfoliation. Grinding of pristine MoS<sub>2</sub> powder in NMP was carried out for 1 h in a mortar followed by heating at 100 °C for 1 h to evaporate the solvent. Furthermore ground MoS<sub>2</sub> was dispersed in NMP for probe sonication for 1 h as grinding and sonication both are effective in exfoliation of MoS<sub>2</sub> flakes [59]. Finally centrifugation at 6000 rpm was carried out for 30 min to remove the larger nanoplatelets and partially exfoliated crystallites. The supernatant was collected and PVA (10 wt. %) was dissolved in it. The blend solution of MoS<sub>2</sub> and PVA was stirred on a magnetic stirrer at 1000 rpm at ambient conditions for overnight to observe if there are some undissolved suspensions left. The resulting homogeneous and uniformly dispersed nanocomposite of MoS<sub>2</sub> with PVA in NMP was used for device fabrication. The dispersion remained stable over a period of several months and no suspension or segregation was observed. The molecular structures of PVA and MoS<sub>2</sub> along with the resulting hybrid nanocomposite ink bottle are shown in Fig. 5.

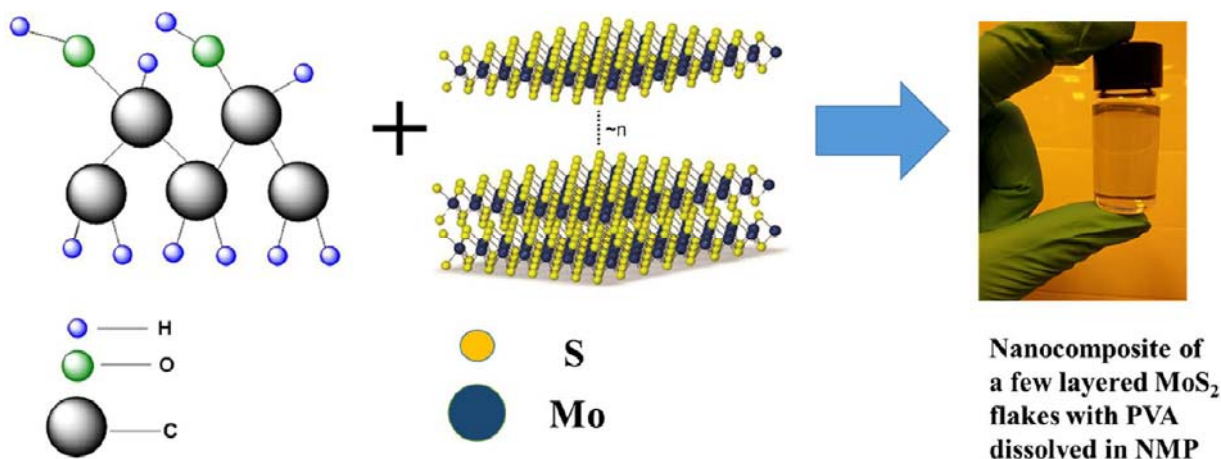


Figure 5. Chemical structures of dielectric PVA polymer and semi-conductive pristine MoS<sub>2</sub> displaying their interatomic bonding along with the as synthesized exfoliated few layered MoS<sub>2</sub> flakes ink with PVA dissolved in NMP solvent

### 2.1.3 Synthesis of hBN flakes blended with GQDs

Graphene nano platelets (GNPs) (Purity > 99%, Diameter: 1-2  $\mu\text{m}$ , Grade: 4) were used for the synthesis of Graphene quantum dots and were purchased from Cheap Tubes Inc. Boron Nitride (BN) ultrafine powder (Purity: 99.0%, Average particle size:  $\sim 70$  nm) was purchased from Graphene Supermarket. N-Methyl-2-pyrrolidone (NMP), 1, 2-dichlorobenzene (DCB) and isopropyl alcohol (IPA) were purchased from Sigma Aldrich. The chemical structures of the used 2D materials and their nanocomposite is illustrated in Fig. 6 below along with their as synthesized inks. In brief, GQDs were synthesized from GNPs by wet grinding the nano powder for 6 h using mortar and pestle assisted by adding a few drops of NMP. The gel like mixture was obtained which was dried at 100  $^{\circ}\text{C}$  for 1 h. The dried powder was then dispersed in equal volumes of NMP and DCB and placed on a mechanical shaker for 3 h for vigorous mixing followed by ultra-sonication in a bath sonicator for 4 h. Further sonication was conducted by probe-type sonicator at 30 % amplitude for 1 h with shorter pulses of sonication (pulse on: 3 s, pulse off: 1 s).

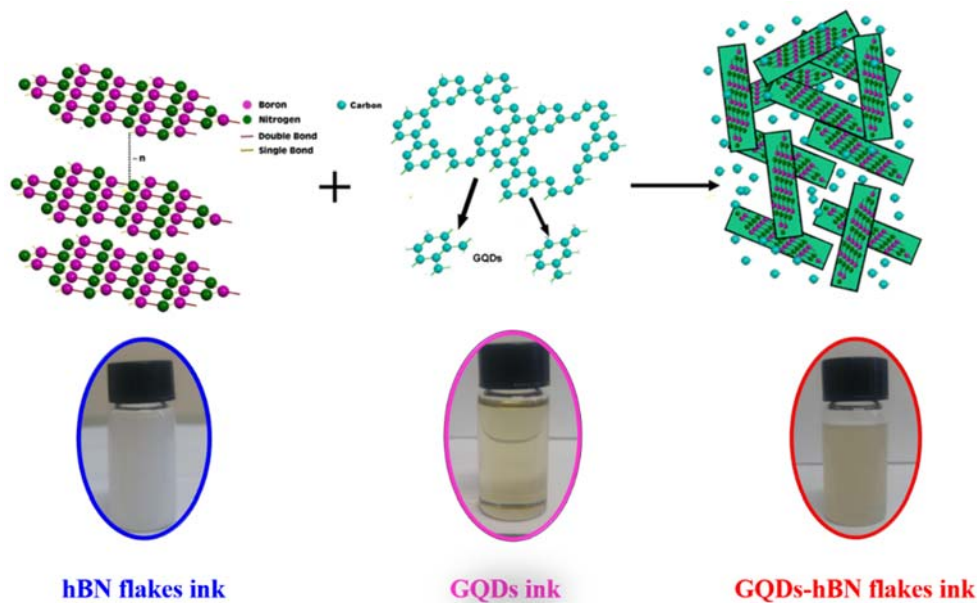


Figure 6. Chemical structures of as synthesized 2D materials including hBN flakes, GQDs and their nanocomposite. The prepared inks of each material in their respective solvents is shown at the bottom of each chemical structure

The ultra-sonicated solution was kept unstirred for overnight and top 2/3<sup>rd</sup> portion of the solution was taken for centrifugation which was carried out at 10000 rpm for 30 min. Finally, the supernatant with a faint yellow color was collected in a separate bottle with a concentration of 7 mg/ml of GQDs in it. The chemical structure and optical image of GQDs ink are illustrated in Fig. 6. Pristine ultrafine powder of hBN was exfoliated to obtain nanosheets through liquid exfoliation method assisted by grinding and ultrasonic vibration [60]. Initially, the pristine hBN powder was ground for 2 h in IPA followed by ultrasonic vibration via bath-sonication and probe-sonication each for 1 h. After drying the wet ground powder, the dried hBN powder was dispersed in IPA because IPA is considered the better solvent to exfoliate and disperse hBN as compared to other organic solvents [61]. Furthermore, to obtain the exfoliated thin nanosheets of hBN, the resulted solution was centrifuged at 4000 rpm for 30 min and then supernatant was collected containing the thin nanosheets of hBN. The as prepared solution of exfoliated hBN nanosheets appeared to

be milky white in color as can be seen in Fig. 6 and remained stable even after 6 weeks of its preparation.

The as prepared solution of hBN thin nanosheets was used to prepare 2D nanocomposite with as synthesized GQDs which was the critical objective of this research work in exploring the resistive switching effect of this 2D nanocomposite. The resulted solutions of GQDs and hBN nanosheets were mixed in equal volumes and placed on a magnetic stirrer for overnight to attain the homogeneous mixing and it was observed that both the solutions are thoroughly mixed and stable while all the solvents i.e. NMP, DCB and IPA remained miscible to form a turbid color stable solution as illustrated in Fig. 6. The whole method of forming this advanced 2D nanocomposite is illustrated schematically in Fig. 7 with appropriate color code.

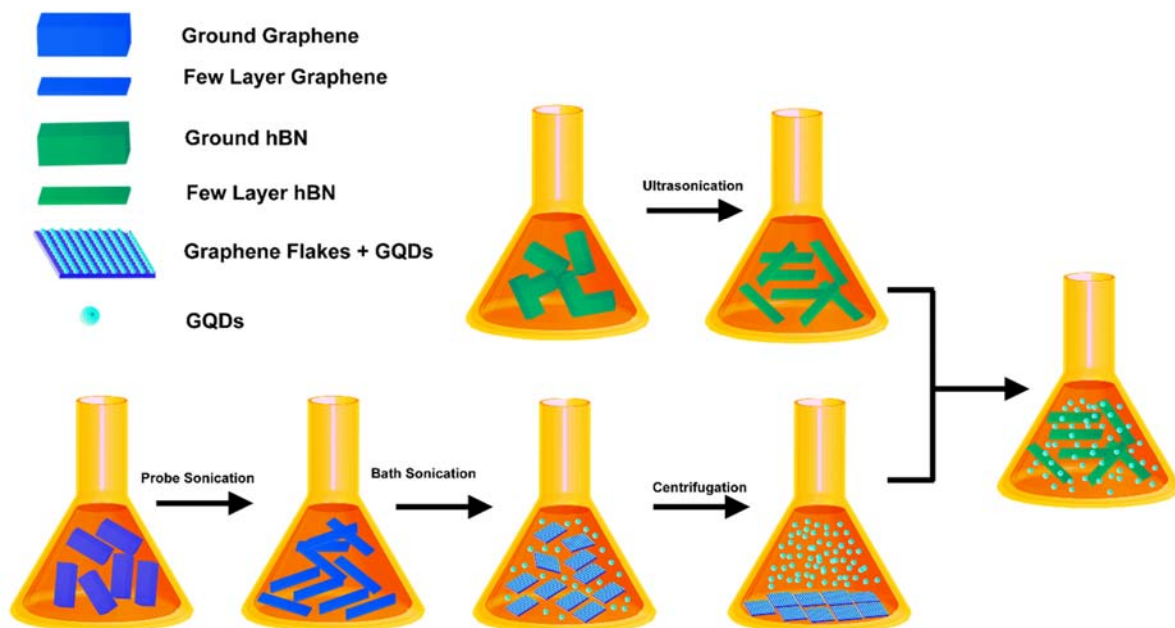


Figure 7. Complete process of synthesizing an all 2D GQDs-hBN nanocomposite ink with proper color scheme. The synthesis of hBN flakes are illustrated in the upper part while GQDs synthesis is shown in the lower part of diagram.

#### 2.1.4 Synthesis of hBN flakes blended with MoS<sub>2</sub>QDs

For the synthesis of MoS<sub>2</sub> QDs, ultrafine MoS<sub>2</sub> crystalline powder was purchased from Graphene Supermarket (average particle size: ~90 nm, purity: 99.0%). For the preparation of h-BN flakes, the BN ultrafine powder was also purchased from Graphene Supermarket (average particle size: ~70 nm, purity: 99.0 %). All the solvents including N-Methyl-2-pyrrolidone or NMP (99.5%), 1, 2-dichlorobenzene or DCB (99.0%) and isopropyl alcohol or IPA were purchased from Sigma Aldrich. MoS<sub>2</sub> QDs were prepared by the same method as reported in our previous work [59,62]. Briefly, the method involves wet grinding of pristine MoS<sub>2</sub> powder in a mortar for 6 h with NMP solvent. After drying the ground powder, it was dispersed in equal volumes of NMP and DCB followed by mechanical shaking (4 h), bath sonication (4 h), ultrasound probe sonication (1 h), and centrifugation (30 min, 8000 rpm).

The liquid based chemical exfoliation of pristine hBN was carried out in isopropyl alcohol (IPA) to obtain maximum yield. First, the pristine hBN powder was ground in a few drops of IPA for 2 h followed by the drying of gel like mixture under ambient conditions. After drying, the mixture was dispersed in IPA followed by ultrasonic bath sonication and probe sonication each for 1 h respectively. The as prepared dispersion was centrifuged at 4000 rpm for 30 min and top 3/4<sup>th</sup> portion of the dispersion was taken out for final solution. The milky white h-BN solution was mixed in equal volume ratio with MoS<sub>2</sub> QDs solution and stirred on a magnetic stirrer for 24 h. The whole process of synthesizing an all 2D nanocomposite from the exfoliated QDs of MoS<sub>2</sub> and few layer flakes of hBN is illustrated in Fig. 8 below.

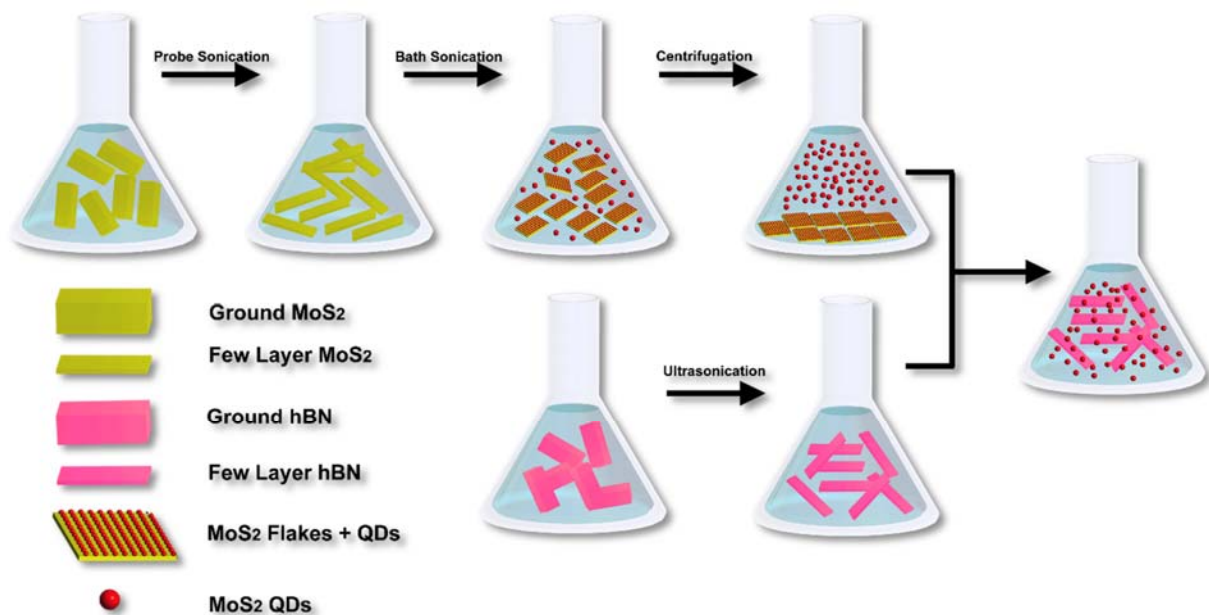


Figure 8. Schematic representation of the advanced 2D nanocomposite synthesis. The upper row illustrates the preparation of MoS<sub>2</sub> QDs while the bottom layer is showing the preparation of hBN flakes by using chemical liquid exfoliation in DMF, NMP, and DMEU respectively with appropriate color scheme and labelling of each step

## 2.2 Surface Characterizations

### 2.2.1 Surface Morphology

Fig. 9 shows the FESEM analysis of exfoliated WS<sub>2</sub> flakes and WS<sub>2</sub> thin film surface morphology. Fig. 9(a) showing the as exfoliated WS<sub>2</sub> flakes ranging from few microns to several nanometer proving the reliability of the liquid exfoliation with co-solvent and predicting the suitability to fabricate the thin film. Fig. 9(b) shows the FESEM image of as deposited thin film of exfoliated WS<sub>2</sub> flakes on PET substrate as it can be seen that there are some small and large flakes covering the maximum area of the PET substrate to make a uniform thin film. The uniform and continuous thin film of exfoliated WS<sub>2</sub> flakes with large lateral size makes it appropriate for microelectronic devices. Microstructure properties of as synthesized GQDs were analyzed by HR-TEM. Fig.9(c) presents the TEM image of exfoliated mono or few layer graphene nanosheets of several nanometer from which GQDs were extracted.



Fig. 9(d) shows the morphology of the platelike exfoliated hBN nanoflakes with a size of the individual flake ranging from 100 nm to several nanometers. Average lateral size of the exfoliated nanosheets is in the range of several hundreds of nanometer to a few micrometer with random orientation while each flake consist of mono or few layers of h-BN. These micron size h-BN 2D flakes are highly suitable for depositing thin films over a large substrate area. HR-TEM image in Fig. 9(e) shows the uniform size and high concentration of GQDs, inset histogram exhibits that diameter of the most of the GQDs lie in the range of 2-4 nm. The HR-TEM image of as synthesized MoS<sub>2</sub> QDs exhibiting their size and morphology is shown in Figure 9(f). It can be seen distinctly that the average size of the QDs is less than 10 nm with a high concentration of 7 mg/ml in the solution. The images taken from FESEM at a high resolution show extremely high density of sprayed MoS<sub>2</sub> flakes with no gaps in between them as shown in Fig. 9(g). These images show a chaotic array of MoS<sub>2</sub> flakes stacked mostly in plane. We attained very thin yet unbroken MoS<sub>2</sub> flakes film with conventional lateral dimensions. The prepared MoS<sub>2</sub> flakes were further critically characterized by taking images from TEM as shown in Fig. 9(h).

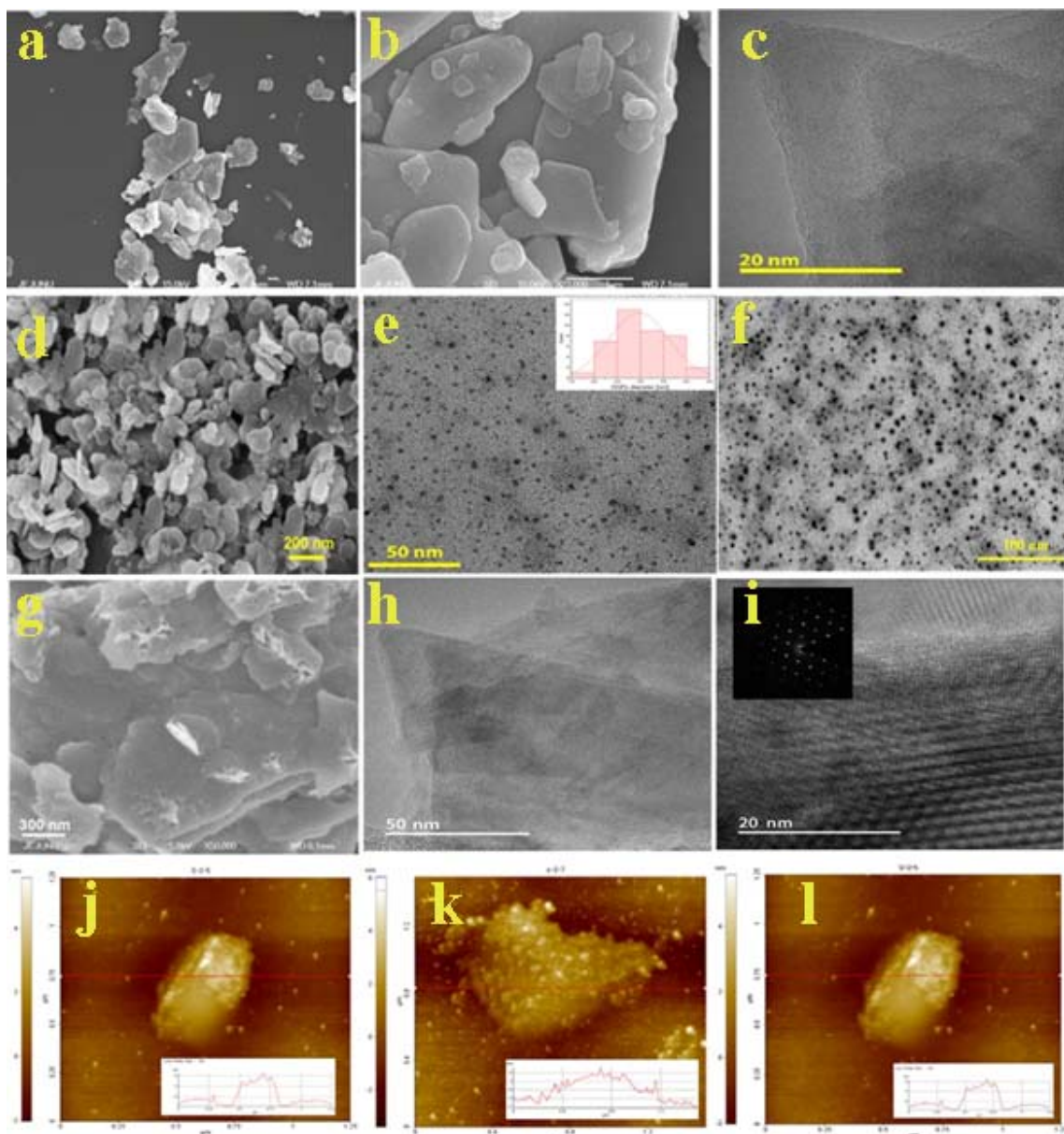


Figure 9. (a) FESEM image of as exfoliated WS<sub>2</sub> solution via liquid exfoliation with co-solvent (b) morphology of as deposited thin films of exfoliated WS<sub>2</sub> flakes through EHDA showing large lateral size up to few microns making it uniform and continuous. (c) HR-TEM image of exfoliated mono or few layer graphene nanosheets (d) Exfoliated hBN nanoflakes illustrating their platelike shape and size of the individual flake in the range of 100 nm-several nanometers (e) HR-TEM image displaying the uniform size and high concentration of GQDs, inset histogram exhibits the average size of as synthesized GQDs (2-4 nm) (f) HR-TEM image of as synthesized MoS<sub>2</sub> QDs (g) FESEM image illustrating the high density of as synthesized MoS<sub>2</sub> flakes (h) Typical bright field TEM image of MoS<sub>2</sub> flakes showing layer edges (i) Phase contrast High Resolution (HR) TEM image of thin MoS<sub>2</sub> flakes clearly displaying layer edges. Inset in (i) shows the selective area electron diffraction (SAED) pattern (j) AFM image illustrating a single flake of hBN surrounded by MoS<sub>2</sub> QDs. The thickness of a single hBN flake as displayed in this image is 4 nm verifying that it is a few layer flake (k) AFM image of formed 2D nanocomposite demonstrating the thickness of an individual hBN flake and interspersions of GQDs onto and around it. (l) AFM image of single exfoliated MoS<sub>2</sub> flake illustrating its few layered nature with average thickness of 4 nm

TEM images also verified the existence of a few layered exfoliated MoS<sub>2</sub> flakes with varying thickness. The regions with darker shade have more thickness owing to more number of layers as compared to regions with light color. Edges of individual layers stacked over one another can easily be observed near the periphery of MoS<sub>2</sub> flakes in high resolution (HR) TEM image of Fig. 9(i). HRTEM image is clearly exhibiting the layered structure of as synthesized MoS<sub>2</sub> flakes. The distance between two consecutive layers as seen from the Fig. 9(i) is evidently less than 1 nm. Inset of Fig. 9(i) displays the selective area electron diffraction (SAED) pattern that is consistent with a plain lattice showing that the prepared MoS<sub>2</sub> flakes are highly crystalline.

Furthermore, the morphology of all 2D nanocomposite composed of the exfoliated h-BN nanosheets and MoS<sub>2</sub>QDs was investigated by atomic force microscope (AFM) image as illustrated in Fig. 9(j). It can be seen along the red line and its corresponding height profile on the right side that thickness of the h-BN single nanosheet is ~ 4 nm and semiconducting MoS<sub>2</sub>QDs are interspersed onto and around the h-BN flakes which was the core objective of this study to form this nanocomposite for resistive switching application. Fig. 9(k) is the AFM image of 2D nanocomposite which demonstrates the thickness of an individual hBN flake and interspersion of GQDs onto and around the single flake of hBN. The image taken by AFM illustrates a few layered nature of exfoliated MoS<sub>2</sub> flakes as the average thickness is 3 nm which is equivalent to 3–4 layers as shown in Fig. 9(l). The surface morphology of as deposited MoS<sub>2</sub>-PVA nanocomposite thin film was further measured by 2D-Nanomapping as shown in Fig. 10. Values of average surface roughness (Ra) and Root mean square roughness (Rq) were 41.19 nm and 71.23 nm respectively.

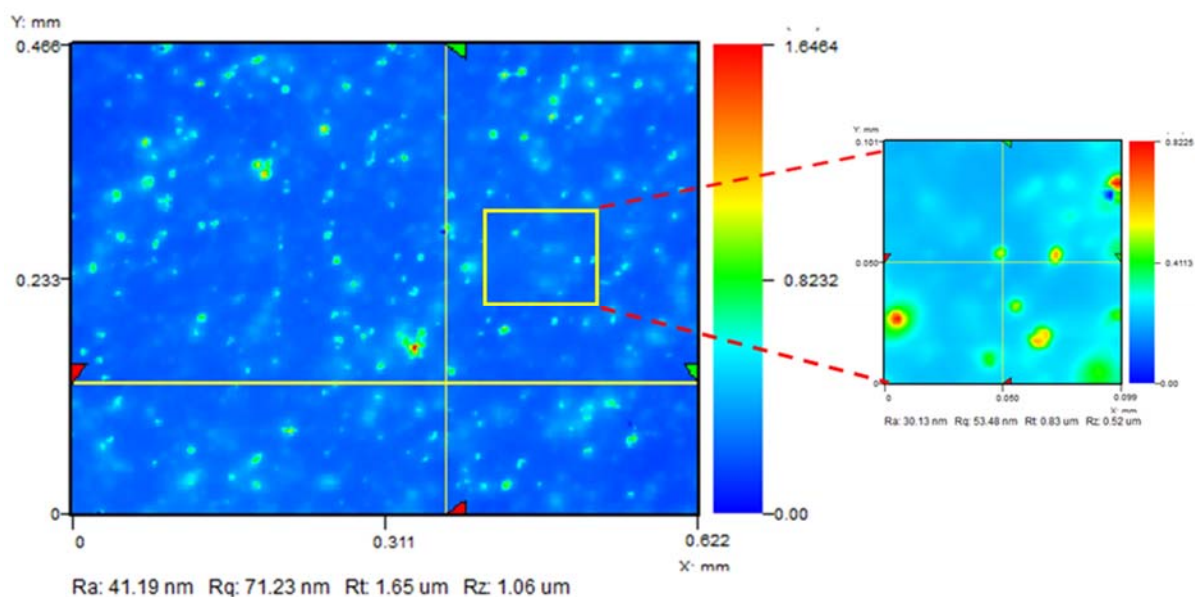


Figure 10. 2D nanomap image displaying the surface morphology of as deposited active thin film of MoS<sub>2</sub>-PVA nanocomposite by using EHD Atomization. The average roughness value is equal to 41.19 nm

### 2.2.2 Compositional Characterization

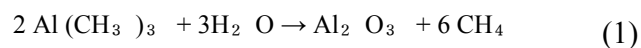
Raman spectroscopy was employed to characterize the structure of WS<sub>2</sub> as shown in Fig. 11(a). Two characteristic vibrations modes E<sub>2g</sub><sup>1</sup> and A<sub>1g</sub> can be observed in pristine and exfoliated WS<sub>2</sub> flakes, the E<sub>2g</sub><sup>1</sup> phonon mode involves the in-phase vibration of W atoms with respect to S atoms having also in-phase vibration but in opposite direction while the A<sub>1g</sub> mode is an out-of-plane vibration involving only the S atoms [63,64]. In pristine WS<sub>2</sub>, the two characteristic phonon modes (E<sub>2g</sub><sup>1</sup> and A<sub>1g</sub>) appeared at 353 cm<sup>-1</sup> and 419 cm<sup>-1</sup> respectively while after liquid exfoliation they were observed to be shifted up to 3 cm<sup>-1</sup> at 356 and 416 cm<sup>-1</sup>. The energy difference between the two vibrational modes of exfoliated WS<sub>2</sub> has been observed 60 cm<sup>-1</sup>, is the fingerprint for the well exfoliation up to few layers. There is red shift for A<sub>1g</sub> mode in exfoliated WS<sub>2</sub> because van der Waals forces decrease between the layers as the number of layers are decreased which results weakening the restoring forces in the vibration, however, blue shift was observed in E<sub>2g</sub><sup>1</sup> mode.

Other TMDs also show such trend due to the reduced long-range Coulomb interaction between the effective charges. These effective charges may be caused by the dielectric screening or stacking-induced changes in the intra-layer bonding [65,66].

X-ray diffraction analysis of pristine WS<sub>2</sub> and as deposited exfoliated WS<sub>2</sub> thin film has been shown in Fig. 11(b). A prominent peak corresponds to (002) plane while the other three small peaks are attributed to (100), (105) and (112) planes, these all peaks showing the hexagonal 2H-WS<sub>2</sub> phase with no discernible impurity. Raman spectroscopy was used to confirm the transition of pristine hBN powder from bulk to exfoliated flakes as illustrated in Fig. 11(c). The E<sub>2g</sub> vibrational mode is observed in pristine and exfoliated h-BN which is the Raman imprint of h-BN structure. The E<sub>2g</sub> mode is observed at 1367 cm<sup>-1</sup> in bulk hBN while a typical slight shift in this peak to 1370 cm<sup>-1</sup> is observed for exfoliated h-BN. There is a blue shift of the E<sub>2g</sub> vibrational mode up to 3 cm<sup>-1</sup> in exfoliated h-BN which has quite resemblance with the earlier reported results [67,68].

Fig. 11 (d) presents the Raman spectra of exfoliated hBN nanoflakes in which typical E<sub>2g</sub> mode peak of hBN is appeared at 1370.5 cm<sup>-1</sup> [60] indicating the good crystallinity and exfoliation while in pristine hBN the same peak appears at 1367 cm<sup>-1</sup>. Raman spectroscopy analysis was carried out to conform the conversion of few layer formation from pristine MoS<sub>2</sub> flakes. It is a very useful technique for quantitatively measuring the number of layers present in exfoliated MoS<sub>2</sub> flakes. Raman spectroscopy utilize inflexible scattering of homochromatic light from a laser. The energy of the photons shifts upward or downward depending upon the laser interacting with vibrations in the system. Low power laser is desirable in order to protect sample from disintegration. Raman spectroscopy was necessary for ensuring the existence of MoS<sub>2</sub> flakes in the prepared solution. Figure 11(e) illustrates the Raman spectra of exfoliated MoS<sub>2</sub> and signifies the presence of its few

layered flakes. Raman spectra was plotted in the range of  $300\text{ cm}^{-1}$  to  $500\text{ cm}^{-1}$ . The characteristic peaks of a few layered  $\text{MoS}_2$  representing  $\text{E}_{2g}$  1 and  $\text{A}_{1g}$  were found at  $378\text{ cm}^{-1}$  and  $405\text{ cm}^{-1}$  respectively which is in agreement with already reported literature<sup>29</sup>. Peak of  $\text{E}_{2g}$  1 is due to in plane vibrations between two sulfur (S) and a single molybdenum (Mo) atoms in the basal plane whereas peak of  $\text{A}_{1g}$  is due to out of plane vibrations of only S atoms along c axis relative to each other. These two peaks undisputedly suggest that the structure of prepared  $\text{MoS}_2$  flakes is 2H30. Fig. 11(f) shows the X-ray photoelectron spectroscopy (XPS) results of encapsulating thin film ( $\text{Al}_2\text{O}_3$ ) with all its characteristic peaks visible in the spectrum. The XPS graph of  $\text{Al}_2\text{O}_3$  exhibits Aluminum (Al), Carbon (C), and Oxygen (O) content. The Al 2p, Al 2s, C 1s and O 1s characteristic peaks are present at binding energies of 74 eV, 119 eV, 285 eV and 531 eV respectively as illustrated in Fig. 11(f). The Al 2p, Al 2s and O 1s peaks are the most important peaks as they verify development of  $\text{Al}_2\text{O}_3$  thin film. Already reported results proposed the energy separation between Al 2p peaks and O 1s peaks must be equal to 457 eV [69]. These results are well supported by our current study as the energy gap between these two respective peaks [Al 2p (119 eV) and O 1s (531 eV)] is 457 eV. The peak of C 1s is also visible in the given XPS spectrum at a binding energy of 285 eV which signifies the carbon content in the deposited encapsulation thin film due to its exposure to air. Even a small exposure of sample to atmosphere can incorporate adventitious carbon on the surface of developed  $\text{Al}_2\text{O}_3$  thin films. These results clearly shows that no other elements were detected in the encapsulation layer implying that the formed thin film of  $\text{Al}_2\text{O}_3$  was free of impurities. All characterizations presented in Fig. 11 were performed at ambient conditions. The overall reaction for the formation of encapsulation  $\text{Al}_2\text{O}_3$  thin film through SAALD can be represented as:



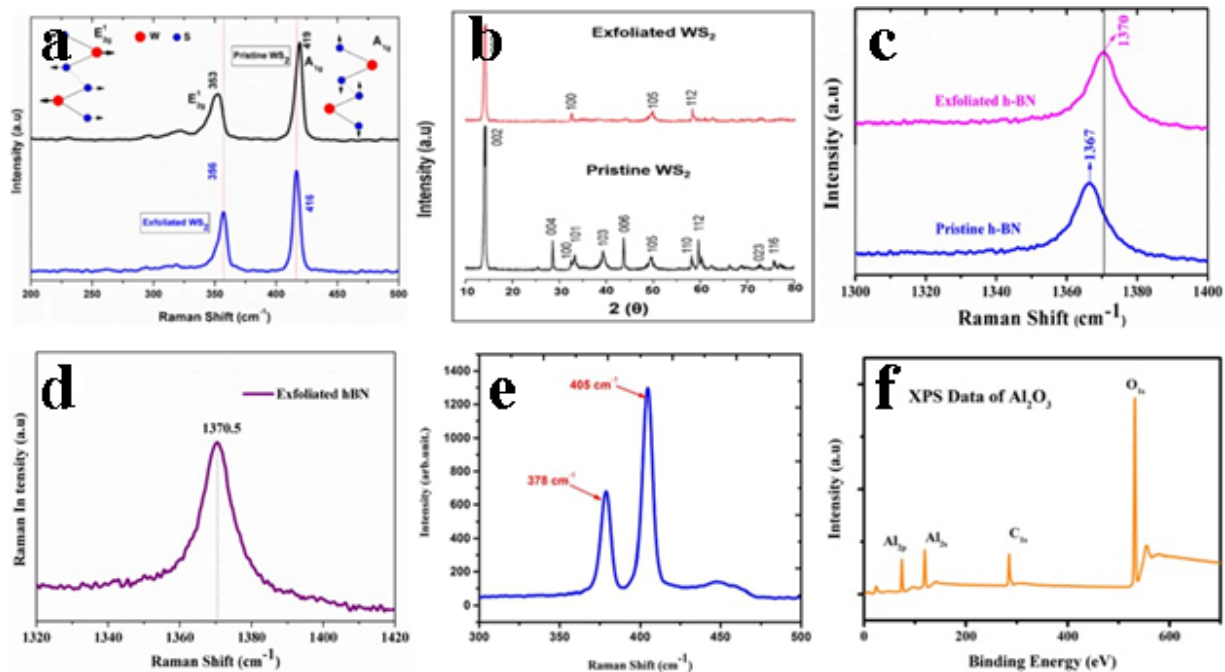


Figure 11. (a) Raman spectra of as deposited thin film of WS<sub>2</sub> flakes (b) XRD results of pristine and exfoliated WS<sub>2</sub> flakes (c) Raman spectra of pristine and exfoliated hBN flakes illustrating a clear shift in the peak (d) Raman spectra of exfoliated hBN nanoflakes (e) Typical Raman spectra of a few layered MoS<sub>2</sub> semiconductor (f) XPS data of as deposited Al<sub>2</sub>O<sub>3</sub> thin film for encapsulation of our memory device

### 2.2.3 Optical Characterization

Fig. 12(a) shows the transmittance and absorbance spectra of as deposited thin film of exfoliated WS<sub>2</sub> flakes recorded by spectra UV/vis spectroscopy. The high transmittance and low absorbance predicting the potential applications of WS<sub>2</sub> thin film in optoelectronic devices. The optical properties of the hBN/MoS<sub>2</sub> QDs nanocomposite were evaluated by UV/Vis spectroscopy as shown in Figure 12(b). High transmittance of ~ 84% and low absorbance spectra were obtained owing to the small thickness of exfoliated h-BN nanosheets that shows that this promising 2D nanocomposite can be used for various optical electronic devices such as photo sensors, LEDs and solar cells. Optical properties of exfoliated hBN nanoflakes and its nanocomposite with GQDs have been analyzed through UV/Vis spectroscopy. Transmittance and absorbance spectra of as

deposited GQDs/hBN nanocomposite thin film are shown in Fig. 13(c) which denotes its high transmittance of  $\sim 89\%$  and low absorbance, making it a suitable choice for transparent electronic devices.

In order to determine the optical properties of as synthesized MoS<sub>2</sub> flakes, wavelength dependent transmittance characterization was carried out by UV/Vis spectroscopy in the range of 300–800 nm as shown in Fig. 12(d). An optical transmittance of  $\approx 80\%$  was observed in the as synthesized MoS<sub>2</sub> flakes. The absorbance curve is also shown along with the transmittance curve for better understanding. This further conforms the presence of a few layered MoS<sub>2</sub> structure because transmittance value of a monolayer MoS<sub>2</sub> flake is much higher (nearly 95%) [70]. Total number of layers and the transmittance of MoS<sub>2</sub> flakes is inversely proportional to each other. The transmittance remained nearly constant from 400 nm to 770 nm and began to decrease after 770 nm. Visible light is absorbed and reflected several times in a few layered structure. UV/Vis spectroscopy further endorse the presence of a few layered MoS<sub>2</sub> flakes because for monolayer MoS<sub>2</sub> nanosheets this broad peak appears at nearly 652 nm. The difference in the peak value is due to direct and indirect bandgap in monolayer and a few layer MoS<sub>2</sub> flakes respectively. This might be due to quantum confinement effect across the 2D planes [71].



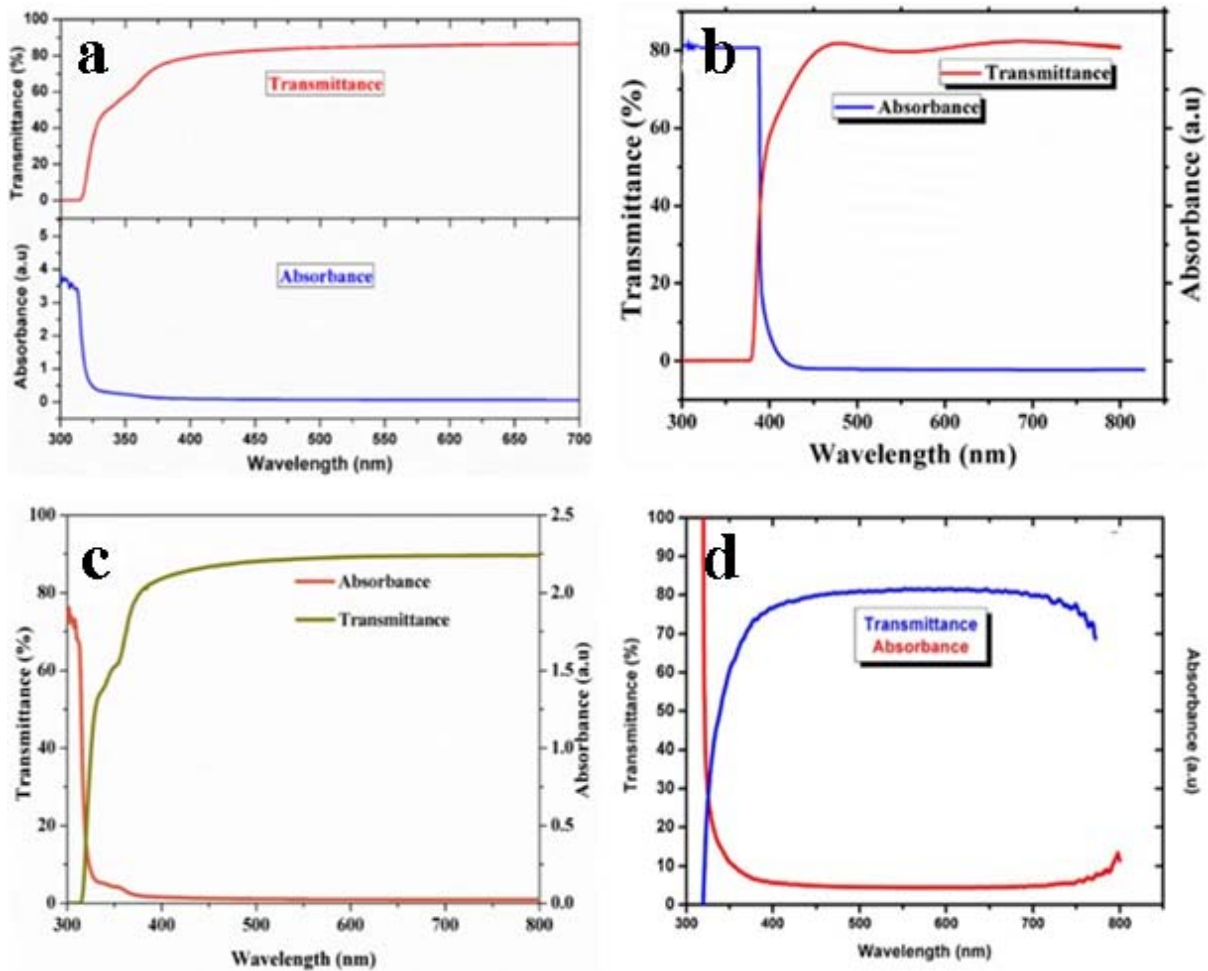


Figure 12. (a) Optical absorption and transmittance of as deposited thin film of WS<sub>2</sub> flakes (b) Illustration of optical transmittance and absorbance of 2D nanocomposite thin film. (c) Transmittance and absorbance spectra of as deposited thin film of GQDs/hBN nanocomposite (d) UV-vis optical transmittance spectra of the as synthesized few layered MoS<sub>2</sub> flakes

## 2.2 Fabrication of flexible RRAM devices

### 2.2.1 Fabrication of Ag/WS<sub>2</sub>/Ag RRAM

Entire device was fabricated on a flexible and transparent PET substrate through all-printed technology such as reverse offset, EHD atomization, and EHD patterning for patterning bottom electrodes (Ag), spraying thin film of functional material (WS<sub>2</sub> flakes) and patterning top electrode (Ag) respectively. Reverse offset printing was preferred over other micro-patterning techniques such as screen printing, gravure printing and inkjet printing due to its high resolution, control and

uniformity of as patterned electrodes. An array of nineteen bottom Ag electrodes was printed on a flexible PET substrate followed by sintering at 100 °C for 2 h. The as patterned Ag bottom electrodes through reverse offset printing were highly conductive ( $0.2 \Omega\text{cm}^{-1}$ ).

Moreover, state of the art printing technique of EHD atomization is a well-known method to achieve uniform and extremely thin films of soluble layered materials on the surface of patterned PET substrate [3,72]. Functional thin film of WS<sub>2</sub> ink was sprayed through EHD atomization and various critical parameters were optimized to achieve a stable spray of deposition. The optimized parameters are listed in table 1 and table 2 respectively for reproducibility of this work. Deposited thin film of WS<sub>2</sub> solution through EHD atomization was sintered at 120 °C for 2 h to evaporate the solvent completely. Finally, the top Ag electrode was patterned on the surface of WS<sub>2</sub> thin film to complete the  $19 \times 1$  array of memory cells. EHD patterning was preferred over other printing techniques to avoid damaging the functional thin film as it is a non-contact method of patterning electrodes that does not touch the thin film surface. The width of the top electrode was 30  $\mu\text{m}$  as measured through the optical microscope. Top Ag electrode was sintered at 100 °C for 2h. The flow diagram of entire device fabrication is illustrated in Fig. 2 with labelling of each part.

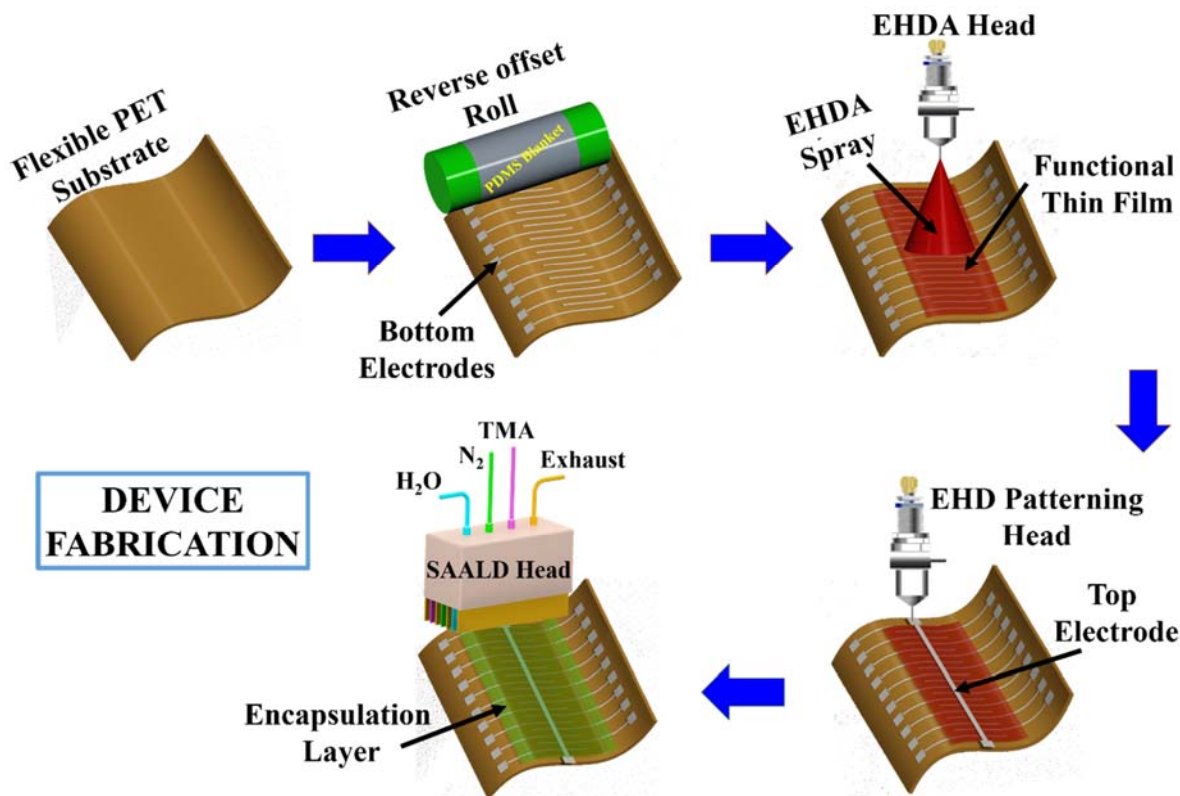


Figure 13. Schematic diagram of entire device fabrication through all printed technology followed by encapsulation of atomically thin film of  $\text{Al}_2\text{O}_3$  to enhance its lifetime

The optimized parameters for spraying  $\text{WS}_2$  thin film through EHDA, different spraying modes of  $\text{WS}_2$  through EHDA and optimized conditions for patterning Ag electrodes are listed in Table 1, Table 2 and Table 3 respectively.

Table 1. Optimized values spraying parameters to precisely control the film uniformity and thickness through EHD Atomization of  $\text{WS}_2$  solution

| Parameter                    | Optimized Value   |
|------------------------------|-------------------|
| Flow Rate                    | 110 ul/h          |
| Applied Voltage              | 2.7 kV            |
| Nozzle to substrate distance | 10 mm             |
| Stage Speed                  | 6 mm/s            |
| Nozzle Diameter              | 200 $\mu\text{m}$ |
| Total No of Spraying Passes  | 3                 |

Table 2. Different spraying modes and their respective voltage range in which they appeared during EHD atomization of WS<sub>2</sub> solution

| <b>Mode of Deposition</b> | <b>Voltage Range</b> |
|---------------------------|----------------------|
| Dripping                  | 0- 4.2 kV            |
| Micro Dripping            | 4.2-5.1 kV           |
| Unstable Cone-Jet         | 5.1-5.9 kV           |
| Stable Cone-Jet           | 5.9-6.3 kV           |
| Multi-stable Cone-Jet     | > 6.3 kV             |

Table 3. Optimized parameters and their fixed values used for patterning the top Ag electrode through EHD patterning

| <b>Parameter</b>             | <b>Optimized Value</b> |
|------------------------------|------------------------|
| Nozzle to Substrate Distance | 5 $\mu$ m              |
| External Nozzle Diameter     | 30 $\mu$ m             |
| Nozzle Speed                 | 0.3 mm/s               |
| Applied Pressure             | 64.6 kPa               |

In order to increase the reproducibility of obtained results and enhance the lifetime of proposed memory device, we further encapsulated our device with Al<sub>2</sub>O<sub>3</sub> thin film deposited through SAALD system to protect its surface from ambient environment. Al<sub>2</sub>O<sub>3</sub> is a non-reactive material that does not change the chemical properties of functional material. Nitrogen (N<sub>2</sub>) gas was used for dual purposes of an inert separator and as a carrier gas while TMA and H<sub>2</sub>O were used as precursors to form atomically thin film of Al<sub>2</sub>O<sub>3</sub> through chemical reaction. All the optimized parameters for depositing encapsulation layer on the surface of our device are listed in Table 4 below. The effectiveness of this encapsulation layer to elongate the performance of a memory device has already been verified in our previous work with detail [54].

Table 4. Optimized parameters for depositing atomically thin film of Al<sub>2</sub>O<sub>3</sub> through ALD along with complete details of used precursors such as TMA and H<sub>2</sub>O.

| Exhaust Setting<br>(torr) | Substrate | MFC Settings<br>(sccm) |      | Temperature<br>(Celsius) |     | Stage Motion<br>Speed<br>(mms <sup>-1</sup> ) | Distance<br>between<br>Stage & Head<br>(mm) | No. of<br>Passes | Time<br>Taken<br>(min) |
|---------------------------|-----------|------------------------|------|--------------------------|-----|---|---|------------------|------------------------|
|                           |           |                        |      |                          |     |   |   |                  |                        |
| 0.73                      | PET       | TMA                    | 100  | TMA                      | 100 | 6   | 0.5   | 5                | 2.5                    |
|                           |           |                        |      | H <sub>2</sub> O         | 100 |   |   |                  |                        |
|                           |           | H <sub>2</sub> O       | 130  | N <sub>2</sub>           | 0   |   |   |                  |                        |
|                           |           |                        |      | HEAD                     | 100 |   |   |                  |                        |
|                           |           | N <sub>2</sub>         | 1200 | STAGE                    | 90  |   |   |                  |                        |
|                           |           |                        |      | H <sub>2</sub> O         | 100 |   |   |                  |                        |
|                           |           | H <sub>2</sub> O       | 130  | N <sub>2</sub>           | 0   |   |   |                  |                        |
|                           |           |                        |      | HEAD                     | 100 |   |   |                  |                        |
|                           |           | N <sub>2</sub>         | 1200 | STAGE                    | 90  |   |   |                  |                        |

### 2.2.2 Fabrication of Ag/hBN-GQDs/Ag RRAM

Typically a NVM device based on resistive switching is fabricated in the form of a sandwich or a crossbar structure owing to its advantages of enhanced scalability and multiple stackability, however, sandwich structure causes current leakage and cross talk between nearby memory cells leading to read operation error. Various solutions have been proposed to solve the problem of sneak current such as integrating different circuit elements to NVM device. However, integration of several circuit elements such as resistors, transistors, and diodes in series with the memory device make the circuitry and device fabrication extremely complex [73,74]. Moreover, in a sandwich type structure, extremely high control is required during patterning top electrode to avoid short circuit with the bottom electrode as it might damage the functional layer [43]. In order to overcome these complications of cross talk between adjacent memory cells, short circuit among

electrodes and device complexity we have proposed a planar structure for our NVM memory device. Our device has only two fabrication steps including side by side electrode deposition followed by active layer spray thus offering an even simpler and cost effective fabrication process. The flexible memory device was fabricated by using printing technology due to its ease of processing and high compatibility with electronic devices [3,46,60]. Bottom electrodes were patterned by reverse offset whose details have been presented under the heading of fabrication technologies in the introduction section. Optical images of as patterned electrodes are also added that clearly exhibit the high quality of obtained metallic electrodes as presented in Fig. 14.

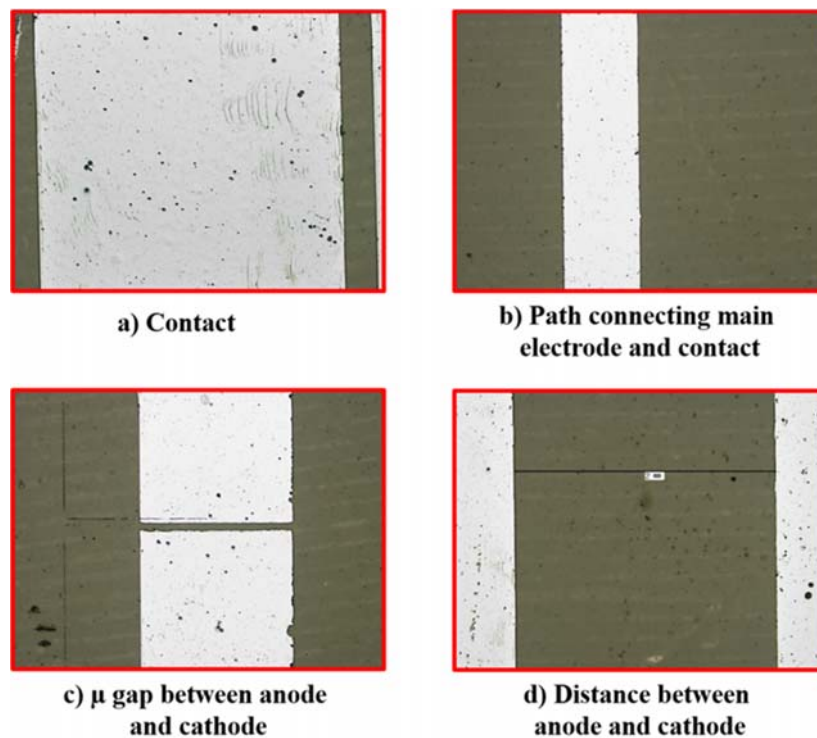


Figure 14. Optical microscope images of as patterned Ag electrodes on flexible PET substrate illustrating their high uniformity and smooth surface

All the electrodes were highly conductive with resistivity of 0.2 ohm-cm after being sintered for 1 h at 110 °C. Functional thin film of GQDs-hBN nanocomposite was successfully sprayed on top of Ag electrodes by using highly reliable and non-contact EHDA printing system. EHDA was

selected due to its ability to form extremely uniform and thin films of various nanocomposite materials in quick time with high control and simplicity [3,46,60,75]. The GQDs-hBN nanocomposite solution was passed through the spraying nozzle by applying high power electric field from the external voltage supply. Various modes of deposition were achieved from dripping mode to multi-stable jet mode by steadily increasing the applied voltage while the uniform thin film was deposited completely in stable cone-jet mode. All values of applied external voltage and their respective spraying modes are listed in Table 5 while complete schematic diagram with proper labelling of each part and the operating envelope for spraying GQDs-hBN ink through EHDA are shown in Fig. 15.

Table 5. Various modes of deposition along with the range of applied voltage difference from high- voltage power supply during EHDA of hBN/GQDs nanocomposite

| <b>Mode of Deposition</b> | <b>Voltage Range (kV)</b> |
|---------------------------|---------------------------|
| Dripping                  | 0- 3.8                    |
| Micro Dripping            | 3.8-5.1                   |
| Unstable Cone-Jet         | 5.1-5.5                   |
| Stable Cone-Jet           | 5.5-6.2                   |
| Multi-stable Cone-Jet     | > 6.2                     |

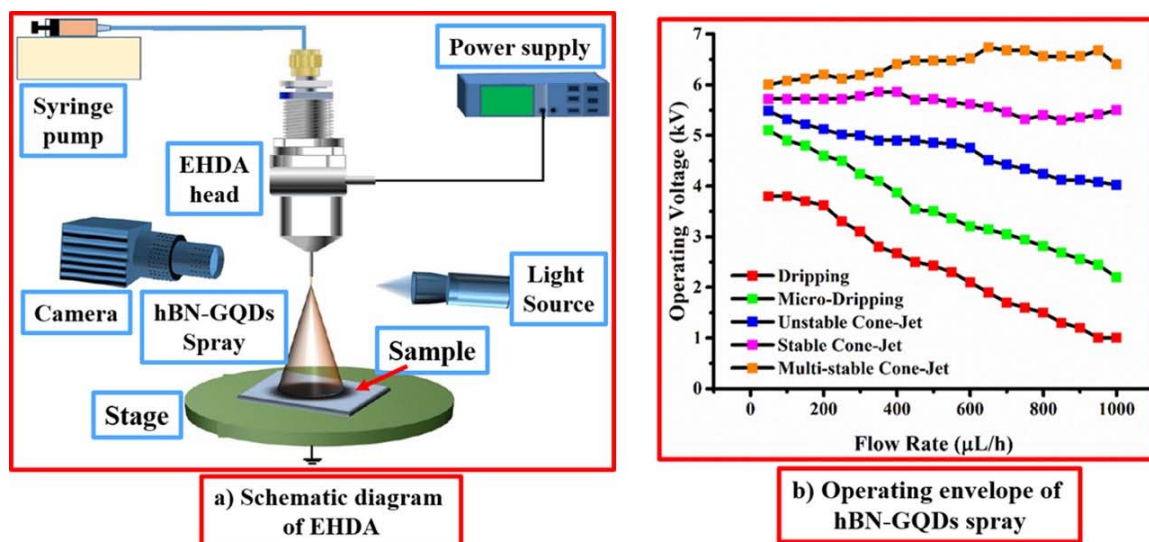


Figure 15. a) Schematic diagram of Electrohydrodynamic (EHD) Atomization system for spraying GQDs-hBN thin film over the patterned silver (Ag) electrodes with labeling of each part b) Operating envelope of GQDs-hBN spray through EHDA illustrating the voltage range for each mode of deposition

Various parameters of EHDA printing process such as flow rate of nanocomposite ink, nozzle diameter, standoff distance, speed of stage and magnitude of applied voltage are to be optimized to achieve uniform thin film. All the optimized parameters for spraying GQDs-hBN nanocomposite solution are listed in Table 6. Deposited thin film of GQDs-hBN nanocomposite was sintered for 2 h at 120 °C.

Table 6. Optimized values of various parameters for spraying functional thin film of GQDs-hBN 2D nanocomposite to control the film thickness and uniformity during EHDA

| Parameter         | Optimized Value |
|-------------------|-----------------|
| Flow Rate         | 280 ul/h        |
| Applied Voltage   | 5.6 kV          |
| Standoff distance | 22 mm           |
| Stage Speed       | 4.5 mm/s        |
| Nozzle Diameter   | 300 μm          |



The top electrode protects the functional thin film of a memory device in a typical sandwich type structure however, in the case of a planar device structure there is no top electrode therefore, functional layer should be protected by some other means from humid environment. We encapsulated our device with an atomically thin layer of Al<sub>2</sub>O<sub>3</sub> deposited through spatial ALD system in order to protect GQDs-hBN functional thin film from open environment and to enhance its lifetime. Water and TMA were used as precursors, while nitrogen (N<sub>2</sub>) acted as a carrier gas and as an inert separator. Details of all the optimized parameters during device encapsulation are listed in Table 7.

Table 7. Optimized parameters for depositing atomically thin film of Al<sub>2</sub>O<sub>3</sub> through ALD along with complete details of used precursors such as TMA and H<sub>2</sub>O.

| Exhaust Setting (torr) | Substrate | MFC Settings (sccm) |      | Temperature (Celsius) |     | Stage Motion Speed (mms <sup>-1</sup> ) | Distance between Stage & Head (mm) | No. of Passes | Time Taken (min) |
|------------------------|-----------|---------------------|------|-----------------------|-----|---|------------------------------------|---------------|------------------|
|                        |           |                     |      |                       |     |   |                                    |               |                  |
| 0.73                   | PET       | TMA                 | 100  | TMA                   | 100 | 6                                       | 0.5                                | 5             | 2.5              |
|                        |           |                     |      | H <sub>2</sub> O      | 100 |   |                                    |               |                  |
|                        |           | H <sub>2</sub> O    | 130  | N <sub>2</sub>        | 0   |   |                                    |               |                  |
|                        |           |                     |      | HEAD                  | 100 |   |                                    |               |                  |
|                        |           | N <sub>2</sub>      | 1200 | STAGE                 | 90  |   |                                    |               |                  |
|                        |           |                     |      | H <sub>2</sub> O      | 100 |   |                                    |               |                  |
|                        |           | H <sub>2</sub> O    | 130  | N <sub>2</sub>        | 0   |   |                                    |               |                  |
|                        |           |                     |      | HEAD                  | 100 |   |                                    |               |                  |
|                        |           | N <sub>2</sub>      | 1200 | STAGE                 | 90  |   |                                    |               |                  |

The encapsulation layer does not alter the device performance in terms of switching ratio or endurance. This is already proved in our previous study that encapsulating a memory device by atomically thin layer of Al<sub>2</sub>O<sub>3</sub> restricts the decomposition and deterioration of the functional layer by blocking its pinholes that otherwise might allow oxygen and water vapors to penetrate through them resulting in the degradation of whole device [54]. The flow diagram of whole device fabrication with its optical image in the center is illustrated in Fig. 16.

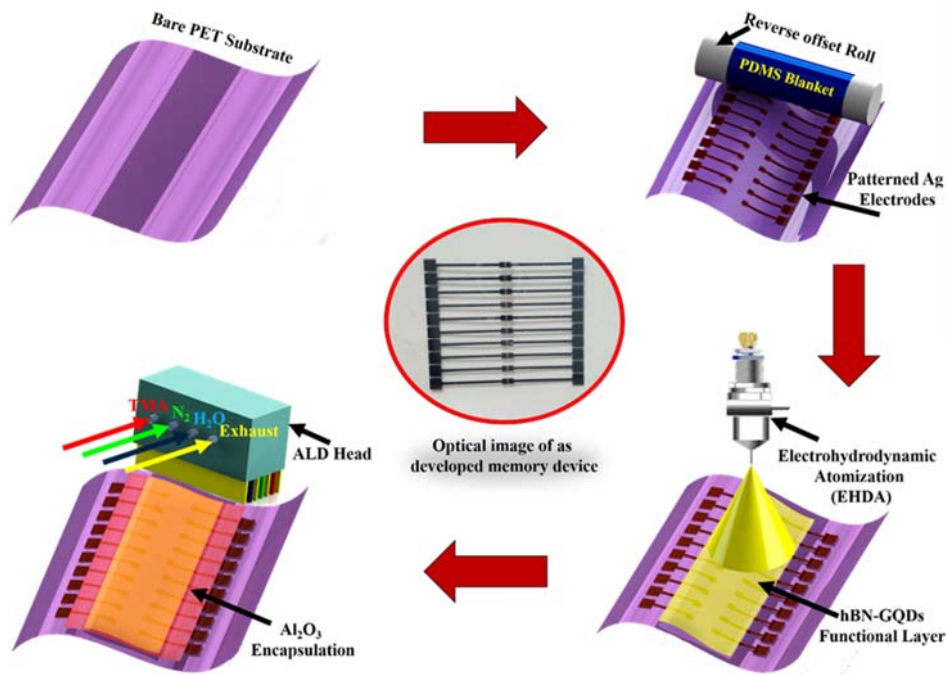


Figure 16. Flow diagram of flexible NVM device fabrication illustrating each step sequentially such as bare PET substrate, patterning of Ag electrodes with high resolution through reverse offset printing system, spraying functional thin film of QDs-hBN nanocomposite through EHDA and finally encapsulating the whole device by atomically thin layer of  $\text{Al}_2\text{O}_3$  deposited through spatial ALD system. Optical image of the final device is shown in the center of the diagram.

### 2.2.3 Fabrication of ITO/hBN-MoS<sub>2</sub>QDs/Ag RRAM

All 2D functional thin film of hBN-MoS<sub>2</sub> QDs nanocomposite was successfully deposited by using an in-house built EHDA system. EHDA is a non-vacuum and non-contact based printing technique that has been used in printed electronics for spraying thin films of various materials [57,58,60,75–78]. Prior to deposition of the thin film, flexible PET substrate was treated with acetone, ethanol, and deionized water to remove any impurities followed by UV treatment to improve surface adhesion of thin film. The operating envelope of hBN-MoS<sub>2</sub>QDs thin film deposition is shown in Fig. 17. The controlling parameters of EHDA printing technique include standoff distance, ink flow rate, applied voltage and nozzle diameter. The flow rate during hBN-MoS<sub>2</sub>QDs solution deposition was varied to achieve the stable cone jet for uniform deposition. Specific values of all

optimized parameters and voltage ranges to achieve different deposition modes are listed in Table 8 and Table 9 respectively. After deposition, hBN-MoS<sub>2</sub>QDs nanocomposite thin film was sintered at 120 °C for 2 h in a furnace to evaporate its solvent completely.

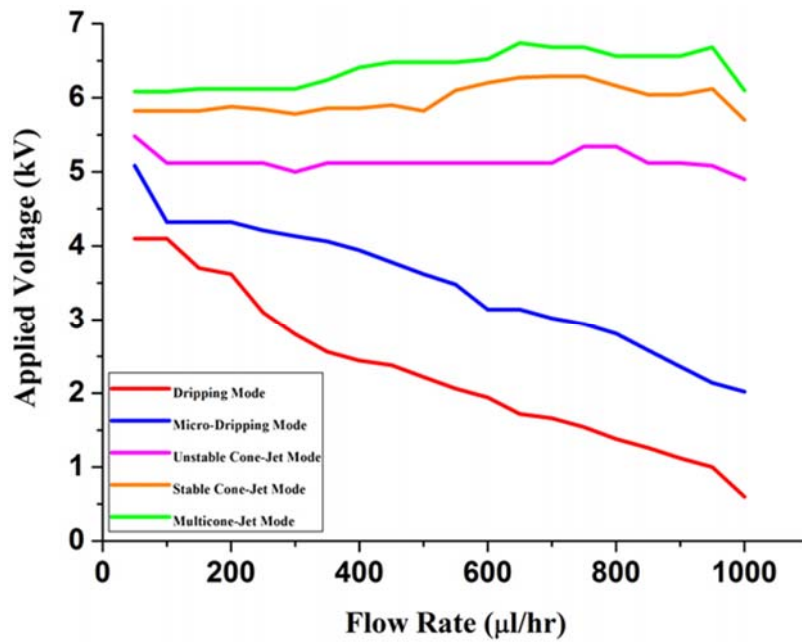


Figure 17. Operating envelope for the deposition of all 2D functional layer of the fabricated device based on the hBN/MoS<sub>2</sub>QDs nanocomposite. This plot illustrates different ranges of applied voltage and their respective flow rates

Table 8. Optimized values of various parameters to control the film thickness and uniformity during EHD Atomization of hBN/MoS<sub>2</sub>QDs nanocomposite

| Parameter         | Optimized Value |
|-------------------|-----------------|
| Flow Rate         | 300 ul/h        |
| Applied Voltage   | 4.7 kV          |
| Standoff distance | 20 mm           |
| Stage Speed       | 3 mm/s          |
| Nozzle Diameter   | 310 µm          |

Table 9. Various modes of deposition along with the range of applied voltage difference from high- voltage power Ssupply during EHDA of hBN/MoS<sub>2</sub>QDs nanocomposite

| <b>Mode of Deposition</b> | <b>Voltage Range</b> |
|---------------------------|----------------------|
| Dripping                  | 0- 3.6 kV            |
| Micro Dripping            | 3.6-4.2 kV           |
| Unstable Cone-Jet         | 4.2-5.1 kV           |
| Stable Cone-Jet           | 5.1-5.7 kV           |
| Multi-stable Cone-Jet     | > 5.7 kV             |

Top circular electrodes with three different diameters of 42  $\mu\text{m}$ , 70  $\mu\text{m}$  and 100  $\mu\text{m}$  respectively were printed on the surface of hBN-MoS<sub>2</sub>QDs functional layer through a non-contact printing technique of RPC inkjet printing system to complete device fabrication. The whole schematic diagram of RPC inkjet printing system during each patterning step is presented in Fig. 2. RPC inkjet printing system was preferred over other patterning techniques owing to its high controllability, compatibility with flexible substrates and high precision without damaging the functional layer. Unlike continuous drop on demand (DOD) method,  $\mu$ -droplets from RPC inkjet printing system were only generated when they were required. The capillary force keeps the high viscosity Ag nanoparticle ink inside the chamber while a pneumatic actuator was used to dispense the droplets. Optimized values of various parameters for highly controllable, precise and repeatable patterning of  $\mu$ -droplets are presented in Table 10. These  $\mu$ -droplets were sintered by UV laser in real time followed by thermal sintering at 110 °C for 1 h to enhance conductivity. The schematic diagram of final RRAM device based on hBN-MoS<sub>2</sub>QDs functional thin film along with the chemical structure of used 2D materials are illustrated in Fig.18.

Table 10. Optimized condition and their set values during the deposition of top Ag electrode through RPC inkjet printing system patterning process of top Ag Electrode

| Parameter                 | Optimized Value   |
|---------------------------|-------------------|
| Diameter of needle holder | 1 mm              |
| Standoff distance         | 100 $\mu\text{m}$ |
| Needle Speed              | 0.05-0.02 mm/s    |
| Pneumatic Pressure        | 0.2 kPa           |
| UV laser                  | 365-395 nm        |

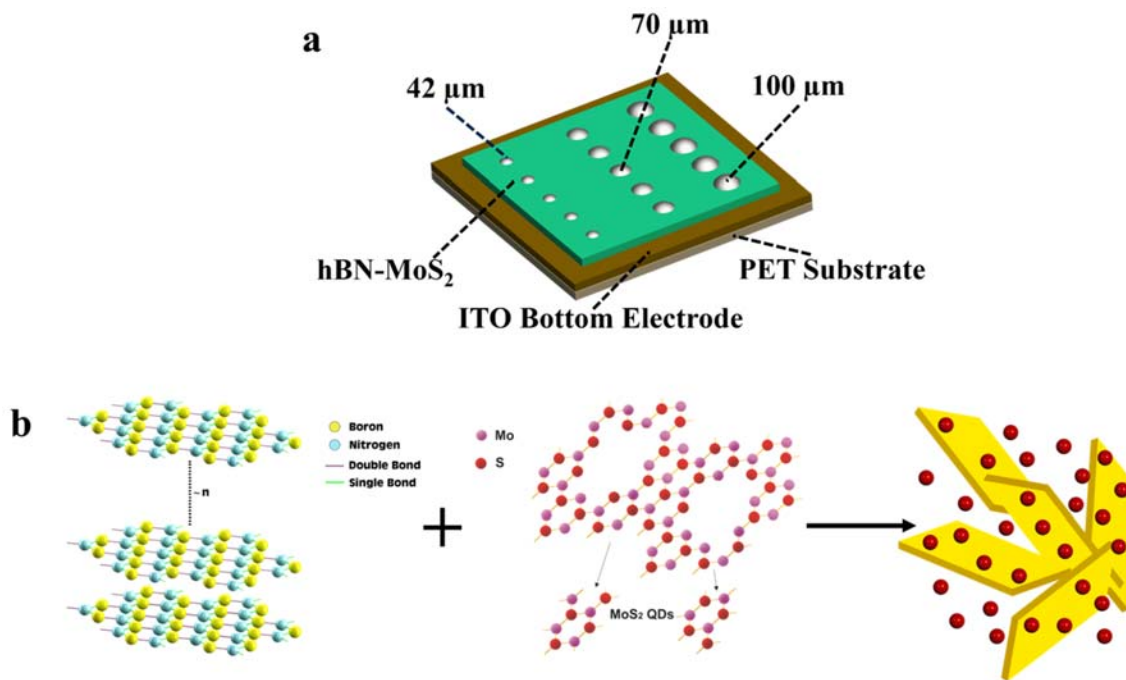


Figure 18. (a) 3D schematic diagram of as fabricated nonvolatile memory device on a flexible PET substrate with three different top electrode sizes (b) Chemical structures of the 2D materials used as the functional layer of fabricated device.

#### 2.2.4 Fabrication of Ag/MoS<sub>2</sub>-PVA/Ag RRAM

To realize highly conductive electrodes, reverse offset printing was used to pattern bottom Ag electrodes. Electrodes printed by reverse offset roll-to-plate printing technique have the promising characteristics of high resolution, low resistivity, high quality surface, simplicity, and ease of fabrication to realize an accurate and precise pattern [56]. It is a direct printing method that can

print electrodes with pattern size  $< 1 \text{ }\mu\text{m}$  unlike its other competitive direct printing techniques such as screen printing, flexographic printing, gravure printing and inkjet printing. A detailed explanation of reverse offset patterning process is shown in Fig. 1.

Thin film of MoS<sub>2</sub>-PVA nanocomposite was successfully deposited by using an in-house built EHDA system. EHDA was preferred due to its high control, simplicity and ability to produce very thin films with high uniformity in quick time. Complete schematic diagram of EHDA system with labelling of each part is shown in Supplementary Fig. 3. The MoS<sub>2</sub>-PVA nanocomposite solution was allowed to flow through the meniscus of the nozzle by applying the electric field as shown in the schematic diagram of Fig. 20. The flow rate was varied from 20 ul/hr–1000 ul/hr in order to achieve the stable cone jet for deposition of uniform thin film in desired area of target substrate. Hybrid MoS<sub>2</sub>-PVA nanocomposite ink being sprayed began to split into small droplets with increasing voltage. Spraying modes varied from dripping to multi-stable jet after passing through micro-dripping, unstable jet and stable jet. The spraying mode was controlled by the parameters of applied voltage, distance of nozzle from the substrate, nozzle diameter and set value of flow rate. The operating envelope of depositing MoS<sub>2</sub>-PVA nanocomposite through EHDA is shown in Fig. 3. Film thickness was controlled by optimizing the number of spraying passes, spraying time, speed of stage and standoff distance between the nozzle and desired substrate. The values of all optimized parameters are listed in Supplementary Table 11 while the voltage range for achieving different modes of deposition are listed in Supplementary Table 12. Deposited thin film of MoS<sub>2</sub>-PVA nanocomposite was sintered at 120 °C for 2 hours in a furnace to evaporate its solvent completely.

Table 11. Optimized values of various parameters to control the film thickness and uniformity during EHD Atomization of MoS<sub>2</sub>-PVA nanocomposite

| <b>Parameter</b>             | <b>Optimized Value</b> |
|------------------------------|------------------------|
| Flow Rate                    | 100 ul/h               |
| Applied Voltage              | 2.9 kV                 |
| Nozzle to substrate distance | 10 mm                  |
| Stage Speed                  | 6 mm/s                 |
| Nozzle Diameter              | 200 um                 |
| Total No of Spraying Passes  | 6                      |

Table 12. Various Modes of Deposition along with the Range of Applied Voltage Difference from High- Voltage Power Supply during EHD Atomization of MoS<sub>2</sub>-PVA nanocomposite

| <b>Mode of Deposition</b> | <b>Voltage Range</b> |
|---------------------------|----------------------|
| Dripping                  | 0- 4.9 kV            |
| Micro Dripping            | 4.9-5.5 kV           |
| Unstable Cone-Jet         | 5.5-6.2 kV           |
| Stable Cone-Jet           | 6.2-7.1 kV           |
| Multi-stable Cone-Jet     | > 7.1 kV             |

Finally the top Ag electrode was deposited by again using Ag nanoparticles ink. This task was performed via employing a non-contact technique by using the in-house developed electrohydrodynamic (EHD) patterning system. EHD patterning was preferred over other contact based printing techniques like screen printing, reverse offset and gravure offset because they could have damaged the MoS<sub>2</sub>-PVA based thin film resulting in a short circuit between top and bottom electrodes. However, on the other hand EHD patterning is a non-contact method with no such disadvantage. A single electrode of Ag nanoparticles ink with 30 μm width and 9 mm length was successfully deposited as the top electrode without damaging active thin film or bottom Ag electrodes as illustrated in Fig. 19. The optimized parameters during the deposition of top Ag electrode are listed in Supplementary Table 13. Top Ag electrode was sintered at 110 °C for 1 hour. The deposited electrode was highly conductive as its measured resistivity was only 0.2 Ω cm<sup>-1</sup>.

Total area of as fabricated Ag/MoS<sub>2</sub>-PVA/Ag single memory cell was 30 μm × 100 μm. The optical images of as deposited bottom and top electrodes taken at various resolutions are presented in Fig.20 as a proof of their uniformity.

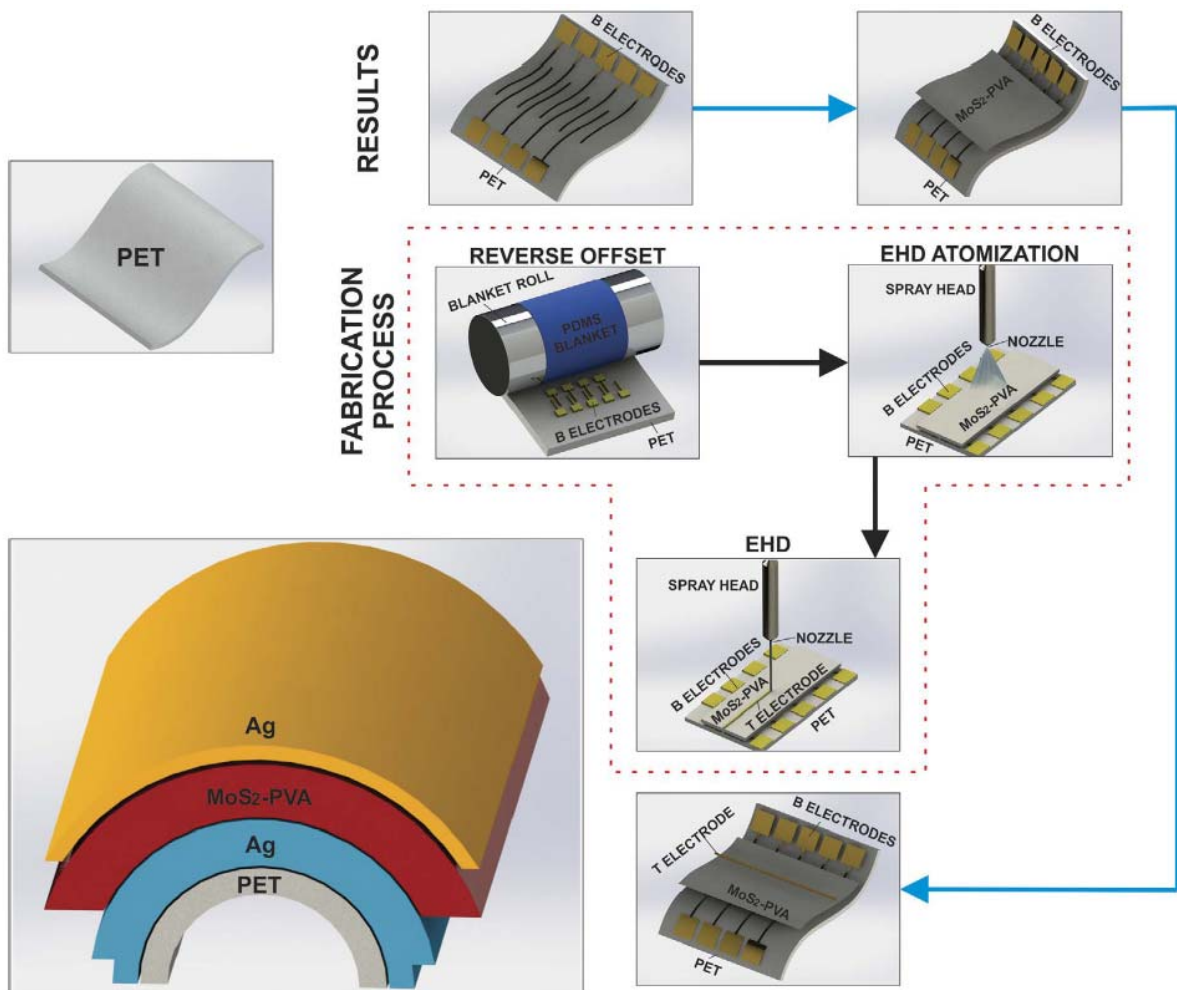


Figure 19. Schematic diagram illustrating the whole manufacturing process of as fabricated memory device on a flexible PET substrate. The images enclosed in the red dotted block exhibit each step of the fabrication process while the images outside the block correspond to the resulting device after each step. The bottom left corner exhibit layer by layer sandwiched structure of a single memory cell in bend state with PET/Ag/MoS<sub>2</sub>-PVA/Ag configuration



Table 13. Optimized condition and their set values during the deposition of top Ag electrode through EHD Patterning Process of Top Ag Electrode

| Parameter                    | Optimized Value  |
|------------------------------|------------------|
| Nozzle to Substrate Distance | 5 $\mu\text{m}$  |
| External Nozzle Diameter     | 30 $\mu\text{m}$ |
| Nozzle Speed                 | 0.3 mm/s         |
| Applied Pressure             | 64.6 kPa         |

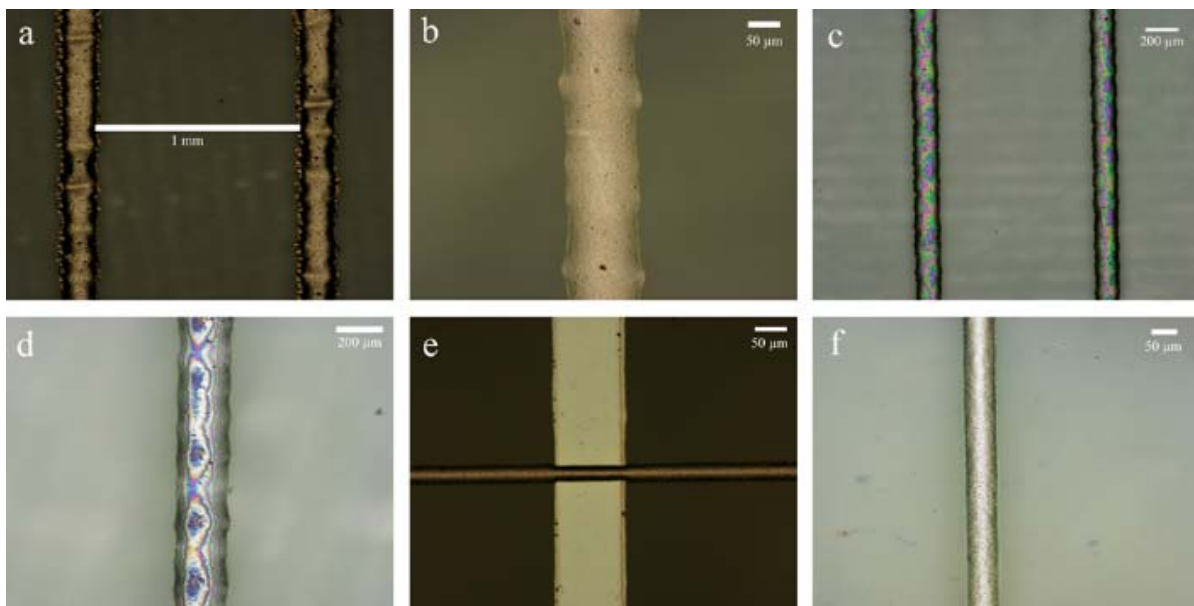


Figure 20. Optical images of bottom and top Ag electrodes displaying their high quality patterned by using reverse offset and EHD patterning systems respectively a) gap between side by side patterned bottom electrodes b) Magnified image of a single bottom electrode c) Two consecutive bottom electrodes with a thin film of MoS<sub>2</sub>-PVA nanocomposite coated on them by EHDA d) Magnified image of a single bottom electrode with a thin film of MoS<sub>2</sub>-PVA nanocomposite coated on it by EHDA e) Image of top electrode bisecting the bottom Ag electrode f) Magnified image of top electrode displaying its remarkably uniform surface

### 3 Resistive switching in as synthesized 2D materials and their nanocomposites

#### 3.1 Flexible Ag/WS<sub>2</sub>/Ag RRAM

##### 3.1.1 Electrical Characterization

Electrical characterization of WS<sub>2</sub> based memory devices was carried out by using Aglient

B1500A Semiconductor Device Analyzer. The obtained results in the form of I-V curves are illustrated in Fig. 21. It is extremely important to mention here that the memory behavior shown by our device was electroforming free that adds to its value as it simplified the memory operation. When direct DC bias was applied across the two terminals of Ag/WS<sub>2</sub>/Ag device, a characteristic bipolar resistive switching behavior was observed with the magnitude of its SET and RESET voltage to be ~ 2.3 V each as illustrated in Fig. 21(a). These values of SET and RESET voltage signifies that digital data can be stored and erased from our memory device at ~ +2.3 V and ~ -2.3 V respectively. A low current compliance value of 50  $\mu$ A was fixed to protect the device from hard breakdown and to reduce its power consumption. The device was originally in HRS that turned to LRS when the magnitude of applied bias reached to threshold voltage ( $V_{th}$ ) value of 2.3 V. It can be seen from the given I-V curves of Fig. 21 that both resistive states (HRS and LRS) can easily be distinguished from each other which is a necessary requirement for all memory devices.

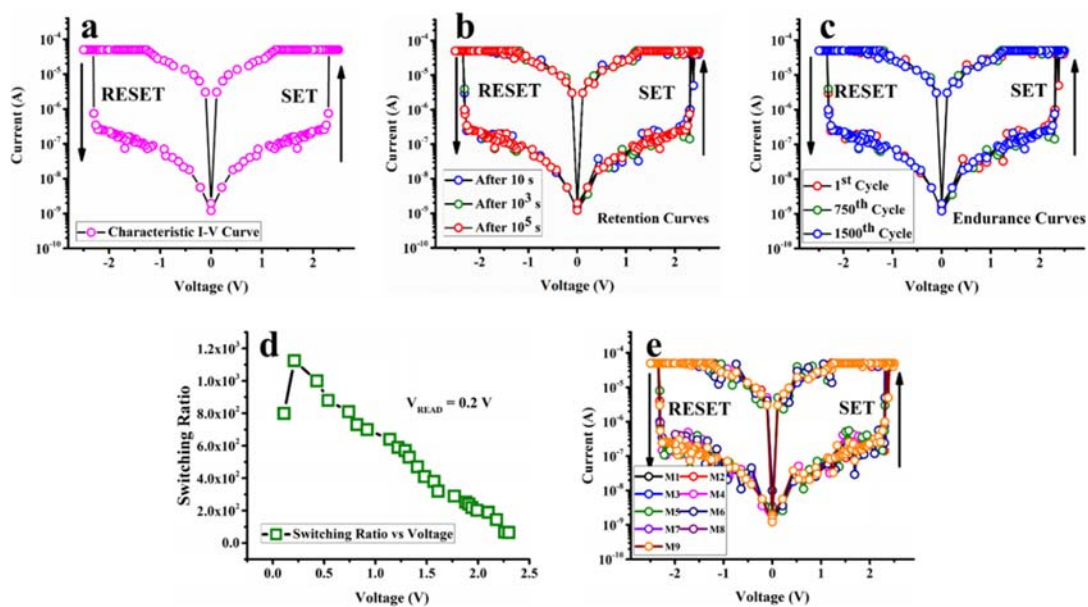


Figure 21. Electrical characterization results of WS<sub>2</sub> based memory device (a) Characteristic bipolar I-V curve (b) retention I-V curves for a 10<sup>5</sup> s (c) high endurance I-V curves for 1500 voltage sweeps (d) inverse relation of switching ratio with increasing applied voltage (e) High repeatability of as fabricated memory device as illustrated by the overlapping I-V curves of each of the nine memory cells chosen randomly

The value of HRS and LRS as recorded from the obtained characteristic I-V curve were 37.5 M $\Omega$  and 33.3 K $\Omega$  respectively at a read voltage ( $V_{\text{READ}}$ ) of 0.2 V. The developed memory device showed significantly high data retention without any prominent change for more than  $10^5$  s as illustrated in Fig. 21(b). The as fabricated device was tested for more than 1500 DC biasing cycles and its results are shown in Fig. 21(c). It can be seen that along with high retention time, the developed memory device exhibited high electrical endurance as well. The trend of switching ratio with increasing value of applied bias is shown in Fig. 21(d) with the maximum ratio of  $\sim 10^3$  at  $V_{\text{READ}}$  of 0.2 V. The switching ratio kept decreasing with increasing voltage due to reduction in gap between LRS and HRS. The fabricated array of our memory device consisted of nineteen memory cells. In order to examine the reliability of our used fabrication techniques and reproducibility of device performance, I-V curves of nine random memory cells were plotted as illustrated in Fig. 21(e). The obtained I-V curves of all the randomly chosen memory cells were highly repeatable. It can be observed from the I-V curves of Fig. 21 that the obtained results were highly symmetric due to the use of same metal electrodes with similar work function as anode and cathode and single functional layer.

In order to check the effectiveness of Al<sub>2</sub>O<sub>3</sub> encapsulating thin film, we obtained the electrical response of our memory device in environments with varying levels of humidity and temperature. The obtained I-V curves were highly stable without any degradation in the original values as illustrated in Fig. 22. The humidity value was raised up to 60 %RH while the temperature was raised up to 50 °C as illustrated in Fig. 22(a) and Fig. 22(b) respectively. The encapsulation of Al<sub>2</sub>O<sub>3</sub> seems to function perfectly making our memory device to be operatable in harsh atmospheric conditions with great repeatability.

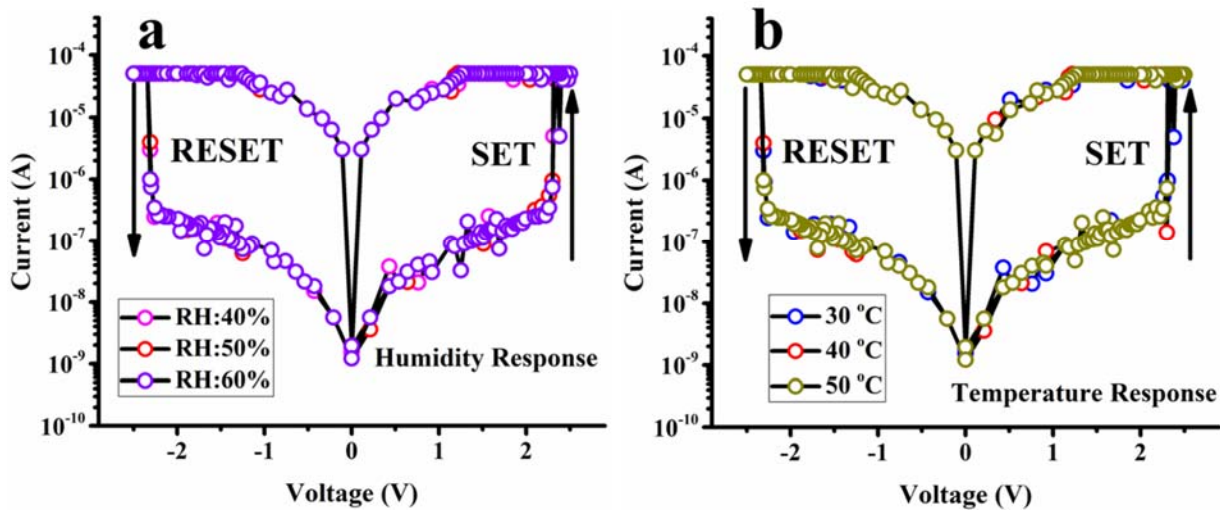


Figure 22. Characteristic I-V curves of developed memory device with a sandwiched layer of WS<sub>2</sub> layered material in harsh environments. (a) with humidity ranging from 40% RH- 60% RH (b) with temperature varying from 30 °C – 50 °C.

### 3.1.2 Conduction Mechanism

Conduction mechanism of resistive switching devices has long been a point of discussion among the researchers working on this electronic device. Plotting a double logarithmic graph is said to be an important tool to reach some sort of conclusive evidence for the observed conduction model of such memory devices. Therefore, a set of two double logarithmic I-V curves was plotted for both the HRS and LRS regions of our device for the verification of its conduction mechanism as illustrated in Fig 23. It can be clearly seen that for smaller values of applied positive bias, the slope of the double logarithmic graph in HRS was  $\sim 1$  ( $I \propto V$ ) that implies its ohmic nature however, with increasing value of applied voltage, the value of slope increased to  $\sim 2$  ( $I \propto V^2$ ) as illustrated in Fig. 23(a). Such behavior signifies the existence of trap controlled space charge limited current (TCSCLC) model in HRS [79–82].

The current tend to abruptly increase at  $V_{th}$  to switch the device from OFF to ON state at 2.3 V. The obtained double logarithmic I-V graph of LRS is linear with a slope value of  $\sim 1$  ( $I \propto V$ ),

signifying the ohmic conduction model implying that current linearly increase with applied value of voltage. TCSCLC model is highly related to the trapping and detrapping of electrons in trap sites that is a commonly observed phenomena in semiconducting functional thin films of memory devices [83–85]. At low values of applied voltage, conduction of charge carriers can be due to the thermionic emission effect in which only a small number of electrons are allowed to take part in conduction from one electrode to the other electrode by passing through the functional material. This low current corresponds to the HRS of the developed memory device.

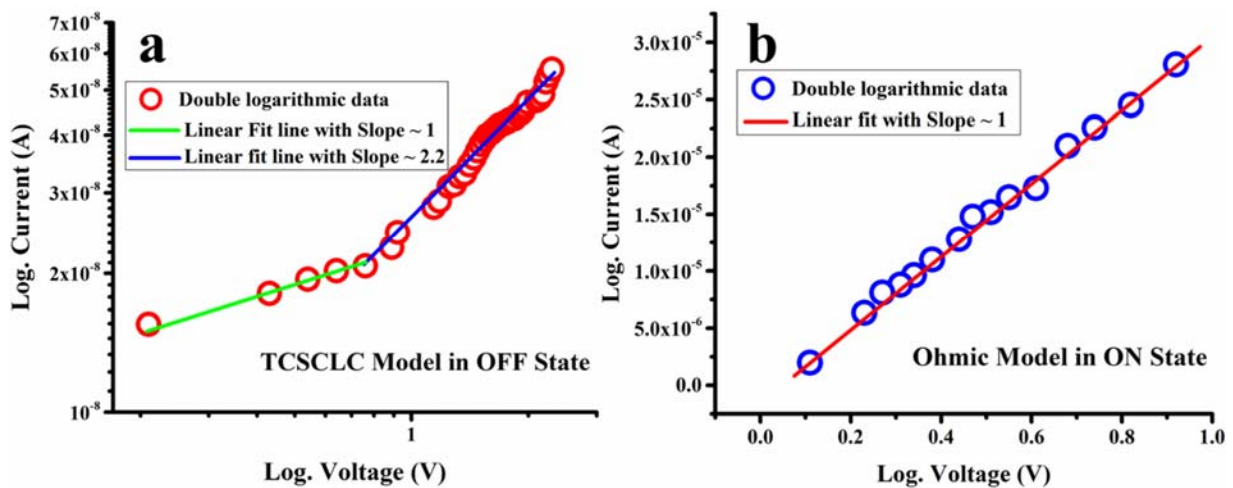


Figure 23. Conduction mechanism as explained by the double logarithmic graph of the I-V curve. (a) This graph suggest that TCSCLC is followed in the HRS while (b) Ohmic current model satisfies the conduction of LRS

The number of charge carriers taking place in conduction increase with increasing magnitude of applied electric field that results in more electrons crossing the potential barrier. At a specific value of applied voltage bias ( $V_{th}$ ), all the traps of functional thin film are filled hence, resulting in increasing density of free electrons. An abrupt increase in the passing electric current is observed ( $I \propto V^m$ ) due to the formation of conduction paths throughout the functional thin film of  $WS_2$ , resulting in switching the device from OFF to ON state. The traps present inside the  $WS_2$  thin film are deep enough to hold the charge carriers for a long time even if the externally applied

electrostatic force is removed resulting in the nonvolatile memory behavior of our device as shown in Fig. 23(b). In order to switch the device back to its original state of HRS, a voltage bias with opposite polarity must be given to the proposed memory device so that charge carriers get enough energy to leave those trap sites causing this bipolar memory behavior. The device returns to HRS with an applied bias voltage of negative polarity due to the destruction of conduction paths throughout the functional thin film of WS<sub>2</sub> sandwiched between the two electrodes and suddenly the trap sites again become empty at a  $V_{th}$  of -2.3 V.

### 3.1.3 Mechanical Characterization

Flexible memory devices can find its applications in wearable electronics and health monitoring systems. Mechanical characterization of this flexible memory device was carried out for various bending cycles (1500 cycles) and at different bending diameters (50-5 mm) as illustrated in Fig. 24. These measurements were recorded by clamping the two ends of our device in between the jaws of a custom made mechanical machine by moving the device in forward and backward direction. Both HRS and LRS were plotted against various bending cycles at a fixed bending diameter of 15 mm without any significant change in their values as illustrated in Fig. 24(a). Furthermore, the memory device was bend at various bending diameters and values of both bistable resistive states (HRS and LRS) were plotted against decreasing magnitude of bending diameter. The obtained results were highly repeatable as shown on Fig. 24(b). These results clearly shows that our device exhibited excellent mechanical endurance and robustness and is highly suitable to be used as a flexible memory device.

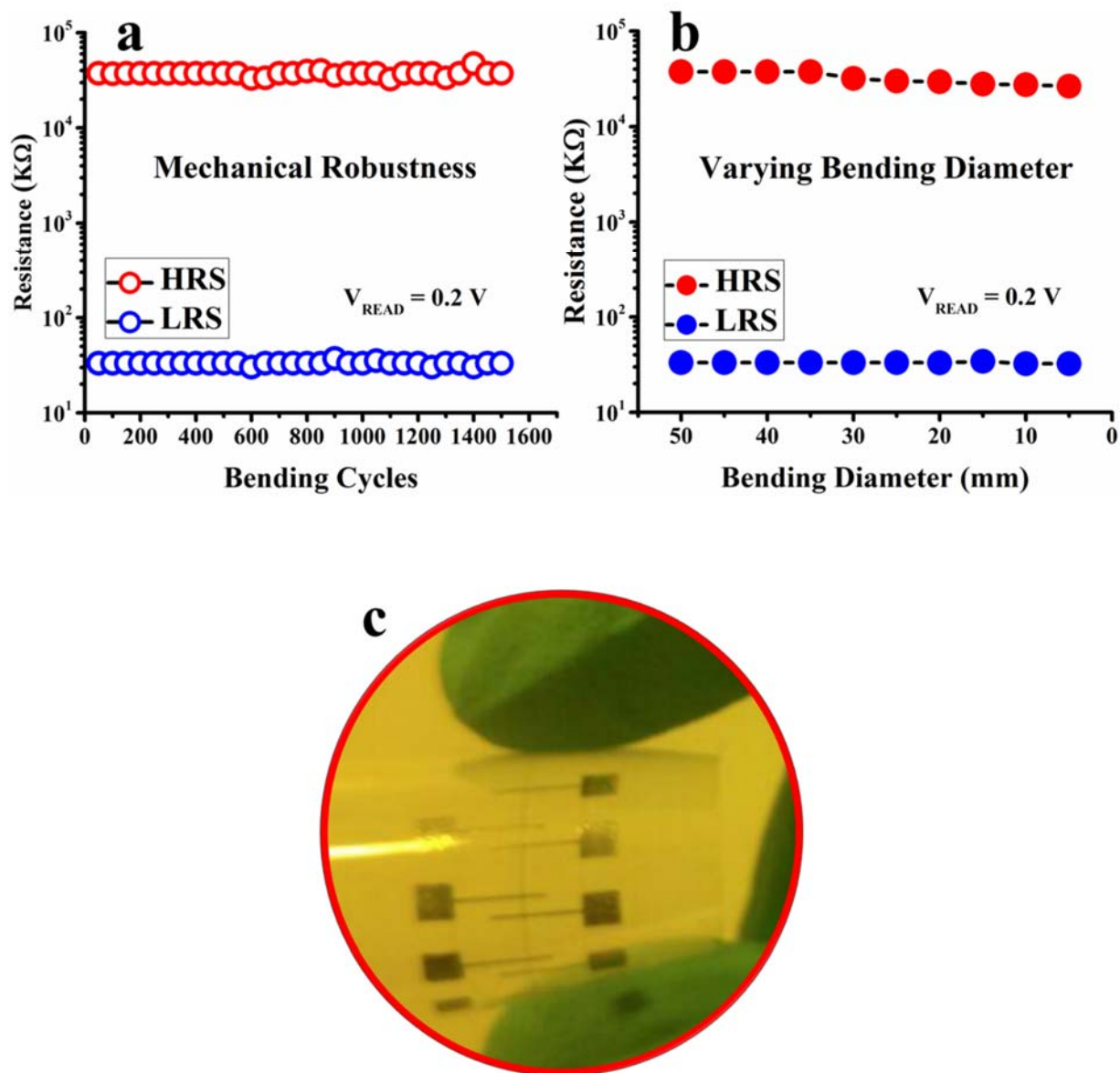


Figure 24. Mechanical characterization results of as fabricated memory device on a flexible substrate (a) Mechanical robustness against 1500 bending cycles (b) Mechanical robustness against various bending diameters from 50 mm to 5 mm. (c) Optical image of as fabricated WS<sub>2</sub> based memory device in bend state.

## 3.2 Flexible Ag/hBN-GQDs/Ag RRAM

### 3.2.1 Electrical Characterization

Electrical analysis of as fabricated Ag/hBN-GQDs/Ag memory device with a planar structure was carried out by applying an electric field across both electrodes. Anode was connected to the driving

terminal while the cathode was grounded. Before applying a double voltage sweep, the device was passed through electroforming process in the range of 0-9 V to achieve stable resistive switching behavior as shown in Fig. 25(a). After electroforming, double voltage sweep was applied across both terminals with a voltage sweep of -5 V to +5 V that resulted in a characteristic bipolar resistive switching behavior as illustrated in Fig. 25(b).

The device was initially in a HRS. As the magnitude of positively biased voltage was increased, current passing through the functional layer also increased, resulting in switching of resistive state from HRS to LRS at a  $V_{th}$  of  $\sim 4$  V known as SET process. At  $V_{th}$ , data can be stored or written on this memory device. The resistance value of HRS and LRS at a  $V_{READ}$  of 0.9 V were  $9 \times 10^8$  and  $2 \times 10^5$  respectively. In order to bring the device back to its initial state of HRS, a voltage bias of same magnitude with opposite polarity was applied. The obtained I-V curve was highly symmetric owing to the use of similar metal electrodes (Ag) as anode and cathode. A maximum switching ratio of  $\sim 5 \times 10^3$  was recorded at a  $V_{READ}$  of 0.9 V. The overall trend of switching ratio at various other values of  $V_{READ}$  is depicted by Fig. 25(c). The switching ratio keeps on increasing almost linearly till 0.6 V and remains nearly constant from 0.6 V - 0.9 V. After 0.9 V the switching ratio begin to decrease. A total of ten memory cells were characterized to check the repeatability of our device. It can be seen from the resulting I-V curves of Fig. 25(d) that each memory cell exhibited similar behavior with very less deviation from the original result hence proving the high repeatability and reliability of fabricated device.



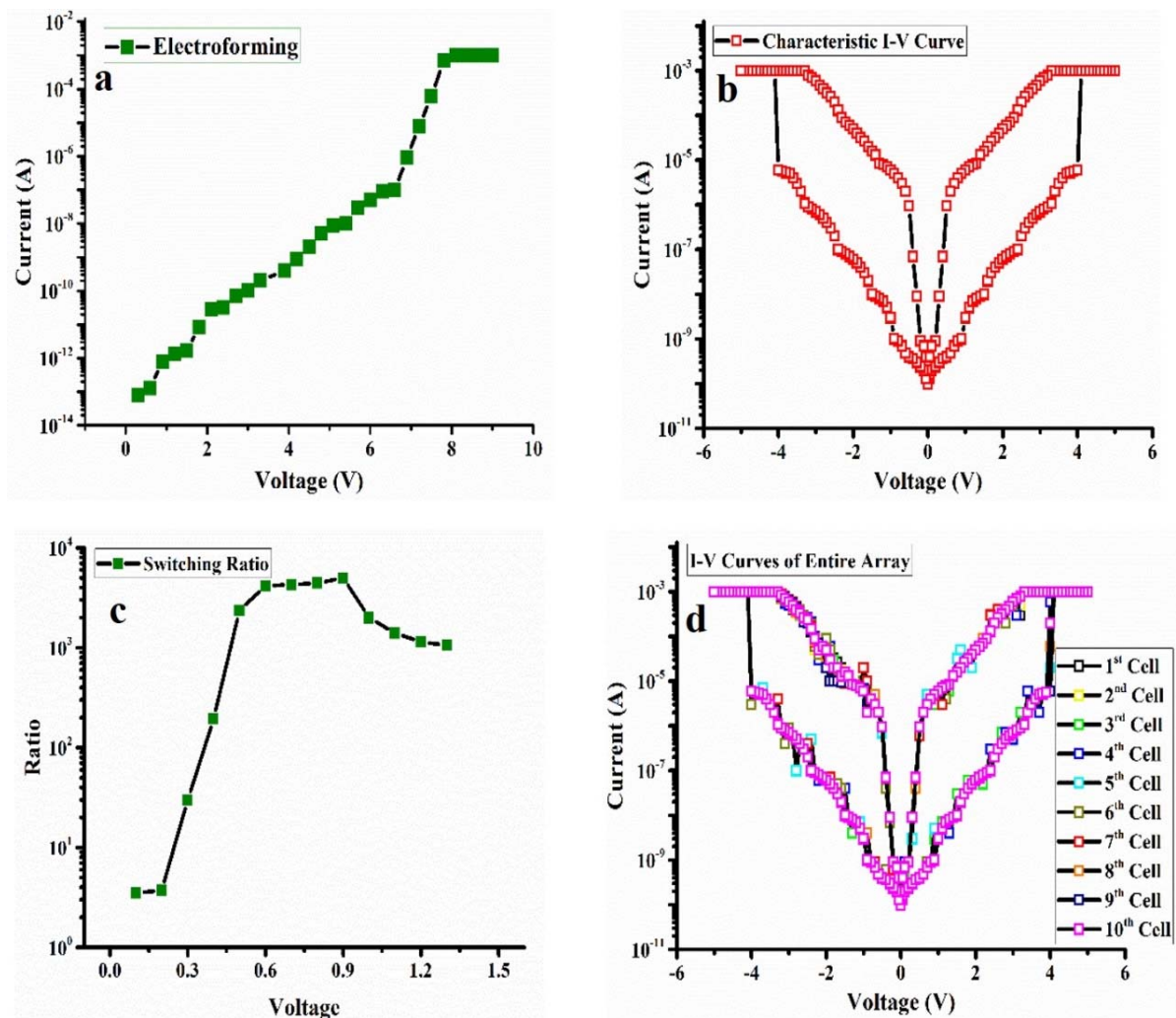


Figure 25. Electrical characterization results of as fabricated NVM device (a) Electroforming curve before applying double voltage sweep (b) Characteristic bipolar I-V curve showing memory effect (c) Illustration of switching ratio with increasing voltage. The switching ratio is maximum at a read voltage in the range of 0.6 V - 0.9 V (d) I-V curves of whole memory cell array illustrating highly repeatable memory behavior in each cell

Moreover, extremely encouraging results of electrical endurance were obtained when the memory device was tested against several voltage sweeps as illustrated in Fig. 26(a). This device was also examined for the NVM behavior and I-V characteristic curves were obtained for several hours. No prominent deterioration in the obtained results was observed implying great ability of our device to retain data for a long time as illustrated in Fig. 26(b). The stability and distribution of  $V_{th}$  and

bistable resistive states (HRS and LRS) was also observed by plotting their cumulative probability plots as illustrated in Fig. 26(c) and Fig. 26(d) respectively.

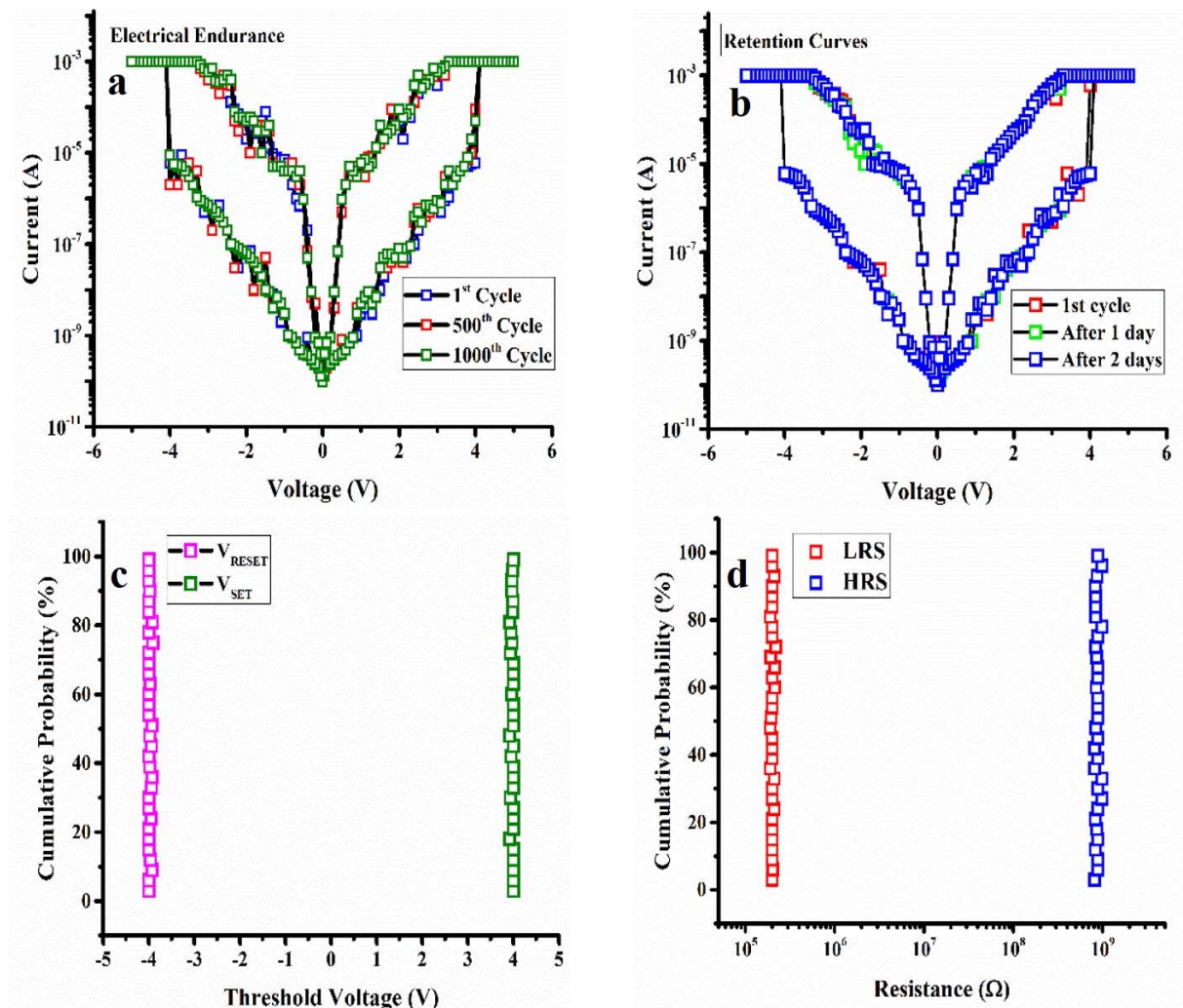


Figure 26. (a) Electrical endurance curves for 1000 voltage sweeps with high stability (b) Illustration of high retentivity owing to the protection by the encapsulation coating of  $\text{Al}_2\text{O}_3$  through ALD (c) Cumulative probability plot of threshold voltages (both SET and RESET) showing high stability in the obtained results (d) Cumulative probability plot of bistable resistive states (both HRS and LRS) showing high stability in the obtained results with negligible deviation

### 3.2.2 Conduction Mechanism

After performing the electrical characterization and inspecting the obtained results, possible conduction mechanism of our device was studied carefully. Conduction mechanism of resistive

switching is mostly classified in two categories i.e. interface type and filament type switching [86]. The sudden increase of electric current passing through our device and requirement of electroforming voltage before applying double voltage sweep were a few indications of filamentary conduction mechanism. To verify the mechanism of our device, we measured the effect of temperature on the bistable resistive states (HRS and LRS). Bistable resistive states were plotted against increasing temperature as illustrated in Fig. 27(a).

The linear increase in LRS with increasing temperature is evident of the presence of a metallic filament as metals have a positive temperature coefficient. A decrease in the values of HRS with an increase in temperature signified the semi-conductive nature of all 2D nanocomposite functional thin film and dissolution of metallic filament [39]. The obtained results verify the conduction mechanism to be conductive filamentary type. The formation and rupture of a metallic filament from anode to cathode can be divided into four steps such as i) Initial state ii) Filament formation iii) Set process and iv) Filament rupture/Reset. All the above mentioned four steps are illustrated in Fig. 27(b). Initially no bias is applied across the two terminals, so no filament was formed. When the positive bias was applied at the anode, neutral Ag metal atoms of anode released free electrons into the functional layer of hBN-GQDs. These electrons are trapped by the GQDs due to quantum confinement effect. Trapping of these charge carriers might be due the trap controlled space charge limited current (TCSCLC). As a result of losing electrons, neutral atoms of Ag anode change into positively charged  $\text{Ag}^+$  cations and repelled towards cathode owing to the positive bias of anode. Due to the low conductivity of  $\text{Ag}^+$  cations in the functional layer of hBNGQDs, these cations begin to reduce by the electrons trapped inside GQDs resulting in the formation of a metallic filament acting as an extended anode. This metallic filament keeps on growing and ultimately connects the anode with cathode. Charge carriers pass through the

functional layer of hBN-GQDs from anode to cathode resulting in switching the device from HRS to LRS, also known as writing process. When a negative bias is applied at the anode, the formed filament was annihilated probably from its thinnest part near the cathode thus bringing the device back to its original resistive state of HRS, also known as erasing process. This annihilation of metallic filament occurs due to joule heating effect and electrochemical process. Such a conduction mechanism has been reported for other memory devices as well based on resistive switching [87]. Many nano sized filaments throughout the functional layer would have formed, however, high current flows through a single filament with higher conductivity connecting both electrodes by masking the partially formed nano-filaments.

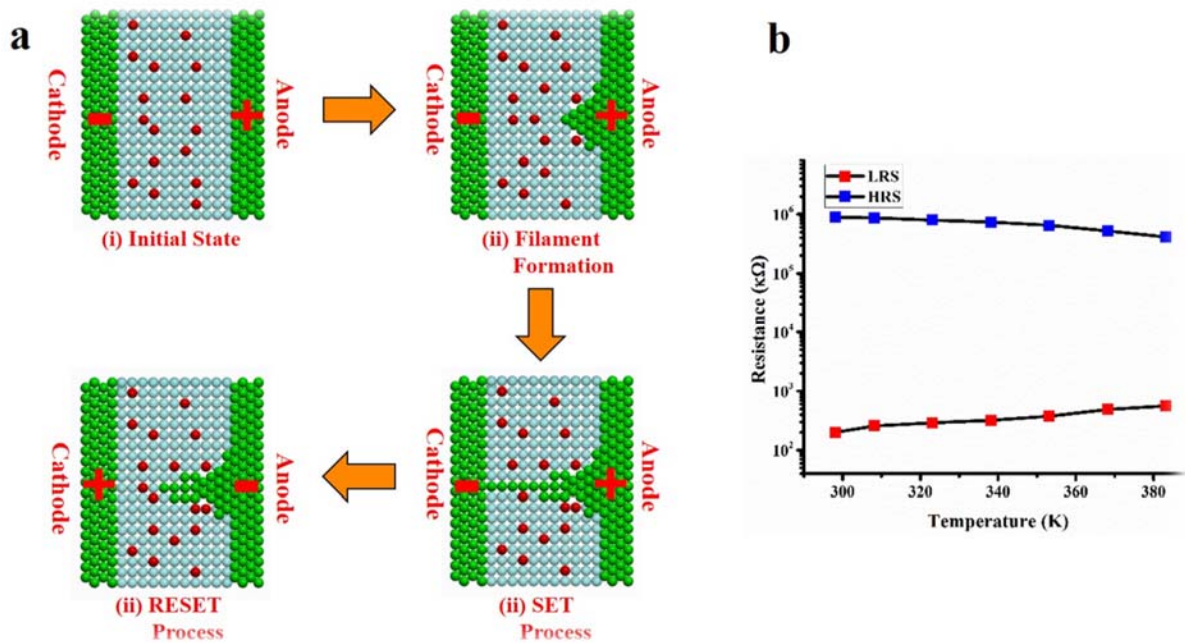


Figure 27. Illustration of working mechanism a) This part shows four different stages of filament formation and rupture such as initial condition (when Ag<sup>+</sup> cations are depleted in the functional layer), filament formation (where reduction of Ag<sup>+</sup> cations takes place), set process (A point where the formed filament connects anode with cathode to complete the pathway of charge carriers to flow) and finally the reset process (when voltage of opposite polarity is applied) b) Dependence of bistable resistive states (HRS and LRS) on temperature verifying the formation of metallic filament through the functional layer

### 3.2.3 Mechanical Characterization

Several efforts are being devoted to the choice of a right material to be used for flexible electronic applications. Preserving the retention and repeatability characteristics of a flexible memory device such as its electrical endurance, current levels, stability of bistable resistive states and switching ratio in a bend state are extremely important parameters. Organic polymers have high flexibility with a disadvantage of very low mobility while inorganic semiconductors have higher mobility values but they are too brittle to be used for flexible electronic applications. However, 2D materials offer both advantages of ultrahigh flexibility and higher mobility therefore we selected a blend of 2D materials as the functional layer of our proposed flexible memory device owing to their supreme breaking strength ( $15.7 \text{ N m}^{-1}$ ) and high elastic constant ( $503 \text{ N m}^{-1}$ ) making them an ultimate choice for flexible electronic devices.

These 2D materials are extremely flexible yet very light in weight. Mechanical robustness of our device was tested by quenching its two ends between the jaws of a customized machine. The obtained results of bistable resistive states against 2000 bending cycles at a bending diameter of 15 mm are illustrated in Fig. 28(a) while the stability of both HRS and LRS against various bending diameters up to 2 mm can be seen in Fig. 28(b). The schematic diagram and the optical image of as fabricated flexible memory device in a bend state are illustrated in Fig. 28(c) and Fig. 28(d) respectively. Optical images of as fabricated NVM device based on hBN-GQDs functional layer at various bending angles are illustrated in Fig. 29 to show its superior flexibility. Robustness of this advanced 2D nanocomposite against several tedious bending measurements without any prominent degradation of obtained results makes it an extremely useful choice for flexible memory device of the future.

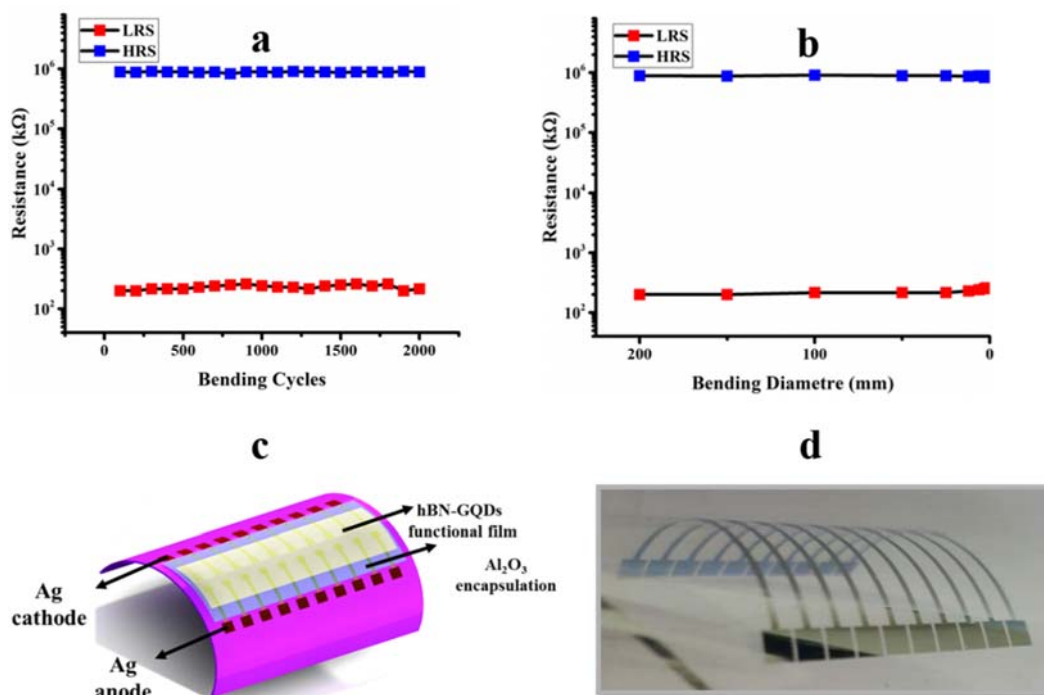


Figure 28. Mechanical characterization results of as fabricated flexible memory device a) Illustration of mechanical endurance for several bending cycles at a fixed diameter of 15 mm b) Display of mechanical robustness and stability over a range of bending diameters from 200 mm to 2 mm. c) Schematic diagram of as fabricated flexible memory device in bend state with labeling of each part d) Optical image of the developed memory device in bend state

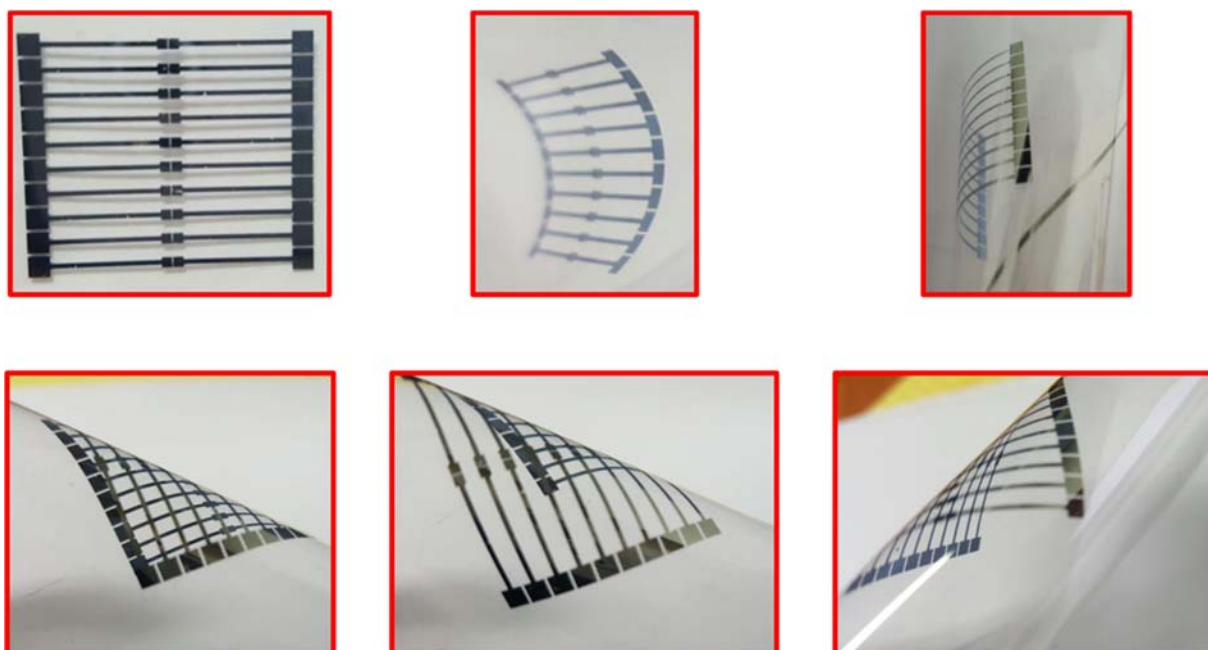


Figure 29. Optical images of as fabricated memory device obtained at various bending angles without any degradation of either electrodes or functional thin film

### 3.3 Flexible ITO/hBN-MoS<sub>2</sub>QDs/Ag RRAM

#### 3.3.1 Electrical Characterization

Resistive switching behavior of ITO/hBN-MoS<sub>2</sub>QDs/Ag based memory device was analyzed by performing electrical characterization on each of the three different fabricated device sizes i.e. 42  $\mu\text{m}$ , 70  $\mu\text{m}$  and 100  $\mu\text{m}$  respectively. Positive voltage sweep was applied to the top circular Ag electrode whereas bottom ITO electrode was connected with a ground to complete the electrical circuit. The fabricated device was initially in HRS. To avoid possible device breakdown and switch the device to LRS, current compliance value was optimized. Electroforming test was carried out before applying a double voltage sweep to obtain reliable electrical results by creating a conductive path between the two electrodes before applying double voltage sweep as shown in Fig. 30.

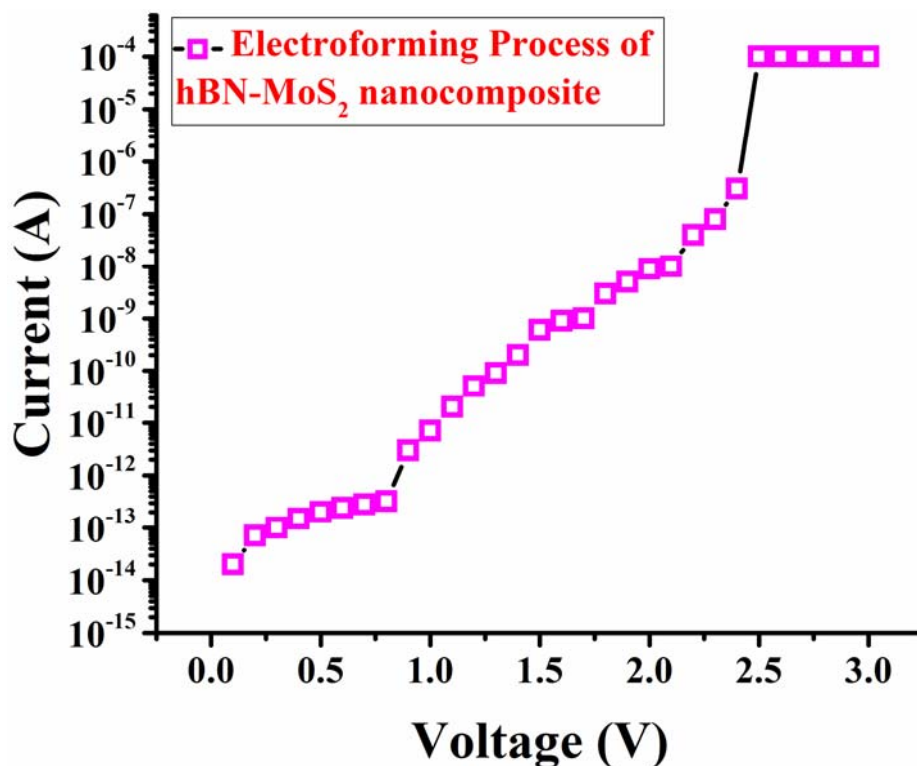


Figure 30. Electroforming Process of the fabricated device for the creation of conductive channel between top and bottom electrodes before observing repeatable bipolar resistive switching effect in them

2D nanocomposite of hBN-MoS<sub>2</sub>QDs exhibited characteristic semi-logarithmic curves of bipolar resistive switching when operated between -2 V to +2 V irrespective of the device size as shown in Figure 31(a-c). Current slightly increased from initial resistive state (HRS) due to applied external bias. It can be deduced from the characteristic I-V curves of fabricated devices that its SET voltage ( $V_{th}$  at which device switches from HRS to LRS) is  $\sim 1.4$  V. This sudden transition from HRS to LRS is termed as the writing process signifying the storage of a bit in memory cell. Thus, it can be inferred that data can be stored in the all 2D nanocomposite functional layer of hBN-MoS<sub>2</sub>QDs at a low threshold voltage.

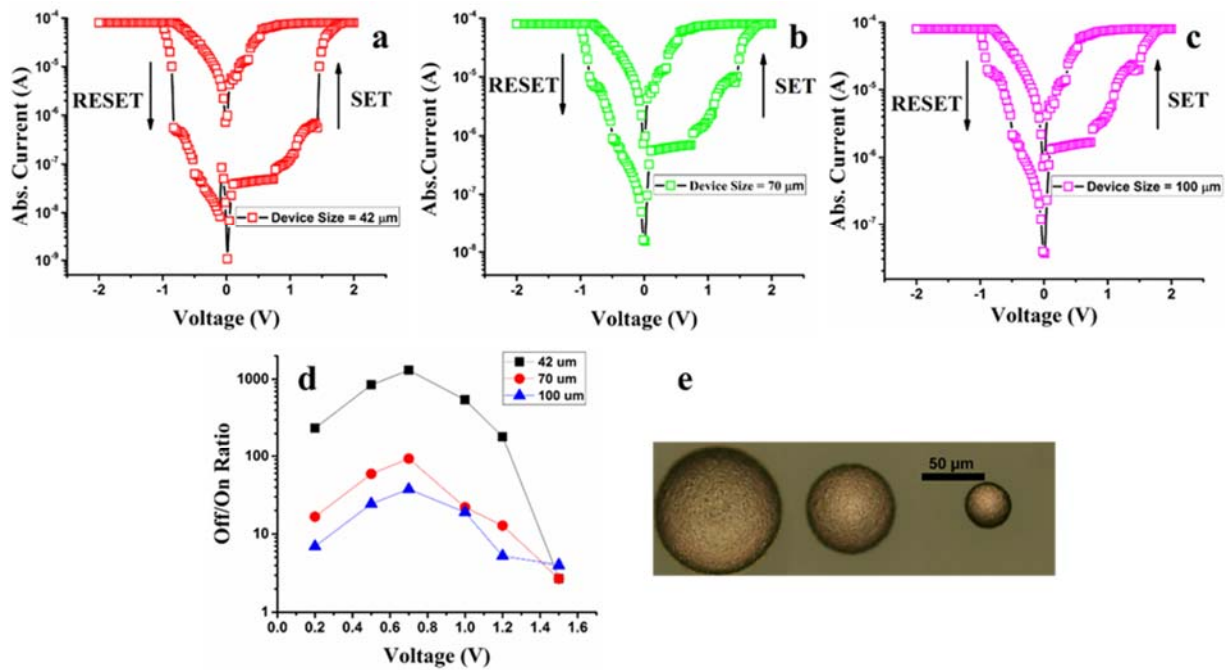


Figure 31. Characteristic bipolar resistive switching curves of as prepared non-volatile flexible memory device based on hybrid hBN-MoS<sub>2</sub> QDs nanocomposite (a) I-V characteristic curve of 42  $\mu\text{m}$  device (b) I-V characteristic curve of 70  $\mu\text{m}$  device (c) I-V characteristic curve of 100  $\mu\text{m}$  device (d) Switching ratio vs applied biased voltage showing their inverse relation (e) Optical images of the prepared devices with three different sizes of 100  $\mu\text{m}$ , 70  $\mu\text{m}$  and 42  $\mu\text{m}$  from left to right respectively with a scale bar of 50  $\mu\text{m}$

A good switching ratio as high as  $\sim 10^3$  was recorded for hBN-MoS<sub>2</sub>QDs nanocomposite at a  $V_{\text{READ}}$  of 0.7 V. A decreasing trend of switching ratio was observed with increasing voltage value as illustrated in Figure 31(d) for all the fabricated devices with different top electrode size. Optical



image of top electrodes with different sizes are displayed in Figure 31(e). The obtained results exhibited no significant change in either HRS or LRS for repeated biasing cycles (1000 voltage sweeps) and over a longer period of time ( $> 10^4$  s) signifying its highly robust and nonvolatile nature as illustrated in Fig. 32(a-b). Cumulative probability plots for the  $V_{th}$  ( $V_{SET}$  and  $V_{RESET}$ ) and bistable resistive states (HRS and LRS) showed highly repeatable values as illustrated in Fig. 32(c-d). Characteristic I-V curves of all the fabricated devices with different size are presented in a single plot for comparison of their switching ratio in Fig. 33.

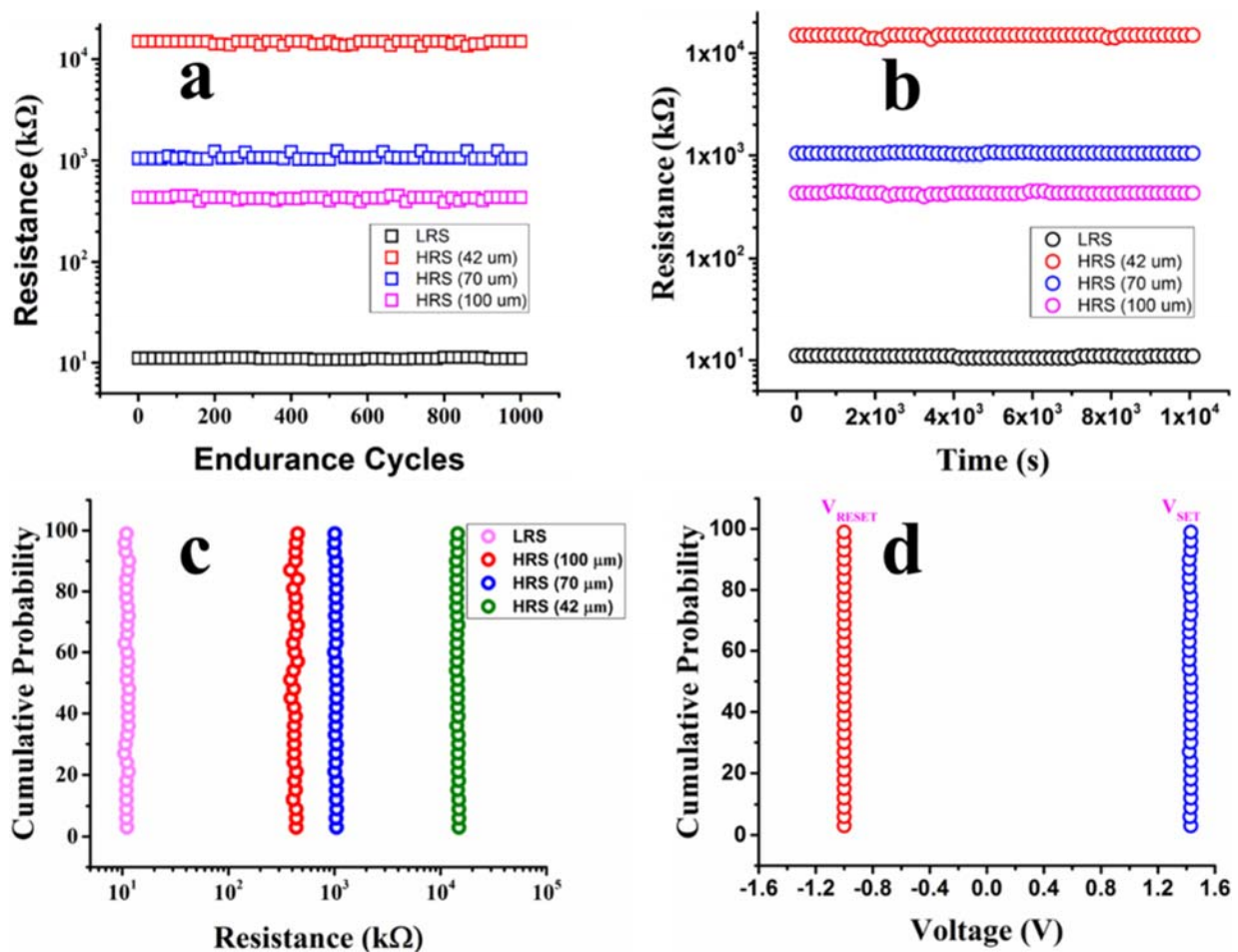


Figure 32. Durability of memory device based on all 2D functional layer against multiple voltage sweeps and for several hours along with cumulative probability plots of resistance and threshold voltages a) Electrical endurance for 1000 voltage sweeps without any considerable deviation b) High retentivity with high stability in both resistive states of all the three devices c) Cumulative probability plot of LRS and HRS d) Cumulative Probability curve of threshold voltages showing minor deviation

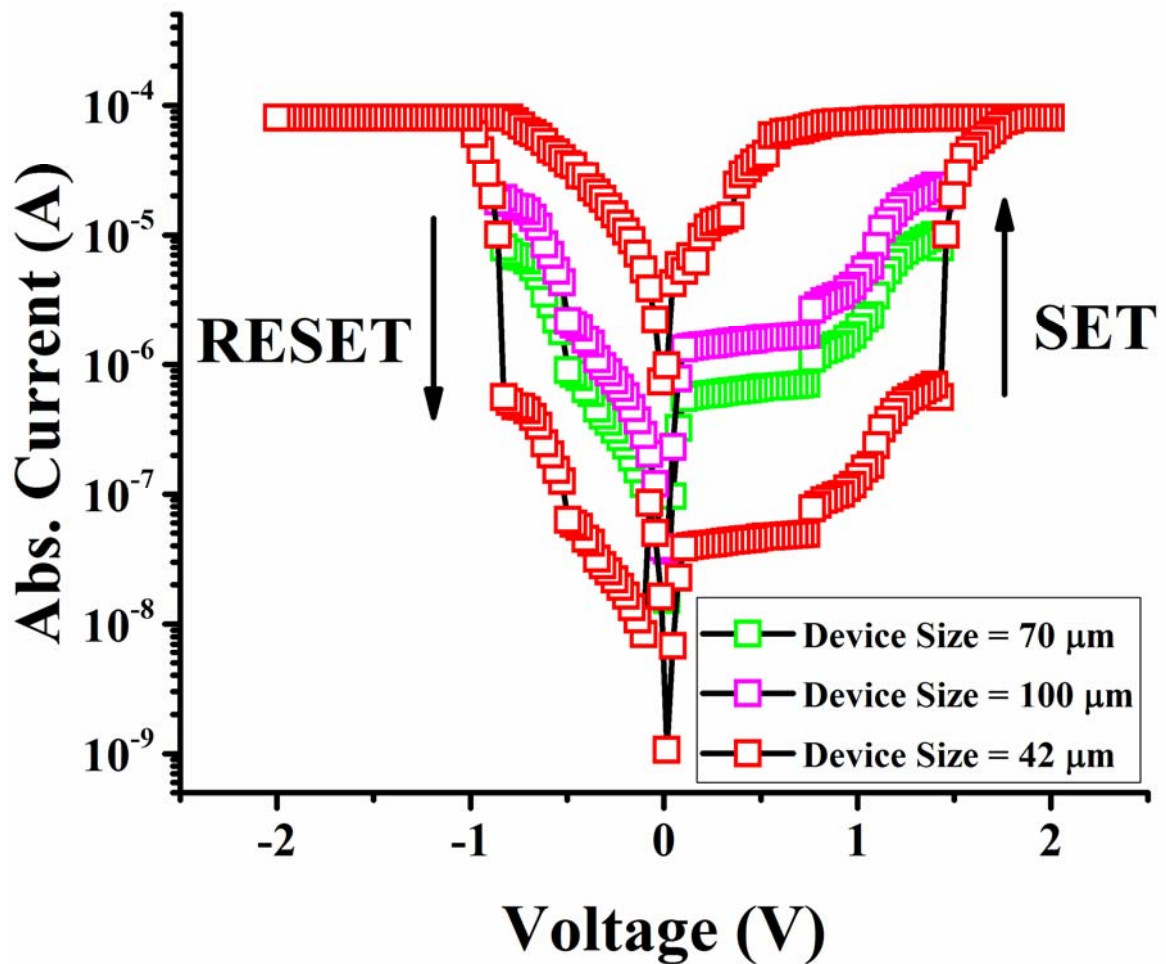


Figure 33. Typical bipolar I-V curves of all the three memory devices with different sizes of 42  $\mu\text{m}$ , 70  $\mu\text{m}$ , and 100  $\mu\text{m}$  respectively plotted against each other to clearly observe the difference between their switching ratios. LRS of all the devices is same however HRS tend to decrease with increasing device size hence resulting in smaller switching ratio

### 3.3.2 Conduction Mechanism

After performing the dc biasing and analyzing the obtained electrical results, the possible conduction mechanism of the considered 2D functional layer was studied cautiously. Conduction mechanism of a resistive switching device can be broadly classified in two classes i.e. interface and filament type switching [86,88]. However, particularly in our device the sudden increase in the flow of current as observed in the characteristic bipolar I-V curves of Figure 31(a-c) and the requirement of electroforming step before applying double voltage sweep indicate the formation

of a filament in the active layer. The process of filament formation is illustrated in Figure 34(a) that is divided into four parts i.e. i) initial state ii) forming iii) set and iv) reset. When positive bias is applied to the top Ag electrode, free charge carriers are released into the 2D active layer of hBN-MoS<sub>2</sub>QDs resulting in the formation and depletion of Ag<sup>+</sup> cations in the functional layer. These cations do not have the ability to travel far enough owing to their low mobility in the active layer before getting reduced by the electrons trapped inside the nearby MoS<sub>2</sub>QDs. Reduction of these cations result in the formation of neutral Ag atoms inside the functional layer thus a conductive metallic filament begin to form from the top Ag electrode acting as its extended part. Subsequent Ag<sup>+</sup> cations keep on reducing around this filament, preferably at the end of already formed filament as influence of electric field is the strongest at that point. This conductive path keep on forming in a downward direction till it reaches the bottom electrode and create a complete path for the excessive current to flow. At this point, the device switches from HRS to LRS also termed as SET or writing process. The thickness of the formed metallic filament is higher near the originating Ag electrode and reduces near the bottom ITO electrode. The device remains in the ON state i.e. the filament is not annihilated even if the external voltage supply is removed, signifying the nonvolatile nature of the fabricated device. In order to switch the device back to its original state of HRS, we applied an external bias of opposite polarity that resulted in the rupture of formed filament at V<sub>RESET</sub> also known as RESET or erasing process at which stored data is removed. This rupture occurs mainly due to the electrochemical process and Joule heating effect [88]. Magnitude of V<sub>RESET</sub> is lower than V<sub>SET</sub> because even a little dissolution of filament near the interface of hBN-MoS<sub>2</sub>QDs and bottom ITO electrode will result in the OFF state. The whole filament does not need to be dissolved. Such a formation and rupture of metallic Ag filament from top to bottom electrode has also been reported in other nonvolatile memory devices [87–90].

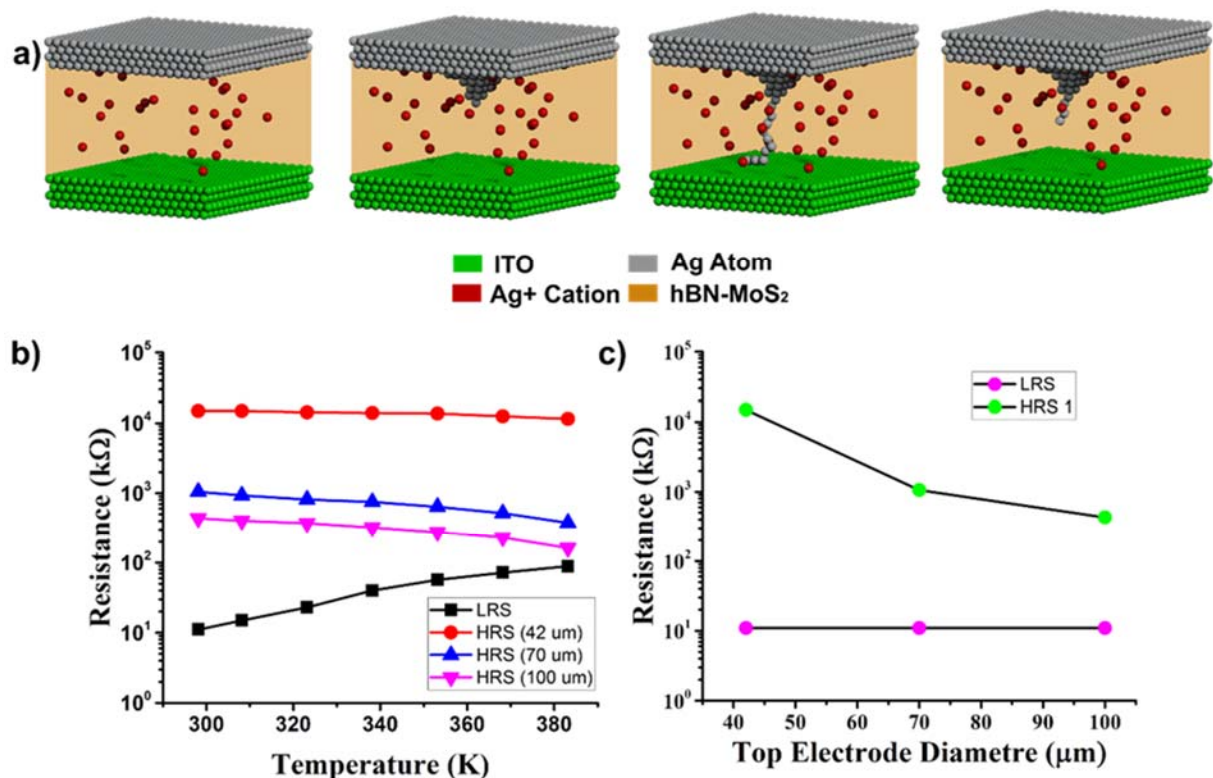


Figure 34. Schematic diagram of various stages of filament formation and rupture and its verification by temperature and device dependence of bistable resistive states. a) (i) Electrons are depleted from the top electrode followed by the injection of Ag<sup>+</sup> cations into the active layer (ii) Injected Ag<sup>+</sup> cations travel slowly within the active layer and thus they are reduced by the nearby trapped electrons. This causes the growth of Ag filament as an extension of top electrode (iii) The filament growth continues until it connects top electrode with bottom electrode hence switching the device into ON state (writing process) (iv) A bias of opposite polarity is applied to rupture the filament from its thinnest part near the bottom electrode to turn the device back to its OFF state (erasing process) b) Illustration of temperature dependence on the resistive states of the fabricated device c) Illustration of device size dependence on the resistive states of the fabricated device

However, further experimental results were required to verify the conduction mechanism of our device and infer the formation of metallic filament. We plotted both resistive states against increasing temperature and device size as illustrated in Figure 34(b-c). These obtained results provided a conclusive evidence of a metallic filament being formed between the two electrodes. Figure 34(b) clearly shows that LRS linearly increases with increasing temperature signifying the presence of a conductive filament owing to the positive temperature coefficient of metals. HRS of each device decreases with increasing temperature signifying the semiconductive nature of the

functional thin film with a negative temperature coefficient [91–94]. To further validate the conduction mechanism, area dependence of the resistive states was observed and it was found that LRS was independent while HRS was highly dependent upon the device size. HRS decreases with increasing device size while LRS remains constant [42,95,96]. With increasing device size, number of defects also increase thus resulting in a decrease of HRS magnitude due to the flow of leakage current. Large memory cell has more defects than smaller one resulting in a reduced switching ratio. The independence of LRS on device size shows that the conduction is due to the localized formation of filaments. Many nano sized filaments throughout the functional layer would have formed, however, high current flows through a single filament with higher conductivity connecting both electrodes by masking the partially formed nano filaments.

### 3.3.3 Mechanical Characterization

Several organic semiconductors and polymers with memory behavior have promising flexibility but their extremely low conductivity is a big constraint in such electronic applications. Conventional inorganic semiconductors have substantially high conductivity than organic polymers but they are too brittle and non-flexible however, 2D materials offer both advantages of high conductivity and super flexibility making them an ultimate choice for flexible memory devices [97,98,34]. Our device based on the sandwiched structure of ITO/hBN-MoS<sub>2</sub>QDs/Ag was fabricated on a flexible PET substrate to examine the mechanical robustness of this advanced functional 2D nanocomposite. The bistable resistive states were plotted against decreasing bending diameter extending from 500 mm to 4 mm without any prominent degradation in either HRS or LRS values as illustrated in Figure 35(a). The fabricated memory device was bent against various bending cycles by quenching it between the jaws of an in-house developed mechanical machine specifically designed for repeatable bending test at a desired curvature. The device was squeezed

back and forth for 1500 cycles at a bending diameter of 10 mm respectively and both the resistive states were recorded at a reading voltage of 0.7 V. The fabricated device exhibited outstanding mechanical strength against repeated bending cycles as no considerable deviation in either HRS or LRS was observed as illustrated in Figure 35(b). The schematic diagram of flexible 2D memory device is shown in bend state in Figure 35(c) with labelling of each part. These bendability tests express that hBN-MoS<sub>2</sub>QDs based memory device is extraordinarily appropriate to be used for flexible electronics applications.

A thorough comparison of as fabricated device is presented in Table 14 that shows the importance of this advanced 2D nanocomposite over several other hybrid and non-hybrid nanocomposites as a functional layer for flexible memory device.

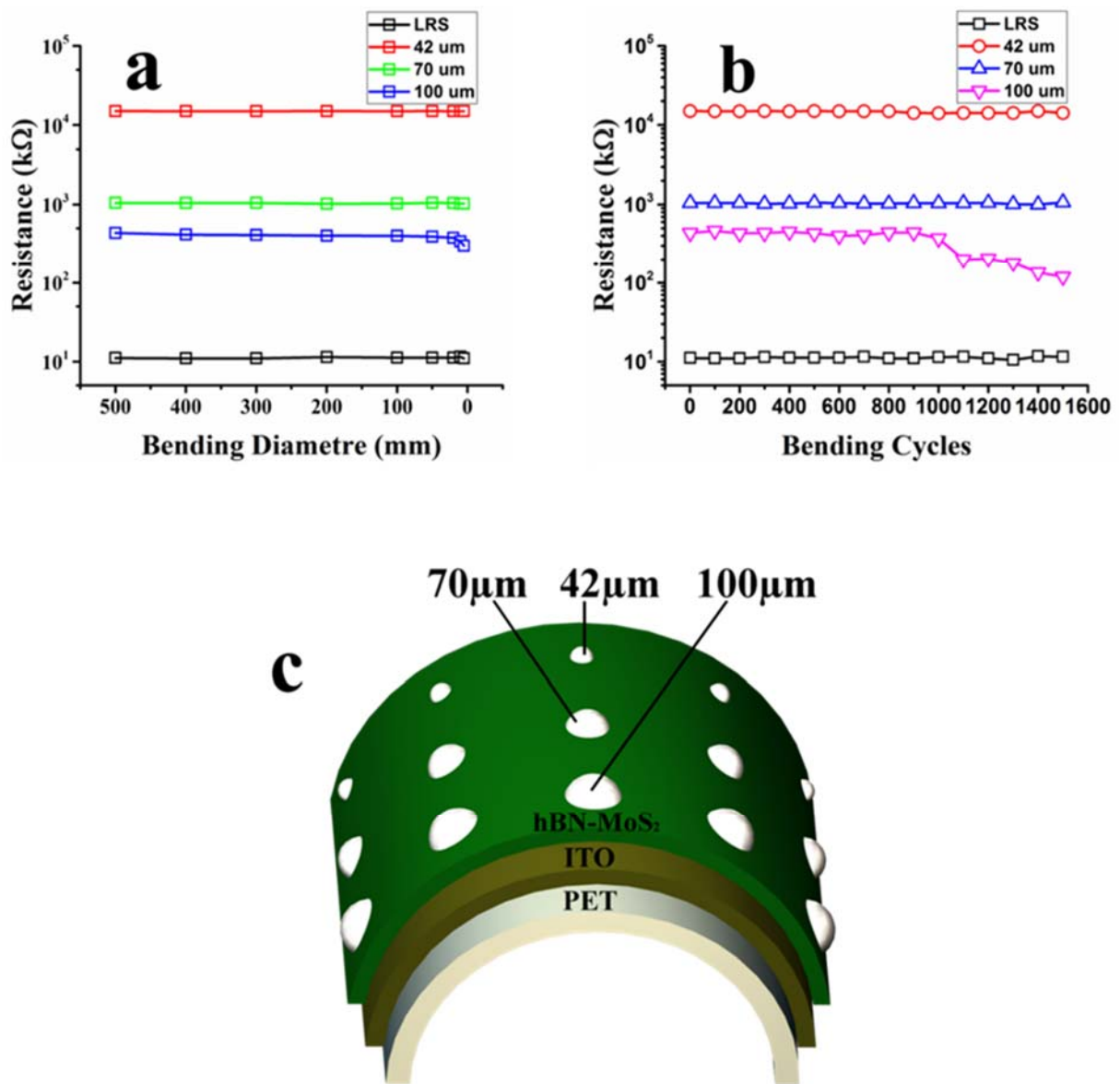


Figure 35. Mechanical characterization of as fabricated flexible memory device a) Mechanical bending test for various bending diameters b) Endurance test for 1500 bending cycles at a fixed bending diameter of 10 mm without any major difference in the bistable resistance values c) Schematic diagram of flexible memory device in bend state with labelling of each part

Table 14. Comparison of various resistive switching device parameters of as fabricated memory device with other hybrid and non-hybrid nanocomposite active layer materials

| Nanocomposite              | Operating Voltage (V) | Switching Ratio            | Electrical Endurance (Cycles) | Data Retention (s)    | Mechanical Robustness (Cycles) | Maximum Bendability (mm) |
|----------------------------|-----------------------|----------------------------|-------------------------------|-----------------------|--------------------------------|--------------------------|
| <b>hBN-MoS<sub>2</sub></b> | <b>-2 to +2</b>       | <b>&gt; 10<sup>3</sup></b> | <b>10<sup>3</sup></b>         | <b>10<sup>4</sup></b> | <b>1500</b>                    | <b>4</b>                 |
| PEDOT:PSS-PVA              | -2 to +2              | 10 <sup>2</sup>            | -                             | 10 <sup>4</sup>       | -                              | -                        |
| GNF-PVA                    | -7 to +2              | 10 <sup>2</sup>            | 10 <sup>2</sup>               | 10 <sup>4</sup>       | -                              | -                        |
| MoS <sub>2</sub> -PVA      | -4 to +4              | 10 <sup>2</sup>            | 10 <sup>3</sup>               | 10 <sup>5</sup>       | 1500                           | 2                        |
| AgNW-PVA                   | -10 to +10            | 10                         | 160                           | -                     | -                              | -                        |
| PVP-MoS <sub>2</sub>       | ~ 3.5 V               | 10 <sup>2</sup>            | -                             | -                     | -                              | -                        |
| MoS <sub>2</sub> -P123     | 3-4 V                 | >10 <sup>2</sup>           | -                             | 10 <sup>3</sup>       | -                              | -                        |
| MoS <sub>2</sub> -GO       | < 1.5 V               | 10 <sup>2</sup>            | -                             | -                     | -                              | -                        |
| ZIF-8-MoS <sub>2</sub>     | ~ 3.3 V               | 10 <sup>4</sup>            | -                             | 10 <sup>3</sup>       | -                              | -                        |

### 3.4 Flexible Ag/MoS<sub>2</sub>-PVA/Ag RRAM

#### 3.4.1 Electrical Characterization

I-V characterization of MoS<sub>2</sub>-PVA based memory devices was done by using Aglient B1500A Semiconductor Device Analyzer. Biased voltage was applied to the top Ag electrode while the bottom Ag electrode was grounded. Current compliance (C.C) value was set as 60 uA in the applied voltage sweep range of - 4 to + 4 volts. The typical characteristic semi-logarithmic I-V curve of resistive switching was observed in our memory device based on MoS<sub>2</sub>-PVA nanocomposite as displayed in Fig. 36(a). Current slightly kept increasing with increasing value of voltage while maintaining its HRS until the applied voltage reached to a threshold value  $V_{th}$  of  $\approx 3$  V. The low threshold voltage can be attributed to the high conductivity of Ag electrodes assisted by charged MoS<sub>2</sub> flakes. Current abruptly increased from  $9.6 \times 10^{-7}$  A to  $8.5 \times 10^{-5}$  A, resulting in a clear resistive switching from HRS to LRS. It can be deduced from this information that data can be written on this memory device at a voltage of  $\approx 3$  V. The tunable electrical resistance exist in the range of 22 k $\Omega$  to 3 M $\Omega$ .



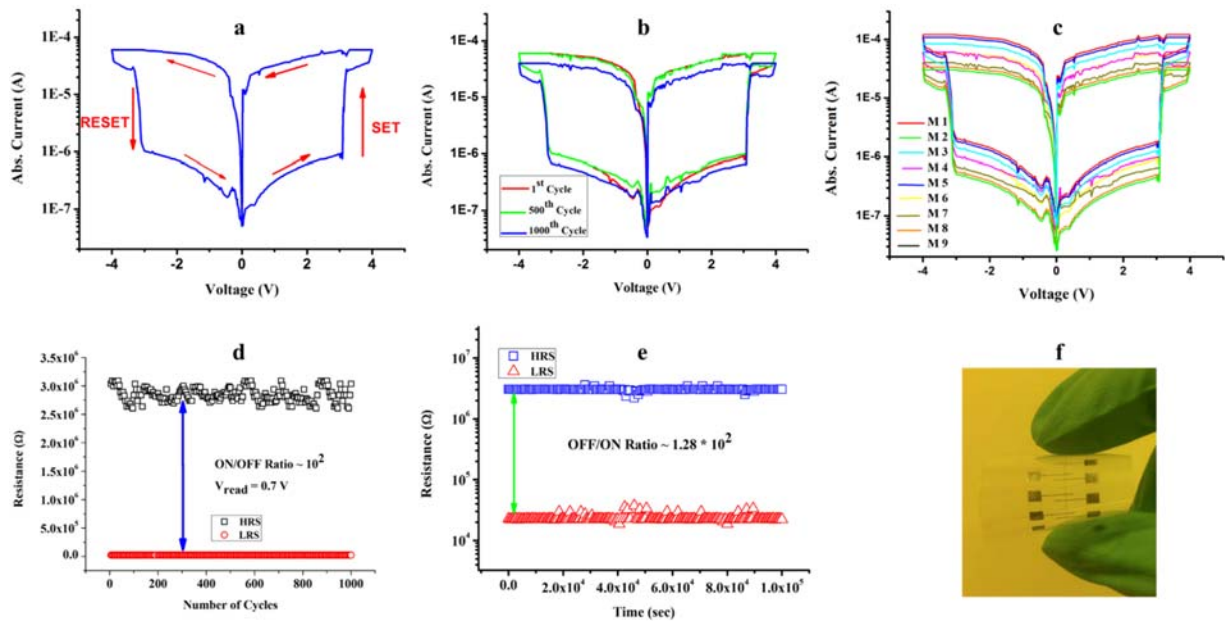


Figure 36. Electrical characterization of memory device a) Typical log I-V characteristic curve of a memristor showing bipolar resistive switching b) Endurance measurement showing excellent repeatability of 1<sup>st</sup>, 500<sup>th</sup>, and 1000<sup>th</sup> cycle c) Typical I-V curves showing the bipolar resistive switching effect in all the 9 memory cells of a 9 × 1 array labeled as M1-M9 respectively d) Endurance of HRS and LRS at a reading voltage of 0.7 volt showing remarkable stability e) Retention of HRS and LRS measured over a longer period of time without any noticeable deviation at 0.7 volts f) Optical Image of as fabricated memory device on a flexible PET substrate in bend condition

A decent off/on ratio at a  $V_{\text{READ}}$  of 0.7 V was recorded to be equal to  $1.28 \times 10^2$  that is enough to distinguish HRS from LRS. Figure 36(b) illustrates excellent endurance for both HRS and LRS when tested against 1000 voltage cycles as both resistive states showed extremely high stability. Our fabricated memory device comprise an array of nine memory cells. Characteristic logarithmic curve of all the nine memory cells was plotted against each other that showed significant repeatability as shown in Fig. 36(c). The highly symmetric nature of characteristic I-V curves was due to the selection of same Ag metal as the top and bottom electrode with a single uniform nanocomposite layer. Figure 36(d) illustrates the endurance of both resistive states i.e. HRS and LRS over 1000 voltage cycles displaying excellent repeatability. Once the bits were written and external power source

was removed, the device retained the stored data for over  $10^5$  sec without any noticeable decline in HRS or LRS, demonstrating its outstanding non-volatile memory behavior as shown in Fig. 36(e). Optical image of real device in bend state is shown in Fig. 36(f). Both resistive states i.e. HRS and LRS of MoS<sub>2</sub>-PVA based memory device are highly uniform as displayed in Fig. 37(a). Data can be stored and erased from the memory device by applying very small value of set and reset voltage. Cumulative plot of threshold voltage illustrates repeatable values for both  $V_{SET}$  and  $V_{RESET}$  as shown in Fig. 37(b).

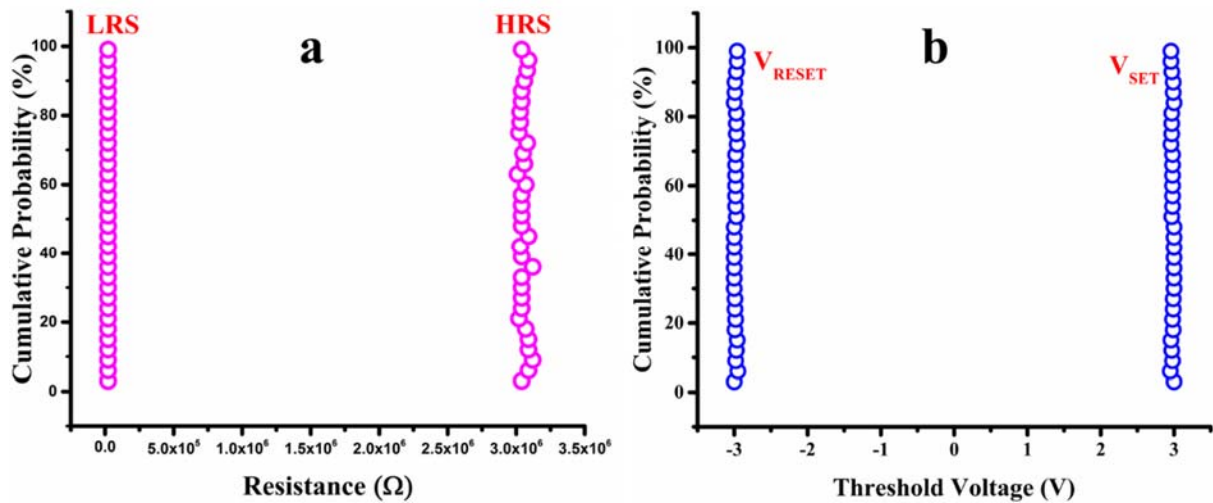


Figure 37. Cumulative Probability plot displaying highly stable and repeatable experimental values of both resistive states and threshold voltages for storing and removing data a) LRS and HRS b) Set and RESET voltage for writing and erasing data

### 3.4.2 Conduction Mechanism

In order to understand the conduction mechanism taking place in our device, model fitting studies for both HRS and LRS was carried out by taking logarithm of both current (y-axis) and voltage (x-axis) as shown in Fig. 38. This plot suggests that LRS is governed by ohmic conduction while HRS is governed by a typical trap controlled space charge limited current (TCSCLC) model as its plot can be confined by three restricted curves based on the slope values. These results are

comparable to already reported conduction mechanism for MoS<sub>2</sub>/PMMA functional thin film by Shinde et al. [48]. In region I (0–0.4 V), majority of charge carriers occur due to thermionic emission owing to lower value of applied bias voltage resulting in ohmic behavior (slope  $\approx 1$ ). These charge carriers mainly depend on the magnitude of externally applied electric field and electronic properties of functional materials [92,99]. As the applied electric field increases, electrons from the metallic electrodes gain enough energy to jump into the active nanocomposite layer of MoS<sub>2</sub>-PVA. Region II (0.4–3 V) signifies that as magnitude of applied voltage increase, traps present within the active layer of MoS<sub>2</sub>-PVA functional layer begin to partially fill with charge carriers hence slightly increasing the conductivity (slope  $\approx 3$ ) as suggested by Son et al. [92,99]. In region III (3–4 V), the magnitude of applied electric field is further increased and all the available unoccupied energy levels or traps are fully filled by the charge carriers resulting in an exponential increase in current as  $I \propto V^m$  (slope  $\approx 23$ ). This sharp increase in the current value can be associated with the exponential spread of trap states within a large bandgap between conduction and valence band of PVA polymer. On the other hand, initially the conduction band of MoS<sub>2</sub> flakes is partially filled with electrons. All the electrons present in the conduction band of MoS<sub>2</sub> have complete freedom of movement. As applied electric field is increased, electrons from the valence band of MoS<sub>2</sub> gain enough energy to jump into the conduction band and fill the unoccupied energy levels. The number of electrons in the conduction band of MoS<sub>2</sub> continue to increase with increasing applied bias voltage, hence resulting in higher conductivity of the memory device. This turns the device from HRS to LRS state. The conduction of charges in the LRS is governed by ohmic conduction ( $I \propto V$ ) owing to the value of linear fit line (slope  $\approx 1$ ) indicating the presence of good conductive channels. Choice of the metal contact is very critical for memory device as it determines the height of the energy barrier for the injected electrons from electrode

into functional thin film. It is a fact that lower the value of work function, lower will be the energy barrier heights, resulting in a large charge carrier flow from metal contacts into active thin film. Ag metal was chosen as the top and bottom electrode owing to its lower work function (4.26 eV) relative to the electron affinity of MoS<sub>2</sub> as compared to other metal electrodes like Pt (5.70 eV), Au (5.40 eV) and tungsten (5.1 eV) [100]. Several energy states are present within the band gaps of MoS<sub>2</sub> semiconductor and PVA polymer.

Primarily, the charge carriers are present in energy states with lower mobility keeping the device in HRS condition. In our memory device, energy states with lower energy levels are offered by exfoliated MoS<sub>2</sub> flakes. Electrons are trapped in the potential wells of MoS<sub>2</sub> due to its quantum confinement and lower energy levels. Conductivity of device begins to increase. As the magnitude of external applied electric field is further increased, its value reaches the threshold voltage ( $V_{th}$ ) at which all the traps with higher mobility are completely filled with charge carriers and the memory device switches to LRS. The huge bandgap offered by PVA polymer due to its dielectric property makes it extremely difficult for the trapped charge carriers to return to their original energy states without the aid of an external power source. This insulating property of PVA restricts the flow of trapped charge carriers back to their original energy states with lower mobility resulting in remarkably high retention time. In order to turn the device back to its original resistance state of HRS from LRS an external voltage supply of opposite polarity is applied. As a result, trapped charge carriers gain enough energy to overcome the huge energy barrier offered by PVA. This turns the device back to its original resistive state of HRS. In this fabricated device, the composition of MoS<sub>2</sub>-PVA nanocomposite along with the choice of top and bottom electrodes is yet to be optimized which will surely further increase the efficiency of this device.

Structure of our device can be attributed to an assembly of potential wells with different widths, depths and asymmetry's owing to the nanocomposite of n-type semiconducting MoS<sub>2</sub> flakes and dielectric PVA polymer as the functional materials. This difference is due to different magnitude of work function, HOMO and LUMO energy levels. Furthermore the states are localized in potential wells due to which movement of charge carriers takes place by hopping mechanism. Before the application of voltage sweep, charge carriers trapped in the potential wells are in Fermi level. Initially charges are present in lowest available energy levels where they have low mobility. On the application of electric field, charge carriers gain enough energy and bending of energy barriers takes place. These excited electrons begin to flow from lower energy states into traps with higher energy. This partially fulfills the traps and

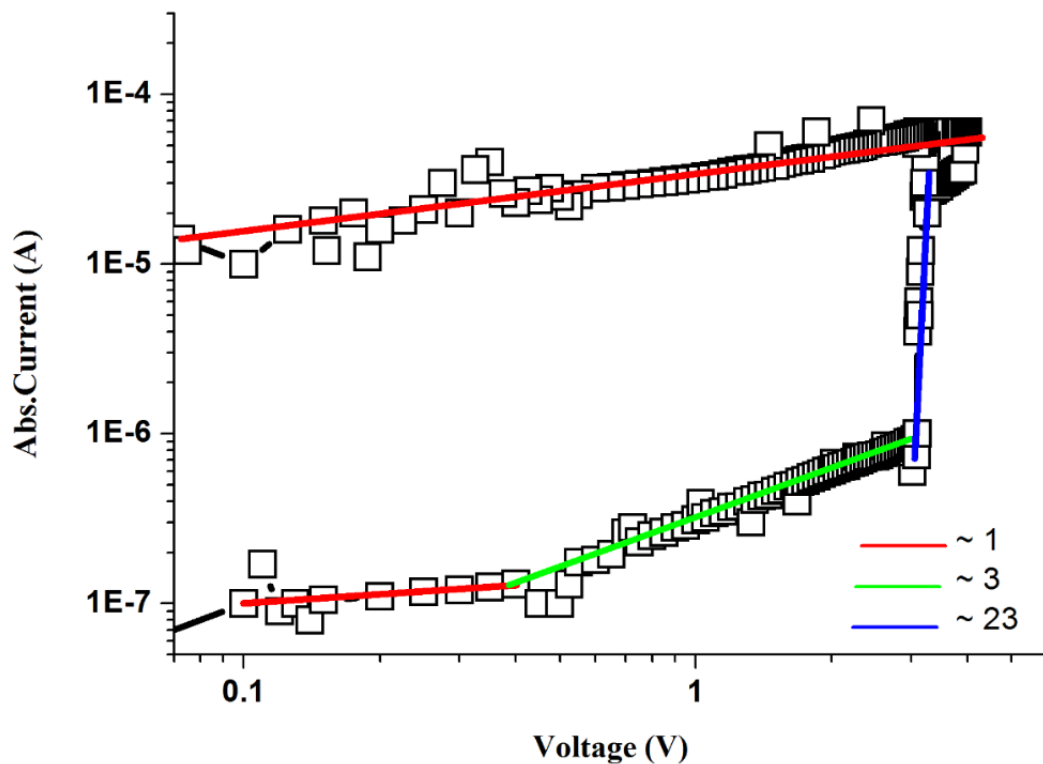


Figure 38. Double Logarithmic I-V curve showing the slopes for HRS and LRS with different values of slope. This plot can be divided into three distinguish regions as separated by the three different colors. In the red line region, ohmic conduction takes place as slope  $\approx 1$ . The green line is the Child's law region as the slope value  $\approx 3$ . The blue line shows the region of sharp current increase as slope  $\approx 23$  where the device switches from HRS to LRS.

### 3.4.3 Mechanical Characterization

As the device was fabricated on a flexible PET substrate therefore its mechanical robustness was examined against several bending cycles by squeezing the PET substrate in forward and backward direction. An in-house designed bending machine was used for repeatable bendability test at desired curvatures. The device showed excellent mechanical strength against 1500 bending cycles without any considerable change in both resistive states at a fixed bending diameter of 10 mm as no considerable difference in the bi-stable resistive states was observed in Fig. 39(a). Inset of Fig. 39(a) illustrates the optical image of as fabricated device without bending. The resistance of both HRS and LRS was plotted against decreasing value of bending diameter ranging from 50 mm to 2 mm. Figure 39(b) shows the endurance of both resistive states i.e. HRS and LRS against several bending diameters exhibiting negligible deviation owing to the remarkable mechanical strength of these devices. Inset of Fig. 39(b) illustrates the optical image of as fabricated memory device in bend state. However bending beyond 2 mm caused the disintegration of electrodes that ruptured the path of electron flow resulting in open circuit. The formation of micro and major cracks with increasing bending diameter are shown in Fig. 39(c–e). These bendability test shows that MoS<sub>2</sub>-PVA based memory device is remarkably suitable to be used in flexible electronics.

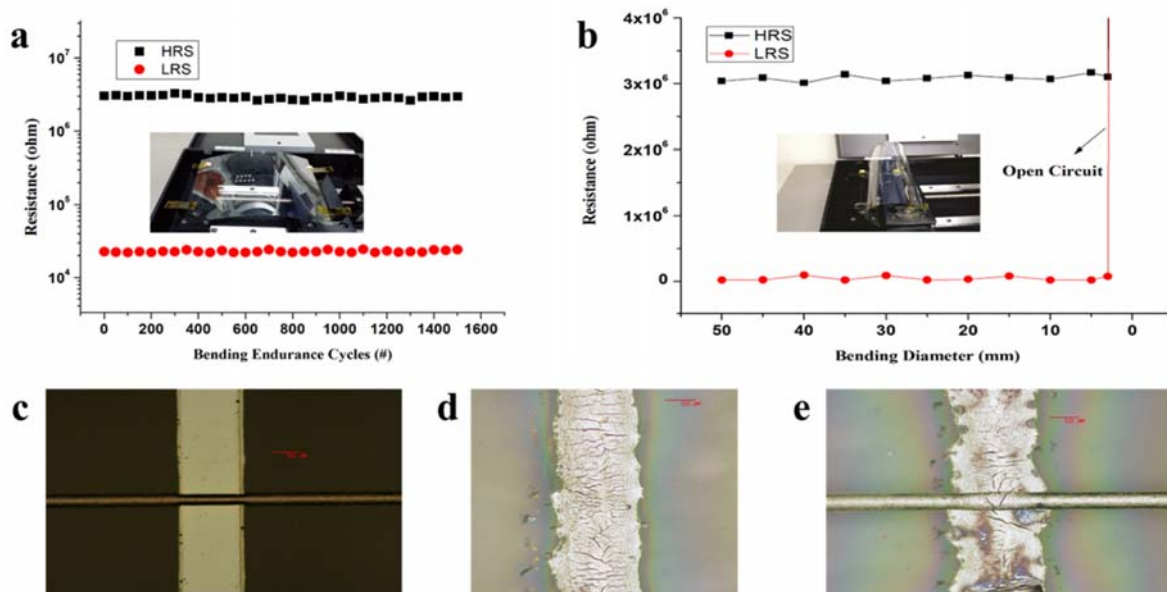


Figure 39. Bendability measurements by using the in-house prepared bending machine showing the remarkable flexible properties of as prepared resistive switching device a) Endurance curve showing HRS and LRS values for 1500 bending cycles at a fixed diameter value of 10 mm b) Endurance plot clearly showing very less deviation in HRS and LRS with changing values of bending diameters in the range of 30 mm to 2 mm. The device behaved like an open circuit at a bending diameter of 2 mm. Optical images of as top and bottom electrodes at different values of bending diameters c) Before bending d) Appearance of micro-cracks in bottom electrode e) Development of a major crack in the bottom electrode and completely broken top electrode at a bending diameter of 2 mm resulting in the open circuit of memory device

The nonvolatile memory device based on hybrid MoS<sub>2</sub>-PVA nanocomposite exhibited superior electrical and mechanical characteristics such as better off/on ratio, high retention time, lower current compliance, larger endurance, low operating voltage and remarkable mechanical robustness when compared with already reported resistive switching devices based on PVA nanocomposites with other materials. Electrical characteristics of already reported PVA based memory devices have been compared with our device in Table 15. Moreover, the electrical characteristics of already reported MoS<sub>2</sub> based memory devices have also been separately compared with MoS<sub>2</sub>-PVA based memory device reported in this work as shown in Table 16. Off/on ratio of MoS<sub>2</sub>-PVA nanocomposite is comparable to other already reported MoS<sub>2</sub> based memory devices, however retention of this device is significantly higher owing to the high

dielectric value of PVA which restricts the charge carriers to move back to their original energy states after the removal of external power supply. From Tables 15 and 16, it is noticeable that the results for mechanical robustness of either PVA or MoS<sub>2</sub> based nanocomposite memory devices by bending at various diameters and for several bending cycles have never been reported before this work.

Table 15. Comparison of MoS<sub>2</sub>-PVA nanocomposite based memristive device with already reported memory devices based on PVA nanocomposites. It is evident from the illustrated results that MoS<sub>2</sub> flakes play a vital role in improving the electrical properties of PVA based memory devices

| Active Layer Materials | Voltage Sweep | Off/On ratio       | Current Compliance | Endurance | Retention          | Mechanical Robustness | Bend-ability | Ref       |
|------------------------|---------------|--------------------|--------------------|-----------|--------------------|-----------------------|--------------|-----------|
| MoS <sub>2</sub> -PVA  | -4 to +4      | $1.28 \times 10^2$ | 60 $\mu$ A         | 1000      | $10^5$ s           | 1500 cycles           | 2 mm         | This work |
| PVA-PbS                | -30 to +30    | < 10               | 30 $\mu$ A         | -         | -                  | -                     | -            | [101]     |
| AgNW-PVA               | -10 to +10    | $\sim 10$          | 10 mA              | 160       | -                  | -                     | -            | [102]     |
| PEDOT:PSS-PVA          | -2 to +2      | $\sim 10^2$        | 100 mA             | -         | $36 \times 10^4$ s | -                     | -            | [1]       |
| GNF-PVA                | -7 to +2      | $\sim 10^2$        | 1 mA               | 100       | $1 \times 10^4$ s  | -                     | -            | [2]       |

Table 16. Comparison of MoS<sub>2</sub>-PVA nanocomposite based memristive device with already reported memory devices based on nanocomposites of MoS<sub>2</sub> semiconductor with other materials. It is evident from the illustrated results that PVA has enhanced the retention time and mechanical strength MoS<sub>2</sub> based memory device

| Active Layer Materials | Switching Voltage | Off/On Current Ratio   | Retention Time      | Endurance   | Bending Diameter | Mechanical Robustness | Ref       |
|------------------------|-------------------|------------------------|---------------------|-------------|------------------|-----------------------|-----------|
| MoS <sub>2</sub> :PVA  | 3 V               | $1.28 \times 10^2$     | $10^5$ s            | 1000 cycles | Up to 2 mm       | 1500 cycles           | This work |
| MoS <sub>2</sub> -GO   | < 1.5 V           | $\sim 10^2$            | -                   | -           | -                | -                     | [21]      |
| PVP-MoS <sub>2</sub>   | $\sim 3.5$ V      | $\sim 10^2$            | -                   | -           | -                | -                     | [51]      |
| MoS <sub>2</sub> -P123 | 3-4 V             | $\sim 5.5 \times 10^2$ | $4 \times 10^3$ s   | -           | -                | -                     | [20]      |
| ZIF-8/MoS <sub>2</sub> | $\sim 3.3$ V      | $\sim 7 \times 10^4$   | $1.5 \times 10^3$ s | -           | -                | -                     | [103]     |



## 4. Conclusions and Future work

### 4.1 Conclusions

In conclusion, we demonstrated extremely simple and cost effective flexible memory devices based on 2D materials and their nanocomposites by using all printed technology including reverse offset, EHDA, and RPC inkjet head printing systems. We proposed advanced optically transparent 2D nanocomposites of GQDs-hBN, MoS<sub>2</sub>QDs-hBN, MoS<sub>2</sub>-PVA and WS<sub>2</sub> flakes and deposited them over flexible PET substrates. ITO and Ag were used as the electrodes in each RRAM device. These 2D materials based RRAM devices displayed excellent performance in various essential aspects of resistive switching including switching ratio ( $\sim 10^3$ ), retention time ( $\sim 10^5$  s), write/erase cycling ( $\sim 1500$ ), and particularly mechanical endurance (2000 cycles). These promising results of flexible memory were obtained due to the supreme mechanical strength of 2D materials, large bandgap of hBN and quantum confinement effect of GQDs and MoS<sub>2</sub>QDs. A couple of devices were encapsulated by atomically thin layer of Al<sub>2</sub>O<sub>3</sub> by using ALD system to enhance its lifetime. The core switching mechanism in these four devices were deduced to be based on conductive filamentary and TCSCLC owing to the slope values of double logarithmic I-V curves and dependence of bistable resistive states on temperature and device size. This study provides a platform for exploring the unique characteristics of 2D materials and their applications in a flexible NVM device. These experimental results remarkably demonstrate the promising potential of 2D materials in defining the future of highly flexible and rewritable NVM devices.

### 4.2 Future work

The presented results broaden and deepen the understanding of memory phenomena in hybrid nanocomposites of 2D materials and polymers. In future, research work needs to be done on various aspects of these 2D materials and their nanocomposites owing to their unique and significant properties. Future directions include studying the effect of changing the thickness of these active layers, trying these 2D materials with several other available materials to form novel nanocomposites, optimizing the concentration of both materials blended in the 2D nanocomposite and developing a stretchable RRAM device instead of

only flexible. Furthermore, these 2D material based RRAM devices can be used in various applications such as logic operations, neuromorphic studies, oscillator circuits, filters, flexible memory devices, and chaotic systems.

## References

- [1] J. Huang, D. Ma, Electrical switching and memory behaviors in organic diodes based on polymer blend films treated by ultraviolet ozone, *Appl. Phys. Lett.* 105 (2014) 93303. doi:10.1063/1.4895122.
- [2] Y.-C. Lai, D.-Y. Wang, I.-S. Huang, Y.-T. Chen, Y.-H. Hsu, T.-Y. Lin, H.-F. Meng, T.-C. Chang, Y.-J. Yang, C.-C. Chen, F.-C. Hsu, Y.-F. Chen, Low operation voltage macromolecular composite memory assisted by graphene nanoflakes, *J. Mater. Chem. C* 1 (2013) 552–559. doi:10.1039/C2TC00010E.
- [3] M.M. Rehman, G.U. Siddiqui, J.Z. Gul, S.-W. Kim, J.H. Lim, K.H. Choi, Resistive Switching in All-Printed, Flexible and Hybrid MoS<sub>2</sub>-PVA Nanocomposite based Memristive Device Fabricated by Reverse Offset, *Sci. Rep.* 6 (2016) 36195. doi:10.1038/srep36195.
- [4] C. Lee, X. Wei, J.W. Kysar, J. Hone, Measurement of the Elastic Properties and Intrinsic Strength of Monolayer Graphene, *Science* (80-. ). 321 (2008) 385–388. doi:10.1126/science.1157996.
- [5] A.A. Balandin, S. Ghosh, W. Bao, I. Calizo, D. Teweldebrhan, F. Miao, C.N. Lau, Superior Thermal Conductivity of Single-Layer Graphene, *Nano Lett.* 8 (2008) 902–907. doi:10.1021/nl0731872.
- [6] V. V. Ilyasov, I.G. Popova, I. V. Ershov, N.D. Chien, N.N. Hieu, C. V. Nguyen, First principles study of structural, electronic and magnetic properties of graphene adsorbed on the O-terminated MnO(111) surface, *Diam. Relat. Mater.* 74 (2017) 31–40. doi:10.1016/j.diamond.2017.02.001.
- [7] A. Jafari, M. Ghoranneviss, M. Gholami, A. Salar Elahi, A. Kavosi ghafi, The Effects of Percent and Position of Nitrogen Atoms on Electronic and Thermoelectric Properties of Graphene Nanoribbons, *J. Inorg. Organomet. Polym. Mater.* 26 (2016) 1095–1100. doi:10.1007/s10904-016-0430-7.
- [8] A.C. Ferrari, D.M. Basko, Raman spectroscopy as a versatile tool for studying the properties of graphene, *Nat. Nanotechnol.* 8 (2013) 235–246. doi:10.1038/nnano.2013.46.
- [9] H.-Q. Lin, T. Ma, Z. Huang, Quantum Monte Carlo study of magnetic and superconducting properties of graphene, *Math. Methods Appl. Sci.* 38 (2015) 4487–4494. doi:10.1002/mma.2851.
- [10] X. Yan, X. Cui, L. Li, Synthesis of Large, Stable Colloidal Graphene Quantum Dots with Tunable Size, *J. Am. Chem. Soc.* 132 (2010) 5944–5945. doi:10.1021/ja1009376.
- [11] X. Li, M. Rui, J. Song, Z. Shen, H. Zeng, Carbon and Graphene Quantum Dots for Optoelectronic and Energy Devices: A Review, *Adv. Funct. Mater.* 25 (2015) 4929–4947. doi:10.1002/adfm.201501250.
- [12] L. Tang, R. Ji, X. Li, G. Bai, C.P. Liu, J. Hao, J. Lin, H. Jiang, K.S. Teng, Z. Yang, S.P. Lau, Deep Ultraviolet to Near-Infrared Emission and Photoresponse in Layered N-Doped Graphene Quantum Dots, *ACS Nano* 8 (2014) 6312–6320. doi:10.1021/nn501796r.
- [13] Y. Zhu, X. Ji, C. Pan, Q. Sun, W. Song, L. Fang, Q. Chen, C.E. Banks, A carbon quantum dot decorated RuO<sub>2</sub> network: outstanding supercapacitances under ultrafast charge and discharge, *Energy Environ. Sci.* 6 (2013) 3665. doi:10.1039/c3ee41776j.
- [14] V. Gupta, N. Chaudhary, R. Srivastava, G.D. Sharma, R. Bhardwaj, S. Chand, Luminescent Graphene Quantum Dots for Organic Photovoltaic Devices, *J. Am. Chem. Soc.* 133 (2011) 9960–9963. doi:10.1021/ja2036749.
- [15] A. Pezeshki, S.H. Hosseini Shokouh, S.R.A. Raza, J.S. Kim, S.-W. Min, I. Shackery, S.C. Jun, S. Im, Top and back gate molybdenum disulfide transistors coupled for logic and photo-inverter operation, *J.*

- Mater. Chem. C. 2 (2014) 8023–8028. doi:10.1039/C4TC01673D.
- [16] J. Du, Q. Wang, G. Jiang, C. Xu, C. Zhao, Y. Xiang, Y. Chen, S. Wen, H. Zhang, Ytterbium-doped fiber laser passively mode locked by few-layer Molybdenum Disulfide (MoS<sub>2</sub>) saturable absorber functioned with evanescent field interaction, *Sci. Rep.* 4 (2015) 6346. doi:10.1038/srep06346.
- [17] J.-M. Yun, Y.-J. Noh, J.-S. Yeo, Y.-J. Go, S.-I. Na, H.-G. Jeong, J. Kim, S. Lee, S.-S. Kim, H.Y. Koo, T.-W. Kim, D.-Y. Kim, Efficient work-function engineering of solution-processed MoS<sub>2</sub> thin-films for novel hole and electron transport layers leading to high-performance polymer solar cells, *J. Mater. Chem. C.* 1 (2013) 3777. doi:10.1039/c3tc30504j.
- [18] Y. Li, C.-Y. Xu, J.-Y. Wang, L. Zhen, Photodiode-Like Behavior and Excellent Photoresponse of Vertical Si/Monolayer MoS<sub>2</sub> Heterostructures, *Sci. Rep.* 4 (2015) 7186. doi:10.1038/srep07186.
- [19] X. Liu, J. Hu, C. Yue, N. Della Fera, Y. Ling, Z. Mao, J. Wei, High Performance Field-Effect Transistor Based on Multilayer Tungsten Disulfide, *ACS Nano.* 8 (2014) 10396–10402. doi:10.1021/nn505253p.
- [20] C. Tan, X. Qi, Z. Liu, F. Zhao, H. Li, X. Huang, L. Shi, B. Zheng, X. Zhang, L. Xie, Z. Tang, W. Huang, H. Zhang, Self-Assembled Chiral Nanofibers from Ultrathin Low-Dimensional Nanomaterials, *J. Am. Chem. Soc.* 137 (2015) 1565–1571. doi:10.1021/ja511471b.
- [21] Z. Yin, Z. Zeng, J. Liu, Q. He, P. Chen, H. Zhang, Memory Devices Using a Mixture of MoS<sub>2</sub> and Graphene Oxide as the Active Layer, *Small.* 9 (2013) 727–731. doi:10.1002/smll.201201940.
- [22] K.F. Mak, C. Lee, J. Hone, J. Shan, T.F. Heinz, Atomically Thin  $\text{MoS}_2$ : A New Direct-Gap Semiconductor, *Phys. Rev. Lett.* 105 (2010) 136805. doi:10.1103/PhysRevLett.105.136805.
- [23] B. Radisavljevic, A. Radenovic, J. Brivio, V. Giacometti, A. Kis, Single-layer MoS<sub>2</sub> transistors, *Nat. Nanotechnol.* 6 (2011) 147–150. doi:10.1038/nnano.2010.279.
- [24] K.-G. Zhou, N.-N. Mao, H.-X. Wang, Y. Peng, H.-L. Zhang, A Mixed-Solvent Strategy for Efficient Exfoliation of Inorganic Graphene Analogues, *Angew. Chemie Int. Ed.* 50 (2011) 10839–10842. doi:10.1002/anie.201105364.
- [25] W. Gu, Y. Yan, C. Zhang, C. Ding, Y. Xian, One-Step Synthesis of Water-Soluble MoS<sub>2</sub> Quantum Dots via a Hydrothermal Method as a Fluorescent Probe for Hyaluronidase Detection, *ACS Appl. Mater. Interfaces.* 8 (2016) 11272–11279. doi:10.1021/acsami.6b01166.
- [26] X. Wang, H. Feng, Y. Wu, L. Jiao, Controlled Synthesis of Highly Crystalline MoS<sub>2</sub> Flakes by Chemical Vapor Deposition, *J. Am. Chem. Soc.* 135 (2013) 5304–5307. doi:10.1021/ja4013485.
- [27] R. Wei, H. Zhang, X. Tian, T. Qiao, Z. Hu, Z. Chen, X. He, Y. Yu, J. Qiu, MoS<sub>2</sub> nanoflowers as high performance saturable absorbers for an all-fiber passively Q-switched erbium-doped fiber laser, *Nanoscale.* 8 (2016) 7704–7710. doi:10.1039/C5NR08457A.
- [28] M. Acerce, D. Voiry, M. Chhowalla, Metallic 1T phase MoS<sub>2</sub> nanosheets as supercapacitor electrode materials, *Nat. Nanotechnol.* 10 (2015) 313–318. doi:10.1038/nnano.2015.40.
- [29] Y. Huang, J. Guo, Y. Kang, Y. Ai, C.M. Li, Two dimensional atomically thin MoS<sub>2</sub> nanosheets and their sensing applications, *Nanoscale.* 7 (2015) 19358–19376. doi:10.1039/C5NR06144J.
- [30] Z. Yin, H. Li, H. Li, L. Jiang, Y. Shi, Y. Sun, G. Lu, Q. Zhang, X. Chen, H. Zhang, Single-Layer MoS<sub>2</sub>

- Phototransistors, *ACS Nano*. 6 (2012) 74–80. doi:10.1021/nn2024557.
- [31] H.-U. Kim, H. Kim, C. Ahn, A. Kulkarni, M. Jeon, G.Y. Yeom, M.-H. Lee, T. Kim, In situ synthesis of MoS<sub>2</sub> on a polymer based gold electrode platform and its application in electrochemical biosensing, *RSC Adv*. 5 (2015) 10134–10138. doi:10.1039/C4RA14839H.
- [32] M.-L. Tsai, S.-H. Su, J.-K. Chang, D.-S. Tsai, C.-H. Chen, C.-I. Wu, L.-J. Li, L.-J. Chen, J.-H. He, Monolayer MoS<sub>2</sub> Heterojunction Solar Cells, *ACS Nano*. 8 (2014) 8317–8322. doi:10.1021/nn502776h.
- [33] J. Xiao, X. Wang, X.-Q. Yang, S. Xun, G. Liu, P.K. Koech, J. Liu, J.P. Lemmon, Electrochemically Induced High Capacity Displacement Reaction of PEO/MoS<sub>2</sub>/Graphene Nanocomposites with Lithium, *Adv. Funct. Mater.* 21 (2011) 2840–2846. doi:10.1002/adfm.201002752.
- [34] X. Song, J. Hu, H. Zeng, Two-dimensional semiconductors: recent progress and future perspectives, *J. Mater. Chem. C*. 1 (2013) 2952. doi:10.1039/c3tc00710c.
- [35] P.C. Ooi, K.C. Aw, W. Gao, K.A. Razak, An optically transparent and flexible memory with embedded gold nanoparticles in a polymethylsilsesquioxane dielectric, *Thin Solid Films*. 544 (2013) 597–601. doi:10.1016/j.tsf.2012.12.059.
- [36] P.C. Ooi, F. Li, C.P. Veeramalai, T. Guo, Transparent and flexible nonvolatile memory using poly(methylsilsesquioxane) dielectric embedded with cadmium selenide quantum dots, *Jpn. J. Appl. Phys.* 53 (2014) 125001. doi:10.7567/JJAP.53.125001.
- [37] J. Lin, P.C. Ooi, F. Li, T. Guo, T.W. Kim, Solution-Processed, Flexible, and Transparent Non-Volatile Memory With Embedded Graphene Quantum Dots in Polymethylsilsesquioxane Layers, *IEEE Electron Device Lett.* 36 (2015) 1212–1214. doi:10.1109/LED.2015.2480119.
- [38] F. Li, L. Kou, W. Chen, C. Wu, T. Guo, Enhancing the short-circuit current and power conversion efficiency of polymer solar cells with graphene quantum dots derived from double-walled carbon nanotubes, *NPG Asia Mater.* 5 (2013) e60. doi:10.1038/am.2013.38.
- [39] J. Shen, Y. Zhu, X. Yang, C. Li, Graphene quantum dots: emergent nanolights for bioimaging, sensors, catalysis and photovoltaic devices, *Chem. Commun.* 48 (2012) 3686. doi:10.1039/c2cc00110a.
- [40] P.C. Ooi, J. Lin, T.W. Kim, F. Li, Tristable switching of the electrical conductivity through graphene quantum dots sandwiched in multi-stacked poly(methyl methacrylate) layers, *Org. Electron.* 38 (2016) 379–383. doi:10.1016/j.orgel.2016.09.010.
- [41] D.H. Kim, D. Lim, The electrical and valley properties of monolayer MoSe<sub>2</sub>, *Curr. Appl. Phys.* 17 (2017) 321–325. doi:10.1016/j.cap.2016.10.006.
- [42] J. Shang, G. Liu, H. Yang, X. Zhu, X. Chen, H. Tan, B. Hu, L. Pan, W. Xue, R.-W. Li, Thermally Stable Transparent Resistive Random Access Memory based on All-Oxide Heterostructures, *Adv. Funct. Mater.* 24 (2014) 2171–2179. doi:10.1002/adfm.201303274.
- [43] K.S. Karimov, Z. Ahmad, F. Touati, M. Mahroof-Tahir, M. Muqet Rehman, S. Zameer Abbas, Surface-type nonvolatile electric memory elements based on organic-on-organic CuPc-H<sub>2</sub>Pc heterojunction, *Chinese Phys. B*. 24 (2015) 116102. doi:10.1088/1674-1056/24/11/116102.
- [44] Y.-C. Lai, Y.-X. Wang, Y.-C. Huang, T.-Y. Lin, Y.-P. Hsieh, Y.-J. Yang, Y.-F. Chen, Rewritable, Moldable, and Flexible Sticker-Type Organic Memory on Arbitrary Substrates, *Adv. Funct. Mater.* 24 (2014)

- 1430–1438. doi:10.1002/adfm.201302246.
- [45] B. Cheng, J. Zhao, L. Xiao, Q. Cai, R. Guo, Y. Xiao, S. Lei, PMMA interlayer-modulated memory effects by space charge polarization in resistive switching based on CuSCN-nanopyramids/ZnO-nanorods p-n heterojunction, *Sci. Rep.* 5 (2016) 17859. doi:10.1038/srep17859.
- [46] G.U. Siddiqui, M.M. Rehman, K.H. Choi, Enhanced resistive switching in all-printed, hybrid and flexible memory device based on perovskite ZnSnO<sub>3</sub> via PVOH polymer, *Polymer (Guildf)*. 100 (2016) 102–110. doi:10.1016/j.polymer.2016.07.081.
- [47] P. Cheng, K. Sun, Y.H. Hu, Memristive Behavior and Ideal Memristor of 1T Phase MoS<sub>2</sub> Nanosheets, *Nano Lett.* 16 (2016) 572–576. doi:10.1021/acs.nanolett.5b04260.
- [48] S.M. Shinde, G. Kalita, M. Tanemura, Fabrication of poly(methyl methacrylate)-MoS<sub>2</sub>/graphene heterostructure for memory device application, *J. Appl. Phys.* 116 (2014) 214306. doi:10.1063/1.4903552.
- [49] X.-Y. Xu, Z.-Y. Yin, C.-X. Xu, J. Dai, J.-G. Hu, Resistive switching memories in MoS<sub>2</sub> nanosphere assemblies, *Appl. Phys. Lett.* 104 (2014) 33504. doi:10.1063/1.4862755.
- [50] V.K. Sangwan, D. Jariwala, I.S. Kim, K.-S. Chen, T.J. Marks, L.J. Lauhon, M.C. Hersam, Gate-tunable memristive phenomena mediated by grain boundaries in single-layer MoS<sub>2</sub>, *Nat. Nanotechnol.* 10 (2015) 403–406. doi:10.1038/nnano.2015.56.
- [51] J. Liu, Z. Zeng, X. Cao, G. Lu, L.-H. Wang, Q.-L. Fan, W. Huang, H. Zhang, Preparation of MoS<sub>2</sub>-Polyvinylpyrrolidone Nanocomposites for Flexible Nonvolatile Rewritable Memory Devices with Reduced Graphene Oxide Electrodes, *Small*. 8 (2012) 3517–3522. doi:10.1002/sml.201200999.
- [52] K. Oh, W. Jeon, S.-S. Lee, One-Dimensional TiO<sub>2</sub>@Ag Nanoarchitectures with Interface-Mediated Implementation of Resistance-Switching Behavior in Polymer Nanocomposites, *ACS Appl. Mater. Interfaces*. 4 (2012) 5727–5731. doi:10.1021/am301362f.
- [53] D. Qiu, D.U. Lee, K.S. Lee, S.W. Pak, E.K. Kim, Toward negligible charge loss in charge injection memories based on vertically integrated 2D heterostructures, *Nano Res.* 9 (2016) 2319–2326. doi:10.1007/s12274-016-1118-6.
- [54] K. Ali, J. Ali, S.M. Mehdi, K.-H. Choi, Y.J. An, Rapid fabrication of Al<sub>2</sub>O<sub>3</sub> encapsulations for organic electronic devices, *Appl. Surf. Sci.* 353 (2015) 1186–1194. doi:10.1016/j.apsusc.2015.07.032.
- [55] Y.-M. Choi, E. Lee, T.-M. Lee, Mechanism of reverse-offset printing, *J. Micromechanics Microengineering*. 25 (2015) 75019. doi:10.1088/0960-1317/25/7/075019.
- [56] K.L. Mendoza, A. Ortega, N.S. Kim, Optimization of UV LED-Curable Ink for Reverse-Offset Roll-to-Plate (RO-R2P) Printing, *J. Electron. Mater.* 44 (2015) 784–791. doi:10.1007/s11664-014-3506-6.
- [57] G. Siddiqui, J. Ali, Y.-H. Doh, K.H. Choi, Fabrication of zinc stannate based all-printed resistive switching device, *Mater. Lett.* 166 (2016) 311–316. doi:10.1016/j.matlet.2015.12.045.
- [58] K.H. Choi, G.U. Siddiqui, B. Yang, M. Mustafa, Synthesis of ZnSnO<sub>3</sub> nanocubes and thin film fabrication of (ZnSnO<sub>3</sub>/PMMA) composite through electrospray deposition, *J. Mater. Sci. Mater. Electron.* 26 (2015) 5690–5696. doi:10.1007/s10854-015-3121-1.
- [59] J. Ali, G.U. Siddiqui, K.H. Choi, Y. Jang, K. Lee, Fabrication of blue luminescent MoS<sub>2</sub> quantum dots by wet grinding assisted co-solvent sonication, *J. Lumin.* 169 (2016) 342–347.

doi:10.1016/j.jlumin.2015.09.028.

- [60] G.U. Siddiqui, M.M. Rehman, Y.-J. Yang, K.H. Choi, A two-dimensional hexagonal boron nitride/polymer nanocomposite for flexible resistive switching devices, *J. Mater. Chem. C* 5 (2017) 862–871. doi:10.1039/C6TC04345C.
- [61] Y. Xue, Q. Liu, G. He, K. Xu, L. Jiang, X. Hu, J. Hu, Excellent electrical conductivity of the exfoliated and fluorinated hexagonal boron nitride nanosheets, *Nanoscale Res. Lett.* 8 (2013) 49. doi:10.1186/1556-276X-8-49.
- [62] J. Ali, G. Siddiqui, Y.J. Yang, K.T. Lee, K. Um, K.H. Choi, Direct synthesis of graphene quantum dots from multilayer graphene flakes through grinding assisted co-solvent ultrasonication for all-printed resistive switching arrays, *RSC Adv.* 6 (2016) 5068–5078. doi:10.1039/C5RA21699K.
- [63] C. Rice, R.J. Young, R. Zan, U. Bangert, D. Wolverson, T. Georgiou, R. Jalil, K.S. Novoselov, Raman-scattering measurements and first-principles calculations of strain-induced phonon shifts in monolayer MoS<sub>2</sub>, *Phys. Rev. B* 87 (2013) 81307. doi:10.1103/PhysRevB.87.081307.
- [64] Y. Wang, C. Cong, C. Qiu, T. Yu, Raman Spectroscopy Study of Lattice Vibration and Crystallographic Orientation of Monolayer MoS<sub>2</sub> under Uniaxial Strain, *Small* 9 (2013) 2857–2861. doi:10.1002/sml.201202876.
- [65] P. Hajiyev, C. Cong, C. Qiu, T. Yu, Contrast and Raman spectroscopy study of single- and few-layered charge density wave material: 2H-TaSe<sub>2</sub>, *Sci. Rep.* 3 (2013) 2593. doi:10.1038/srep02593.
- [66] H. Zeng, G.-B. Liu, J. Dai, Y. Yan, B. Zhu, R. He, L. Xie, S. Xu, X. Chen, W. Yao, X. Cui, Optical signature of symmetry variations and spin-valley coupling in atomically thin tungsten dichalcogenides, *Sci. Rep.* 3 (2013) 1608. doi:10.1038/srep01608.
- [67] X. Li, S. Sundaram, Y. El Gmili, T. Ayari, R. Puybaret, G. Patriarche, P.L. Voss, J.P. Salvestrini, A. Ougazzaden, Large-Area Two-Dimensional Layered Hexagonal Boron Nitride Grown on Sapphire by Metalorganic Vapor Phase Epitaxy, *Cryst. Growth Des.* 16 (2016) 3409–3415. doi:10.1021/acs.cgd.6b00398.
- [68] G. Lu, T. Wu, Q. Yuan, H. Wang, H. Wang, F. Ding, X. Xie, M. Jiang, Synthesis of large single-crystal hexagonal boron nitride grains on Cu–Ni alloy, *Nat. Commun.* 6 (2015) 6160. doi:10.1038/ncomms7160.
- [69] F. Zhang, W. Yang, A. Pang, Z. Wu, H. Qi, J. Yao, Z. Fan, J. Shao, Annealing effects on the optical and structural properties of Al<sub>2</sub>O<sub>3</sub>/SiO<sub>2</sub> films as UV antireflection coatings on 4H-SiC substrates, *Appl. Surf. Sci.* 254 (2008) 6410–6415. doi:10.1016/j.apsusc.2008.04.015.
- [70] J. Park, N. Choudhary, J. Smith, G. Lee, M. Kim, W. Choi, Thickness modulated MoS<sub>2</sub> grown by chemical vapor deposition for transparent and flexible electronic devices, *Appl. Phys. Lett.* 106 (2015) 12104. doi:10.1063/1.4905476.
- [71] J.-Y. Wu, M.-N. Lin, L.-D. Wang, T. Zhang, Photoluminescence of MoS<sub>2</sub> Prepared by Effective Grinding-Assisted Sonication Exfoliation, *J. Nanomater.* 2014 (2014) 1–7. doi:10.1155/2014/852735.
- [72] M.M. Rehman, G.U. Siddiqui, S. Kim, K.H. Choi, Resistive switching effect in the planar structure of all-printed, flexible and rewritable memory device based on advanced 2D nanocomposite of

- graphene quantum dots and white graphene flakes, *J. Phys. D. Appl. Phys.* 50 (2017) 335104. doi:10.1088/1361-6463/aa798a.
- [73] G.H. Kim, K.M. Kim, J.Y. Seok, H.J. Lee, D.-Y. Cho, J.H. Han, C.S. Hwang, A theoretical model for Schottky diodes for excluding the sneak current in cross bar array resistive memory, *Nanotechnology*. 21 (2010) 385202. doi:10.1088/0957-4484/21/38/385202.
- [74] M.-J. Lee, S.I. Kim, C.B. Lee, H. Yin, S.-E. Ahn, B.S. Kang, K.H. Kim, J.C. Park, C.J. Kim, I. Song, S.W. Kim, G. Stefanovich, J.H. Lee, S.J. Chung, Y.H. Kim, Y. Park, Low-Temperature-Grown Transition Metal Oxide Based Storage Materials and Oxide Transistors for High-Density Non-volatile Memory, *Adv. Funct. Mater.* 19 (2009) 1587–1593. doi:10.1002/adfm.200801032.
- [75] M.M. Rehman, B.-S. Yang, Y.-J. Yang, K.S. Karimov, K.H. Choi, Effect of device structure on the resistive switching characteristics of organic polymers fabricated through all printed technology, *Curr. Appl. Phys.* 17 (2017) 533–540. doi:10.1016/j.cap.2017.01.023.
- [76] N.M. Muhammad, A.M. Naeem, N. Duraisamy, D.-S. Kim, K.-H. Choi, Fabrication of high quality zinc-oxide layers through electrohydrodynamic atomization, *Thin Solid Films*. 520 (2012) 1751–1756. doi:10.1016/j.tsf.2011.08.065.
- [77] A. Ali, K. Ali, K.-R. Kwon, M.T. Hyun, K.H. Choi, Electrohydrodynamic atomization approach to graphene/zinc oxide film fabrication for application in electronic devices, *J. Mater. Sci. Mater. Electron*. 25 (2014) 1097–1104. doi:10.1007/s10854-013-1693-1.
- [78] M. Zubair, M. Mustafa, K. Lee, C. Yoon, Y.H. Doh, K.H. Choi, Fabrication of CdSe/ZnS quantum dots thin film by electrohydrodynamics atomization technique for solution based flexible hybrid OLED application, *Chem. Eng. J.* 253 (2014) 325–331. doi:10.1016/j.cej.2014.05.067.
- [79] A. Thakre, H. Borkar, B.P. Singh, A. Kumar, Electroforming free high resistance resistive switching of graphene oxide modified polar-PVDF, *RSC Adv.* 5 (2015) 57406–57413. doi:10.1039/C5RA08663A.
- [80] B. Sun, L. Wei, H. Li, X. Jia, J. Wu, P. Chen, The DNA strand assisted conductive filament mechanism for improved resistive switching memory, *J. Mater. Chem. C*. 3 (2015) 12149–12155. doi:10.1039/C5TC02732B.
- [81] X. He, J. Zhang, W. Wang, W. Xuan, X. Wang, Q. Zhang, C.G. Smith, J. Luo, Transient Resistive Switching Devices Made from Egg Albumen Dielectrics and Dissolvable Electrodes, *ACS Appl. Mater. Interfaces*. 8 (2016) 10954–10960. doi:10.1021/acsami.5b10414.
- [82] K. Park, J.-S. Lee, Reliable resistive switching memory based on oxygen-vacancy-controlled bilayer structures, *RSC Adv.* 6 (2016) 21736–21741. doi:10.1039/C6RA00798H.
- [83] F. Pan, S. Gao, C. Chen, C. Song, F. Zeng, Recent progress in resistive random access memories: Materials, switching mechanisms, and performance, *Mater. Sci. Eng. R Reports*. 83 (2014) 1–59. doi:10.1016/j.mser.2014.06.002.
- [84] S. Bhattacharjee, P.K. Sarkar, N. Roy, A. Roy, Improvement of reliability of polymer nanocomposite based transparent memory device by oxygen vacancy rich ZnO nanorods, *Microelectron. Eng.* 164 (2016) 53–58. doi:10.1016/j.mee.2016.04.027.
- [85] R. Chen, C. Lin, H. Yu, Y. Tang, C. Song, L. Yuwen, H. Li, X. Xie, L. Wang, W. Huang, Templating C 60 on MoS<sub>2</sub> Nanosheets for 2D Hybrid van der Waals p – n Nanoheterojunctions, *Chem. Mater.* 28



- (2016) 4300–4306. doi:10.1021/acs.chemmater.6b01115.
- [86] H. Lv, X. Xu, P. Sun, H. Liu, Q. Luo, Q. Liu, W. Banerjee, H. Sun, S. Long, L. Li, M. Liu, Atomic View of Filament Growth in Electrochemical Memristive Elements, *Sci. Rep.* 5 (2015) 13311. doi:10.1038/srep13311.
- [87] E. Yoo, M. Lyu, J.-H. Yun, C. Kang, Y. Choi, L. Wang, Bifunctional resistive switching behavior in an organolead halide perovskite based  $\text{Ag}/\text{CH}_3\text{NH}_3\text{Pb}_{1-x}\text{Cl}_x/\text{FTO}$  structure, *J. Mater. Chem. C.* 4 (2016) 7824–7830. doi:10.1039/C6TC02503J.
- [88] A. Younis, D. Chu, S. Li, Evidence of Filamentary Switching in Oxide-based Memory Devices via Weak Programming and Retention Failure Analysis, *Sci. Rep.* 5 (2015) 13599. doi:10.1038/srep13599.
- [89] U. Celano, L. Goux, A. Belmonte, K. Opsomer, A. Franquet, A. Schulze, C. Detavernier, O. Richard, H. Bender, M. Jurczak, W. Vandervorst, Three-Dimensional Observation of the Conductive Filament in Nanoscaled Resistive Memory Devices, *Nano Lett.* 14 (2014) 2401–2406. doi:10.1021/nl500049g.
- [90] B. Zhang, M. Fraenkl, J.M. Macak, T. Wagner, Ag filament and surface particle formation in Ag doped  $\text{AsS}_2$  thin film, *Mater. Lett.* 163 (2016) 4–7. doi:10.1016/j.matlet.2015.08.131.
- [91] W. Hu, N. Qin, G. Wu, Y. Lin, S. Li, D. Bao, Opportunity of Spinel Ferrite Materials in Nonvolatile Memory Device Applications Based on Their Resistive Switching Performances, *J. Am. Chem. Soc.* 134 (2012) 14658–14661. doi:10.1021/ja305681n.
- [92] S.K. Pradhan, B. Xiao, S. Mishra, A. Killam, A.K. Pradhan, Resistive switching behavior of reduced graphene oxide memory cells for low power nonvolatile device application, *Sci. Rep.* 6 (2016) 26763. doi:10.1038/srep26763.
- [93] J. Zhang, Q. Zhang, H. Yang, H. Wu, J. Zhou, L. Hu, Bipolar resistive switching properties of AlN films deposited by plasma-enhanced atomic layer deposition, *Appl. Surf. Sci.* 315 (2014) 110–115. doi:10.1016/j.apsusc.2014.07.117.
- [94] X. Zhu, W. Su, Y. Liu, B. Hu, L. Pan, W. Lu, J. Zhang, R.-W. Li, Observation of Conductance Quantization in Oxide-Based Resistive Switching Memory, *Adv. Mater.* 24 (2012) 3941–3946. doi:10.1002/adma.201201506.
- [95] Y. Cui, H. Peng, S. Wu, R. Wang, T. Wu, Complementary Charge Trapping and Ionic Migration in Resistive Switching of Rare-Earth Manganite  $\text{TbMnO}_3$ , *ACS Appl. Mater. Interfaces.* 5 (2013) 1213–1217. doi:10.1021/am301769f.
- [96] S. Gao, C. Song, C. Chen, F. Zeng, F. Pan, Dynamic Processes of Resistive Switching in Metallic Filament-Based Organic Memory Devices, *J. Phys. Chem. C.* 116 (2012) 17955–17959. doi:10.1021/jp305482c.
- [97] S.Z. Butler, S.M. Hollen, L. Cao, Y. Cui, J.A. Gupta, H.R. Gutiérrez, T.F. Heinz, S.S. Hong, J. Huang, A.F. Ismach, E. Johnston-Halperin, M. Kuno, V. V. Plashnitsa, R.D. Robinson, R.S. Ruoff, S. Salahuddin, J. Shan, L. Shi, M.G. Spencer, M. Terrones, W. Windl, J.E. Goldberger, Progress, Challenges, and Opportunities in Two-Dimensional Materials Beyond Graphene, *ACS Nano.* 7 (2013) 2898–2926. doi:10.1021/nn400280c.
- [98] D. Akinwande, N. Petrone, J. Hone, Two-dimensional flexible nanoelectronics, *Nat. Commun.* 5 (2014) 5678. doi:10.1038/ncomms6678.

- [99] Y.J. Huang, S.C. Chao, D.H. Lien, C.Y. Wen, J.H. He, S.C. Lee, Dual-functional memory and threshold resistive switching based on the push-pull mechanism of oxygen ions, *Sci. Rep.* 6 (2016) 23945. doi:10.1038/srep23945.
- [100] S. Walia, S. Balendhran, Y. Wang, R. Ab Kadir, A. Sabirin Zoolfakar, P. Atkin, J. Zhen Ou, S. Sriram, K. Kalantar-Zadeh, M. Bhaskaran, Characterization of metal contacts for two-dimensional MoS<sub>2</sub> nanoflakes, *Appl. Phys. Lett.* 103 (2013) 232105. doi:10.1063/1.4840317.
- [101] S. Sarma, B.M. Mothudi, M.S. Dhlamini, Unipolar resistive switching behaviour of copper doped polyvinyl alcohol/lead sulphide quantum dot device, *J. Mater. Sci. Mater. Electron.* 27 (2016) 3785–3790. doi:10.1007/s10854-015-4223-5.
- [102] K. Oh, W. Jeon, S. Lee, One-Dimensional TiO<sub>2</sub> @ Ag Nanoarchitectures with Interface-Mediated Implementation of Resistance-Switching Behavior in Polymer Nanocomposites, *Appl. Mater. Interfaces.* (2012) 5727–5731.
- [103] X. Huang, B. Zheng, Z. Liu, C. Tan, J. Liu, B. Chen, H. Li, J. Chen, X. Zhang, Z. Fan, W. Zhang, Z. Guo, F. Huo, Y. Yang, L.-H. Xie, W. Huang, H. Zhang, Coating Two-Dimensional Nanomaterials with Metal–Organic Frameworks, *ACS Nano.* 8 (2014) 8695–8701. doi:10.1021/nn503834u.